Material Science and Technology Division

Propulsion Materials Program
Quarterly Progress Report for
January through March 2010

D. R. Johnson
Technical Project Manager

Prepared for
U.S. Department of Energy
Assistant Secretary for Energy Efficiency and Renewable Energy
Office of Vehicle Technologies Program
VT 05 04 000

Prepared by the
OAK RIDGE NATIONAL LABORATORY
Oak Ridge, Tennessee 37831-6066
Managed by
UT-Battelle, LLC
for the Department of Energy
Under contract DE-AC05-00OR22725

CONTENTS

Project 18516 – Materials for Electric and Hybrid Drive Systems

Agreement 16305 – Materials by Design – Solder Joints of High Performance Electronics **(ORNL)**

Agreement 16306 – Power Electronics Materials Compatibility **(ORNL)**

Agreement 16307 – Environmental Effects on Power Electronic Devices **(ORNL)**

Agreement 19201 – MBD Non-Rare Earth Magnetic Materials **(ORNL)**

Project 18517 – Combustion System Materials

Agreement 11752 – Materials for HCCI Engines **(ORNL)**

Project 18518 – Materials for High Efficiency Engines

Agreement 13329 – Mechanical Reliability of Piezo-Stack Actuators **(ORNL)**

Agreement 15050 – Evaluation of Materials via ACERT Engine **(ORNL)**

Agreement 16303 – Materials for High Pressure Fuel Injection Systems **(ORNL)**

Agreement 16304 – Materials for Advanced Engine Valve Train **(ORNL)**

Agreement 17257 – Materials for Advanced Turbocharger Design **(ORNL)**

Agreement 17894 – NDE for ACERT Engine Components **(Argonne)**

Agreement 18570 – Engine Materials Compatibility with Alternative Fuels **(ORNL)**

Agreement 18571 – Materials Issues Associated with EGR Systems **(ORNL)**

Agreement 19202 – Friction and Wear in Ti Components **(ORNL)**

Project 18519 – Materials for Exhaust and Energy Recovery

Agreement 9130 – Catalyst Characterization **(ORNL)**

Agreement 10635 – Catalysts vs First Principles **(ORNL)**

Agreement 19214 – Impact of Biofuels on Diesel Particulate Filters **(ORNL)**

Agreement 20091 – Electrically Regenerated DPF Material **(ORNL)**

<u>Project 18865 – Materials by Design</u>

Agreement 9105 – Characterization of Catalyst Microstructures **(ORNL)**

Agreement 14957 – Thermoelectric Mechanical Reliability **(ORNL)**

Agreement 16308 – MBD - Thermoelectrics Theory and Structure **(ORNL)**

Agreement 17895 – Durability of ACERT Engine Components **(ORNL)**

Agreement 20370 – Life Cycle Modeling of Propulsion Materials **(ORNL)**

Agreement 16305: Materials by Design – Solder Joints of High Performance Power Electronics

G. Muralidharan, Ralph Dinwiddie, Andrew Kercher, and Burak Ozpineci
Oak Ridge National Laboratory

Objective/Scope

Advanced hybrid and electric propulsion systems are required to achieve the desired performance and life targets set for future automobiles. As specified in the OFCVT objectives, a target lifetime of 10-15 years has been projected for hybrid and electric propulsion systems meant for operation in harsh automotive environments. Power electronic components and systems are integral components of advanced automotive hybrid and electric propulsion systems. The trend in automotive power electronics is for using higher operating temperatures which has a detrimental effect on the stability of materials used in such systems. The objective of this task is to evaluate the effects of the higher temperatures on critical metallic materials that are used in power electronic devices and systems and to use the Materials-by-Design approach to identify appropriate combinations of materials that would decrease inopportune failures and maximum lifetime and reliability.

Based on the trend for using higher temperatures in power electronic components, there is a significant need to study failures of electronic packages induced by metallurgical changes of solder joints used as die attaches, and in wire bonds exposed to high temperatures (up to 200°C in contrast to the current 125-150°C exposure) anticipated in such applications. These failures can be induced in solder joints and other components by combination of temperatures, stresses, and current. Coarsening of solder joint microstructure along with the formation of intermetallic compounds takes place during high temperature exposure. Wire bonds are also known to be a key location of failures for packages meant for high temperature use. An understanding of the failures in solder joints and wire bonds will empower us to develop a computation-oriented method for the design of materials for packaging applications.

The approach used in this work would be to study failures in simple package designs so that the emphasis is on materials rather than package design thus avoiding complexities of package design issues that may overshadow materials issues. Packages will be subject to extremes of operational stress levels/temperature levels to the study the origin of failures. Steady-state exposure at high temperatures and cyclic exposures (thermal fatigue) all affect microstructure of the materials, their properties, and hence the failure of joints. X-ray radiography along with acoustic and infrared imaging (as is necessary) will be used to characterize voids present in the solder joints. Knowledge from the failures would enable the selection/development of more appropriate materials that would ensure required lifetimes of 10 to 15 years expected of modules in EVs and Hybrid systems.

Technical Highlights

As reported earlier, in collaboration with Powerex Inc., progress has been made in preparing Au-Sn and Sn-Ag solder joints for thermal cycling testing and high temperature exposure. 2.5 mm x 2.5 mm silicon dies were mounted on a metallized AlN

DBC substrate with the metallization consisting of a medium phosphorus (6-12%) Nickel layer followed by a thin Au layer on the surface. To understand the initial void content in the solder joint, high resolution x-ray radiography was carried out on all the specimens.

Thermal cycling results showed that joints between Au-Sn and Si resulted in cracking of the silicon die during thermal cycling. Ag-Sn joints between silicon and DBC substrates have been tested to 3000 cycles.

In order to understand the relationship between material properties, damage evolution and solder joint fatigue life, finite element modeling of damage evolution in solder joints during thermal cycling has been initiated based upon information available in the literature [1]. 3-D finite element modes of the assembled joints have been created and initial results of stress and strain evolution has been obtained. In this quarter, progress has been achieved in finite element modeling. Figure 2 shows the shear stresses at point B as a function of the thermal cycle. These results will be published shortly.

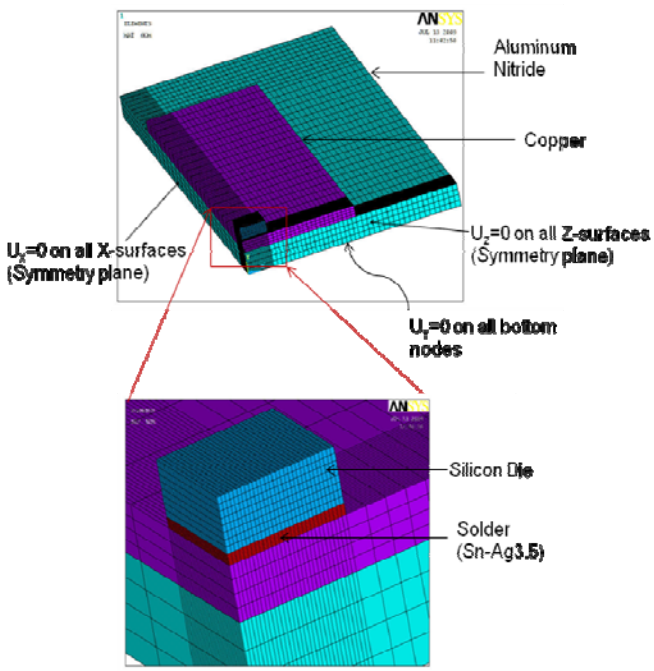

Figure 1. 3-D Finite Element Model of Silicon Die, Sn-Ag Solder Die Attach, and Substrate.

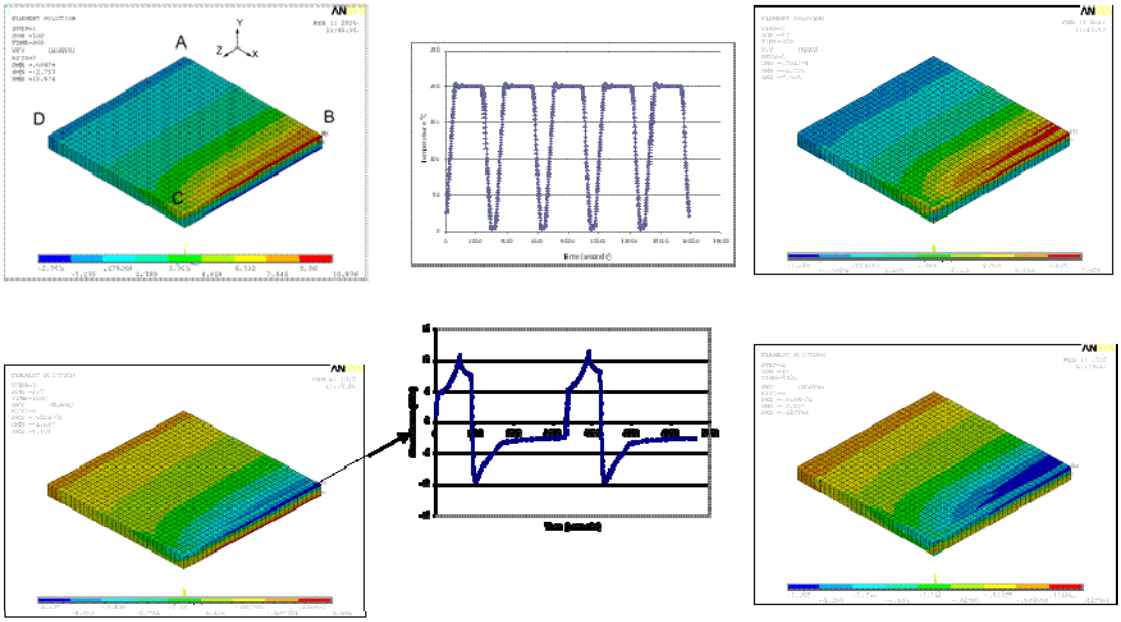

Figure 2. Shear Stresses at point B as a function of temperature within the thermal cycle.

In addition, thermal diffusivity measurements have been initiated to understand the ability to monitor damage accumulation in solder joints. Figure 3 (a) shows the schematic of the thermal diffusivity measurement system and figure 3 (b) shows the measured intensity as a function of time. The time for intensity to increase to half the maximum was used to characterize the thermal diffusivity based on ASTM 1461-92. Figure 4 shows the effect of damage accumulation on the half-rise time. Figure 4 (a) shows the x-ray image and the half-rise time in the region shown on a specimen that was not subject to any thermal cycles, while figure 4(b) shows half-rise time in a sample subject to 3000 thermal cycles. Note that thermal diffusivity is poor in areas (higher half-rise time) in the specimen with accumulated damage. Thus this technique can be used to effectively monitor damage within the solder joints.

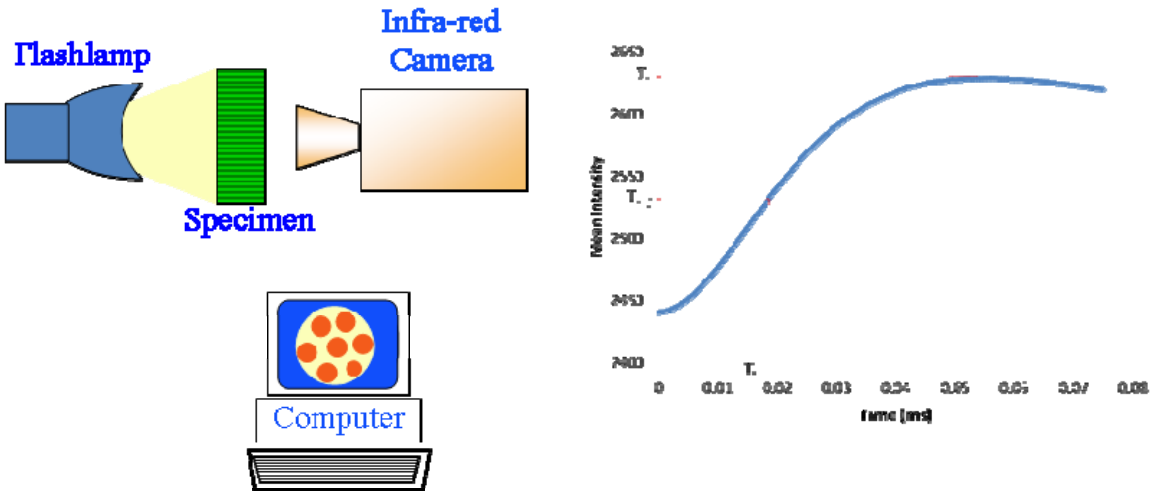

(a) (b)

Figure 3 (a). Schematic of the experimental setup used for characterizing thermal diffusivity. (b) Intensity measured by the IR camera as a function of time in response to the heat pulse from the flash lamp.

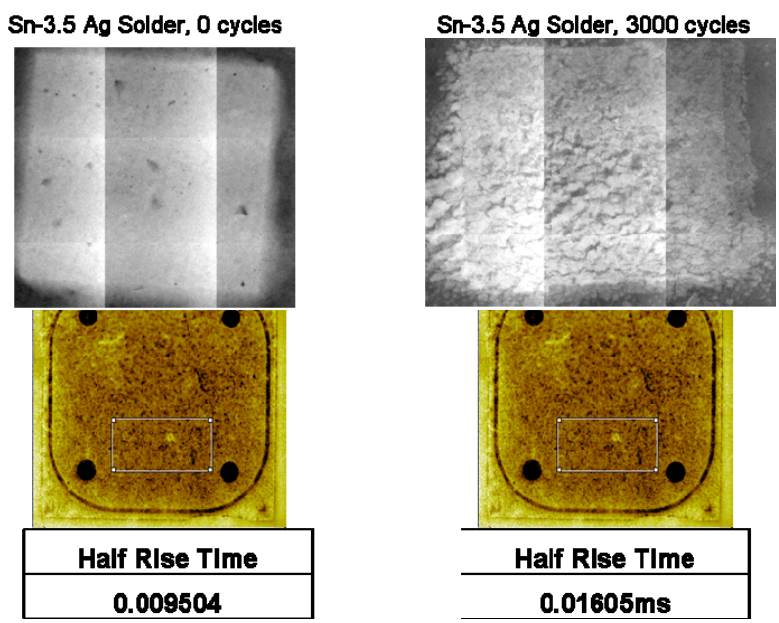

Figure 4. Increase in half rise time as a function of damage accumulation due to thermal cycles (a) Zero cycles, and (b) 3000 cycles.

Discussions are also being carried out with a vendor to design equipment for the preparation of sintered joints.

Status of FY 2010 Milestones

Work is on schedule to meet the following milestone.
Complete fabrication and evaluate reliability of sintered joint using one thermal cycling condition (9/2010)

Communications/Visits/Travel

Communications are on-going with a vendor on the design and fabrication of a system for preparation of sintered joints

Problems Encountered

None

Publications/Presentations/Awards

None

References

1. Bret. A. Zahn, “Impact of Ball Via Configurations on Solder Joint Reliability in Tape-Based, Chip-Scale Packages,” Proceedings of 2002 Electronics Component and Technology Conference, pp. 1475-1483.

Agreement 16306: Materials Compatibility of Power Electronics

B. L. Armstrong, D. F. Wilson, C. W. Ayers, S. L. Campbell, and S. J. Pawel
Oak Ridge National Laboratory

Objective/Scope

The use of evaporative cooling for power electronics has grown significantly in recent years as power levels and related performance criteria have increased. As service temperature and pressure requirements are expanded, there is concern among the Original Equipment Manufacturers (OEMs) that the reliability of electrical devices will decrease due to degradation of the electronic materials that come in contact with the liquid refrigerants. Potential forms of degradation are expected to include corrosion of thin metallic conductors as well as physical/chemical deterioration of thin polymer materials and/or the interface properties at the junction between dissimilar materials in the assembled components. Initially, this project will develop the laboratory methodology to evaluate the degradation of power electronics materials by evaporative liquids.

Technical Highlights

During this quarter, work was continued on the cycle timing and the current being pushed through the circuits. Testing was performed at 39 amperes per wire with 2 seconds on and 2 seconds off cycle for 933,400 cycles, as compared to the 40 ampere per wire test that was performed out to 932,770 cycles. While the latter 40 ampere test resulted in gross deformation of the wires and incipient failure, the 39 ampere test showed no gross indications of impending failure, as shown in Figure 1. Metallographic examination of the cross section of the wires is ongoing to determine if any morphological changes had occurred.

Specimen wires have been sent to an industrial laboratory for chemical analyses. Transmission Electron Microscopy examination of failed specimens was continued.

Status of FY 2010 Milestones

Validate the proposed methodology for examining the interaction of the electrical components with evaporative coolant. **(09/09)** On track.

Communications/Visits/Travel

None.

Problems Encountered

Plans to test ribbon bonds have been stymied by the current limitation of the present system. Work is ongoing to resolve the issue so that testing can be performed with similar current density per unit cross section area as for the circular cross section wires.

Publications/Presentations/Awards

None.

References
None to report.

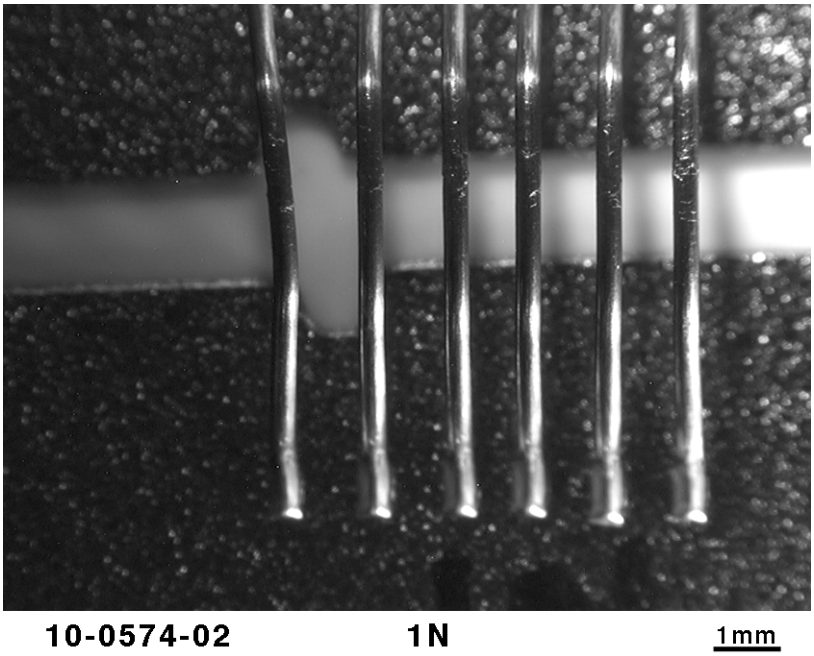

Figure 1. Appearance for wires bonds after 933,400 cycles of 39 amperes per wire with 2 seconds on and 2 second off.

Agreement 16307: Modeling/Testing of Environmental Effects on PE Devices

A. A. Wereszczak, T. P. Kirkland, P. J. Ritt, and H. -T. Lin
Oak Ridge National Laboratory

O. M. Jadaan
University of Wisconsin-Platteville

Objective/Scope

Understand the complex relationship between environment (temperature, humidity, and vibration) and the performance and reliability of the material constituents within automotive power electronic (PE) devices and in supportive systems. There is significant interest in developing more advanced PE devices (PED) and systems for transportation applications (e.g., hybrid electric vehicles, plug-in hybrids) that are capable of sustained operation to 200°C. Advances in packaging materials and technology can achieve this but only after their service limitations are better understood via modeling and testing.

Technical Highlights

Two primary efforts were performed during the present reporting period. The first is continued work to develop a flash diffusivity method to determine thermal properties of multilaminate power electronic devices. Direct bonded copper substrates were ordered and will be used for model test coupons for that. The second effort is a summation of mechanical failure stress testing of silicon and silicon carbide die, and that description follows.

Introduction

Silicon (Si) and silicon carbide (SiC) chips in power electronic devices are subjected to thermal gradients, have coefficient of thermal expansion mismatches with the constituents they are attached to, and therefore are subjected to consequential thermomechanical tensile stresses during operation that can initiate their fracture.

Being they are brittle like glasses and ceramics, it stands to reason that their tensile failure strength is statistical in nature. Several studies have pursued the mechanical testing of silicon chips and interpreted the measured failure stress in this manner.

Wereszczak *et al.* [1] conducted 4-pt bend tests using different test specimen dimensions and statistically examined the strength of etched and polished surfaces. They found that edge-slicing quality could be quite limiting of the overall failure stress but that surface-type flaws and hybrids of edge- and surface-type flaws could be operative too. A convenient manner to portray their competition is shown in Fig. 1. Extrinsic flaws (e.g., surface pitting, scratches, edge-chipping) tend to limit the mechanical strength of chips whereas intrinsic flaws (volume- or bulk-based) are very rare. Another class of brittle materials that is like semiconductor chips is glass.

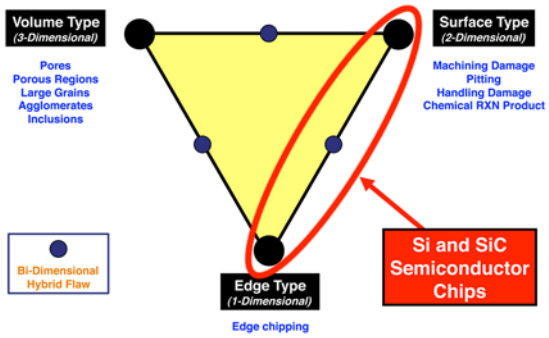

Figure 1. Potential strength-limiting flaw types in semiconductor chips.

Cotterell *et al.* [2] examined the statistical failure stress using 4-pt-bend and ring-on-ring (i.e., axisymmetric 4-pt-bend) testing. While Cotterell's work was systematic, concern over those results arises from the relatively large spans that were used relative to the chip thickness, and the belief that nonlinear elastic effects were likely introduced as a consequence. These were not accounted for and inaccuracy in the results was likely caused. Such issues need to be considered in flexure testing and indeed are considered in standardized tests for uniaxial and biaxial flexure testing [3-4].

Colleti *et al.* [5] considered the competition of edge- and surface-based strength limiting but used ring-on-ring testing to focus study on the latter.

Zhao *et al.* [6] used 3-pt-bending and ball-on-ring (i.e., axisymmetric 3-pt bending) to study the convolution of edge- and surface-type flaws that limit failure stress. A problem with ball-on-ring testing is its generated effective area (i.e., sampled area under tension) is quite small and uncertainty can therefore be produced when comparing the failure strength of different surface conditions. Additionally, Zhao *et al.* used a 3-parameter Weibull distribution to fit the failure stress data; while a "good" fit was perhaps produced, disadvantages of using the 3-parameter fit are it can mask the presence (and problems) of exclusive flaw populations (an indicator of inhomogeneously distributed flaw populations) [7-8], and it does not lend itself easily to strength-size-scaling analysis [9] that is routinely used with 2-parameter Weibull distributions [10] when designing brittle material components and estimating their mechanical reliability.

The present study had several objectives. First, it sought to measure and compare failure stresses in Si and SiC semiconductor chips that had the same physical size and mechanically tested in the same manner. Second, owing to the author's past experience with edges limiting strength in sliced Si semiconductors [1], we sought to use mechanical test methods that would promote failure initiation at the edges. Third, the authors have performed an extensive amount of mechanical testing involving edge characterization of glass tiles [11]. Owing to the fact that glass tiles have similarity to semiconductor chips (i.e., very smooth surfaces with cut, chamfered, or sliced edges or the same flaw types of interest in Fig. 1), and that the authors have found anticlastic bend testing to be an effective method to measure failure stresses with glass tiles, anticlastic bending of Si and SiC chips was pursued to judge its applicability.

Experimental

Silicon {111} and silicon carbide (n-type 4H {0001}) chips were acquired from commercial sources. Dimensions were 10 x 10 x 0.25 mm. One side of the Si chips was lapped and the other was polished. Both sides of the SiC chips were polished. None of the chips of either material had metallization on them. Neither specific slicing method nor procedure was prescribed for either material. Record of the orientation of all chips (or specimens) was kept through the testing history. The primary flat of the silicon wafer was parallel to <112> and that for the silicon carbide was parallel to <112bar0>.

Flexure testing of the entire (square) chips was conducted using uniaxial flexure (three-point-bending) and biaxial flexure (anticlastic bending).

For 3-pt bending, a 5.0-mm span was chosen to sustain classical Eulerian beam bending with respect to the 0.25-mm thick chips. A schematic of the test configuration is shown in Fig. 2. 4-pt bending typically has an advantage over 3-pt-bending in that more of a specimen is desirably subjected to a uniform tensile stress; however, if test specimen geometries and fixtures are small (such as they are in this study), then it can be experimentally difficult to promote, sustain, and validate alignment with the 4-pt configuration. Because of that, the authors pursued 3-pt-bending because maintaining alignment is experimentally easy to achieve, and that advantage was deemed to be more important than the disadvantage of it sampling less material to a tensile stress.

The failure stress (S_{3pt}) for 3-pt-bending is represented by

$$S_{3pt} = \phi \frac{3PL}{2bt^2} \tag{1}$$

where P is failure load, L is the fixture span (5.0 mm), b is the base (10.0 mm), and t is thickness (0.25 mm), and ϕ (=1.02) is a correction factor that takes into account the relatively large base to thickness ratio for the chip to distinguish it from a beam [12]. The outer-fiber tensile stress profile across the span is shown in Fig. 3.

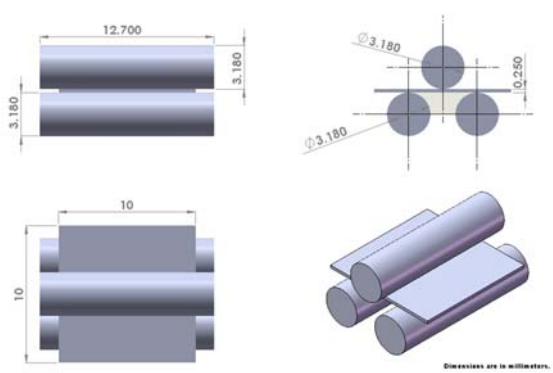

Figure 2. Schematic diagram of the 3-pt-bend test setup. The support span was 5.0 mm.

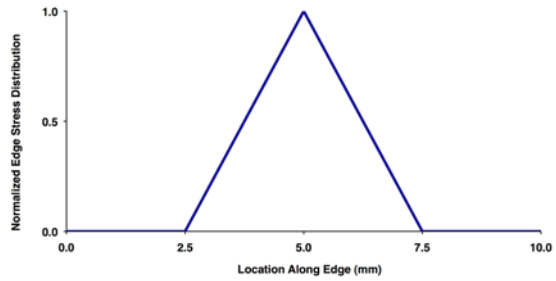

Figure 3. Outer-fiber tensile stress distribution for the 3-pt-bend fixture.

The anticlastic (AC) biaxial flexure specimen was first used by Zamrik *et al.* [13-14] to study crack growth behavior under biaxial fatigue conditions.

The advantage of the anticlastic bend test is all eight edges are subjected to identical sinusoidal stress distribution so the tensile failure stress will be sensitive to the chip's edge-state quality, crystallographic orientation, and surface condition too. Four balls, two on each side of the chip or plate, aligned along counter-opposing diagonals are compressed to produce the anticlastic bending state. This is an example where a schematic (see Fig. 4) is much more effective to describe the manner of loading than a narrative is.

A finite element analysis (FEA) model was constructed to examine the stress state of the 10 x 10 x 0.25 mm chips subjected to anticlastic bending. The first principal (equivalent) stress profile is shown in Fig. 5 for an applied compressive load of 100 N. High radial tensile stresses around the four Hertzian loading positions are not the source of failure initiation if the surface condition of the plate is of high surface finish or has minimally sized flaws and if there are edge-located flaws of relatively large size or severity. This scenario is why AC bending works well with glass and also why it was considered for use in this study with semiconductor chips.

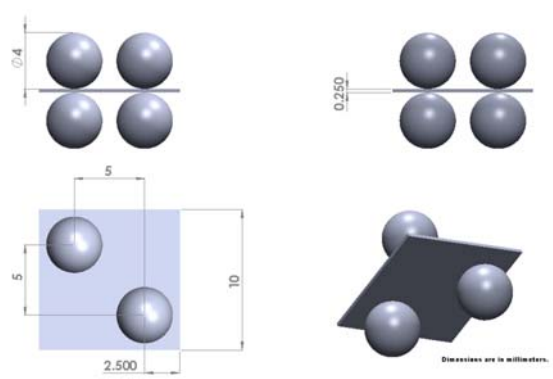

Figure 4. Schematic diagram of the anticlastic bend test setup.

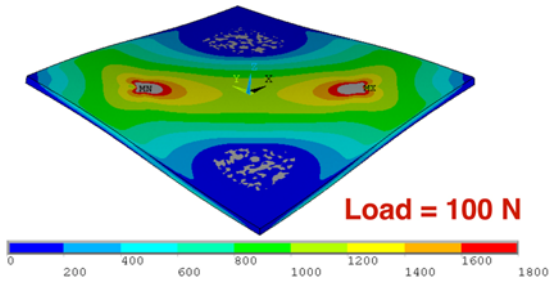

Figure 5. First principal (or equivalent) stress profile of an anticlastically bent silicon chip.

The stress profiles along two of the edges of an anticlastically bent specimen are shown in Fig. 6, and the relationship between compressive force and maximum tensile stress, as determined by FEA, is shown in Fig. 7. The relationship shown in Fig. 7 was used to determine failure stress in the anticlastic bend tests. The sinusoidally produced stress profile along each edge is apparent, and all 8 of the primary edges are subjected to this. If the stress-limiting flaws at an edge are larger in size than those flaws on the surface of the plate, then failure initiation will commence from an edge. This is accomplished within a single specimen. Additionally, this AC bend method is sensitive to the chip's edge-state quality, crystallographic orientation, and surface condition too. Many specimens would be needed for a uniaxial flexure (i.e., 3-pt or 4-pt bending) test matrix to equivalently examine all these effects, and "surface- based" test methods, such as ball-on-ring and ring-on-ring would not be effective at concurrently sampling edge-effects like the AC bend method.

To examine strength-size-scaling or tensile-failure-size-scaling based on Weibull effective length, the probability of failure (P_f) can be represented by

$$P_f = 1 - \exp\left[-\left(\frac{\sigma_{\max}}{\sigma_{0L}}\right)^m L_e\right] \tag{2}$$

where σ_{max} is the maximum applied tensile stress along the edges, σ_{0L} is the scale parameter due to edge-type flaws, m is the Weibull modulus, and L_e is the effective length. The effective length is described as

$$L_e = \int \left(\frac{\sigma(x)}{\sigma_{\max}}\right)^m dx \quad . \tag{3}$$

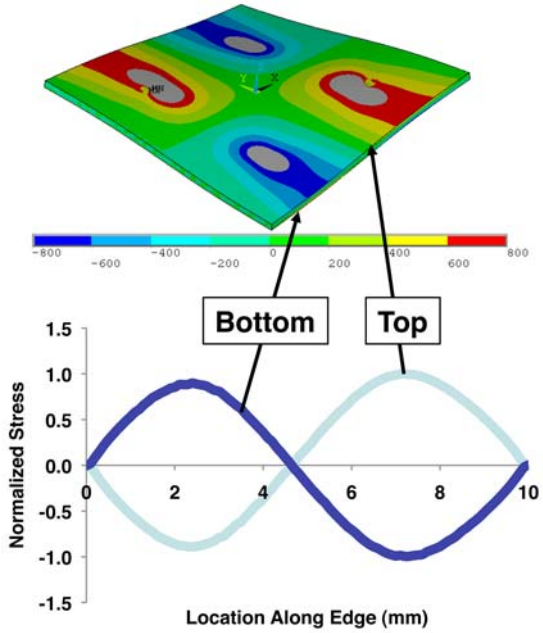

Figure 6. Stress profile along the edges of an anticlastically bent chip.

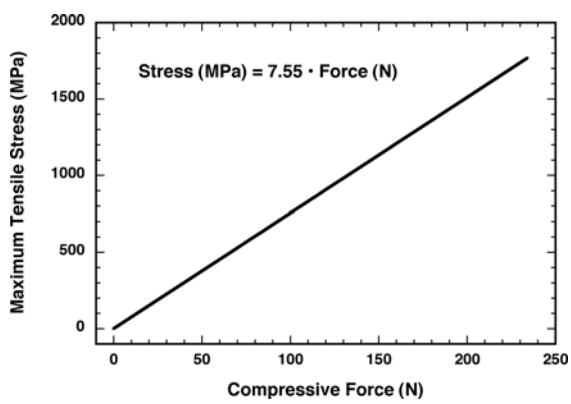

Figure 7. Maximum tensile stress as a function of compressive for the anticlastic bend specimen whose loading is shown in Fig. 4.

The effective length can be used for strength scaling whereby the strength of one component (or specimen in this case) can be predicted from that of another with different stress distribution and edge length by equating their probabilities of failure according to

$$\left(\frac{\sigma_{f1}}{\sigma_{f2}}\right) = \left(\frac{L_{e2}}{L_{e1}}\right)^{\frac{1}{m}} . \tag{4}$$

In order to evaluate the effective length using Eq. 3 for the AC bent chip, the stress distributions along the edges of the chip must be described as a function of position, x. This stress profile is illustrated in Fig. 6. Hence, Eq. 3 for the AC flexure specimen simplifies to

$$L_{e,AC} = \frac{4}{\sigma_{\max}^{m}} \left[\int_{0}^{x1} \sigma_{top_edge}^{m}(x)\,dx \right] + \frac{4}{\sigma_{\max}^{m}} \left[\int_{0}^{x2} \sigma_{bottom_edge}^{m}(x)\,dx \right] . \tag{5}$$

Unlike the AC flexure specimen, the 3-point bend test induces tensile stresses along only two edges. The effective length formula for a 3-point bend specimen is associated with the stress profile in Fig. 3 is given by

$$L_{e,3pt} = \frac{2L}{m+1} . \tag{6}$$

The effective lengths are a function of Weibull modulus and the profiles for the anticlastic and 3-pt bend specimens which are shown in Fig. 8. This figure shows that, for a given Weibull modulus, the anticlastic bend specimen subjects much more edge length to a tensile stress than the 3-pt bend specimen does.

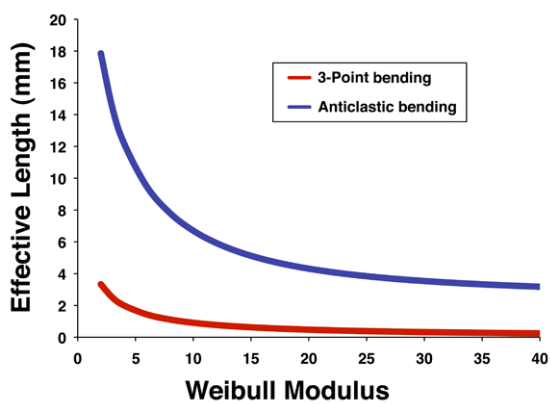

Figure 8. Weibull effective length as a function of Weibull modulus for the two bend test configurations used in this study.

All 3-pt and anticlastic bend tests were done using an electromechanical test frame and a crosshead displacement rate of 0.5 mm/min. At least 14 specimens were tested for each condition and their Weibull failure stress distributions were determine using commercial statistical software which uses maximum likelihood estimation to determine the (2-parameter) Weibull modulus and characteristic strength of each set. 95% confidence ratio rings were determined for each set and were used to compare data sets.

Optical microscopy was used to identify the failure locations of all the specimens. Scanning electron microscopy was used with a select few specimens to examine the edge and surface qualities of the chips.

Results and Discussion

The 3-pt strength distributions for the Si chips are shown in Fig. 9. There were two surface conditions for the Si (lapped and polished) and two crystallographically aligned orientations with the chip's edges (<112> and <110> directions), so there were four combinations tested with the 3-pt bending. The <112> lapped set had the lowest characteristic strength among the four while the <112> polished set exhibited the least amount of scatter (as represented by a higher Weibull modulus). The characteristic strengths of both polished orientations were equivalent.

Optical microscopy showed that failure initiation with the 3-pt bend specimens occurred on the surfaces (and not the edges) of the lapped Si chips but that initiation occurred at edges of the polished Si chips.

Examples of chipping along edges on the lapped and polished surfaces are illustrated in Figs. 10-11. Edge chipping on the two crystallographic directions (Fig. 10) was not noticeably different and that is probably why their characteristic strengths were equivalent. However, the edge chipping on the edges bordering the lapped surface was much more severe (Fig. 11); however, the surface-located flaws inherent to the lapped surface were still more dominant in limiting strength than these severe edge-type flaws.

When a component is mechanically confined and concurrently subjected to a thermal gradient through its thickness (i.e., such as these chips during service), then higher tensile stresses will occur on the colder side. For an attached chip subjected to cooling, the lapped side of the chip will be that colder side. How may the results in Fig. 8 be interpreted in context with this? If an attached chip is subjected to a uniform biaxial tensile stress, then (Mode I) failure initiation is more likely to occur perpendicular to the weakest direction <112> and away from the edge. From a design perspective, if a rectangular chip could be used instead of a square chip (but with the same area or edge length), then a rectangular chip whose longer axis is parallel to <110> will have a higher probability of survival (all other things being equal).

The 3-pt failure stress distributions for the two SiC chips are shown in Fig. 12. The two surfaces of the SiC chips were both polished so only crystallographic orientation effects were examined. While the characteristic strengths of all the SiC chips were approximately an order of magnitude larger than those for the Si chips, the characteristic strength of the SiC chips tensile stressed perpendicular to <112bar0> were stronger than those stressed parallel to that direction. Additionally, the failure initiation of all SiC chips occurred at their edges. This shows that surface polishing removes (or minimizes the effects of) surface-type strength-limiting flaws and that translates into failure initiation at the edges.

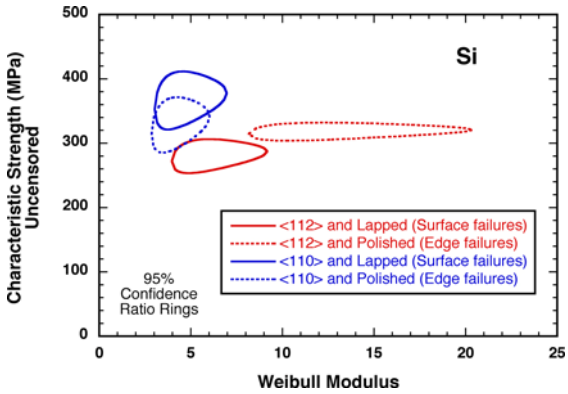

Figure 9. A Weibull strength distribution for the four combinations of 3-pt-bend test sets on the Si chips. 95% confidence ratio rings shown.

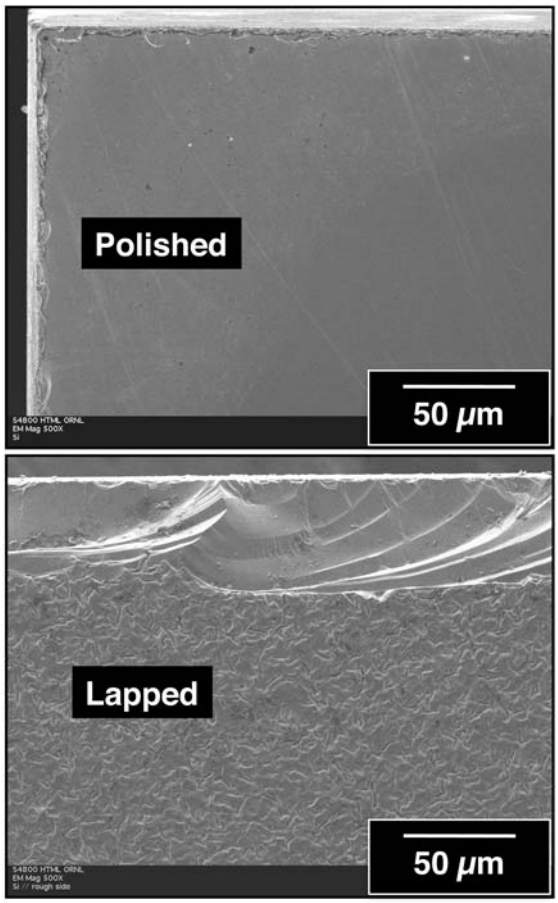

Figure 10. Representative edge chipping and comparison of polished and lapped surfaces on a Si chip.

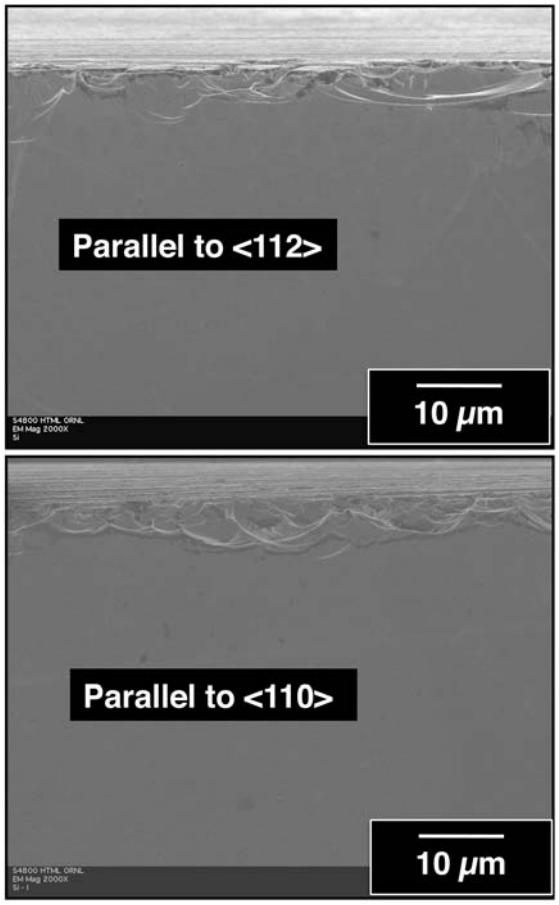

Figure 11. Representative edge chipping and comparison of polished surfaces on edges parallel to <112> and <110> directions on a Si chip.

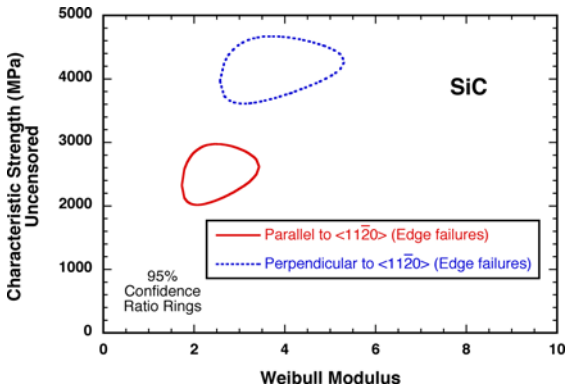

Figure 12. A Weibull strength distribution for the two combinations of 3-pt-bend test sets on the SiC chips (both sides were polished). 95% confidence ratio rings shown.

The significantly higher characteristic strength of the SiC chips compared to the Si chips is likely a consequence of the difference in the quality of the edge slicing. Examples of edge chipping on the SiC chips are shown in Fig. 13. The chipping is much smaller in stature than the chipping in the Si chips (compare with Figs 10-11). Given these differences in edge quality, one could conclude that the differences in characteristic strength are due to differences in these extrinsic type of strength-limiting flaws and not differences in intrinsic or bulk material differences.

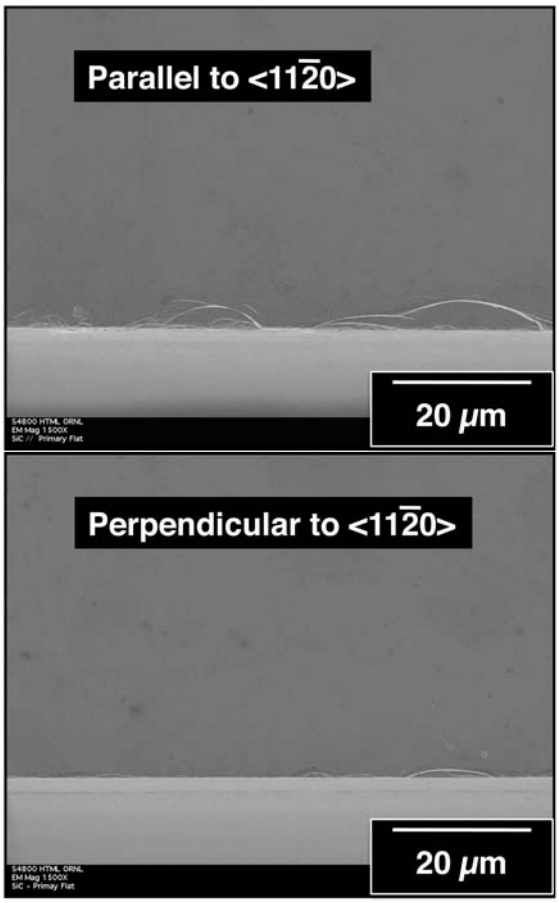

Figure 13. Representative edge chipping and comparison of polished surfaces on edges parallel and perpendicular to <1120> direction on a SiC chip.

The anticlastic bending characteristic strength of the SiC chips was almost an order of magnitude larger than that for the Si chips as shown in Fig. 14. Failure initiation with the SiC chips occurred at an edge whereas failure initiation with the Si chips occurred away from the edge. In fact, optical fractography showed that failure initiation with the Si chips routinely occurred on the lapped surface directly opposite (or under) where one of the two balls was making contact with the polished surface.

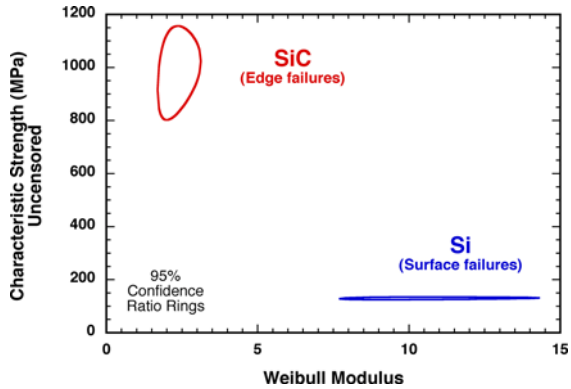

Figure 14. Weibull strength distributions for anticlastic bend test sets. 95% confidence ratio rings shown.

Anticlastic bending tensile stresses operate over greater total lengths of chip edges than 3-point bending does, and because of that, its specimens fail at lower failure stresses when surface type-flaws are not operative (i.e., in the case of the SiC chips). The anticlastic failure stress for SiC chips was approximately one-third that of the 3-pt bend characteristic stresses. For more confident design and mechanical reliability analysis, it is always advantageous to have failure stress data from test coupons that sample (or tensile stress) as much material as possible. Therefore, anticlastic bending can be an effective test method for evaluating edge failure stress in semiconductor chips if surface-type strength-limiting flaws are not dominant.

Conclusions

Extrinsic strength-limiting flaws located at their edges and on lapped surfaces limit tensile stress tolerance of Si and SiC chips. And that tensile stress tolerance exhibits size scaling. Namely, failure stress is lower with longer (effective) edge lengths and with larger (effective) areas. This is consistent with the established utilization of censored Weibull tensile strength distributions for the design and mechanical reliability estimation of brittle material components.

Anticlastic bending tensile stresses much greater lengths of chip edges than 3-point bending does, and because of that, this specimens fails at lower failure stress when surface type-flaws are not operative. For more confident design and mechanical reliability analysis, it is always advantageous to have failure stress data from test coupons that sample (or tensile stress) as much material as possible. Therefore, anticlastic bending can be an effective test method for evaluating edge failure stress in semiconductor chips if surface-type strength-limiting flaws are not dominant.

Edge-strength anisotropy was observed with both the Si and SiC. This suggests that if non-square chips are used (e.g., rectangular chips) that there is an advantage to having the longer axis being parallel with the stronger direction.

Surface-strength anisotropy was observed with the Si because one side was lapped and the other polished. The lapped side is weaker. Others have described this effect too. For conservative design or mechanical reliability estimation, the use of the strength distribution measured with the (weaker) lapped should be used.

The SiC chips failed at higher tensile stresses than Si chips; however, that difference may be a ramification of edge slicing differences and not intrinsic material differences.

Status of FY 2010 Milestones

Develop a test coupon, method, and model that will estimate and measure the apparent thermal diffusivity of a PED's die-solder-DBC laminate. (09/10) *On schedule.*

Communications/Visits/Travel

Wereszczak had numerous meetings with VT APEEM PIs L. Marlino, F. Wang, and R, Wiles to discuss collaborative efforts. Wereszczak also had several discussions with NREL about prospective collaborations involving the thermal diffusivity experiments run in this project.

Problems Encountered

None.

Publications/Presentations/Awards

A paper entitled "Edge-Controlled Mechanical Failure of Si and SiC Semiconductor Chips" co-authored by A. A. Wereszczak, O. M. Jadaan, and T. P. Kirkland was submitted to the IMAPS sponsored conference High Temperature Electronics (HiTEC 2010). To be held May 11-13, 2010 in Albuquerque, NM.

References

[1] A. A. Wereszczak, A. S. Barnes, and K. Breder, "Probabilistic Strength of {111} n-Type Silicon," Journal of Materials Science: Materials in Electronics, Vol. 11, pp. 291-303, 2000.

[2] B. Cotterell, Z. Chen, J. -B. Han, and N. -X. Tan, "The Strength of the Silicon Die in Flip-Chip Assemblies," Journal of Electronic Packaging, Vol. 125, pp. 114-119, March, 2003.

[3] Standard Test Method for Flexural Strength of Advanced Ceramics at Ambient Temperatures, ASTM C1161, Vol. 15.01, ASTM International, West Conshohocken, PA, 2008.

[4] Standard Test Method for Monotonic Equibiaxial Flexure Strength of Advanced Ceramics at Ambient Temperature, ASTM C1499, Vol. 15.01, ASTM International, West Conshohocken, PA, 2008.

[5] G. Coletti, C. J. J. Tool, and L. J. Geerligs, “Mechanical Strength of Silicon Wafers and Its Modeling,” Presented at the 15th Workshop on Crystalline Silicon Solar Cells & Modules: Materials and Processes, Vail, CO, Aug. 7-12, 2005.

[6] J. –H. Zhao, J. Tellkamp, V. Gupta, and D. Edwards, “Experimental Evaluations of the Strength of Silicon Die by 3-Point-Bend Versus Ball-on-Ring Tests,” 2008 11th

IEEE Intersociety Conference on Thermal and Thermomechanical Phenomena in Electronic Systems, I-THERM, pp. 687-694, 2008.
[7] C. A. Johnson, "Fracture Statistics in Design and Application," GE Report No. 79CRD212, General Electric, Schenectady, NY, 1979.
[8] A. A. Wereszczak and T. P. Kirkland, "Exclusivity of Strength-Limiting Extrinsic Surface and Hybrid Flaws," Ceramic Engineering Science Proceedings, Vol. 27, No. 2, pp. 593-601, 2006.
[9] Standard Practice for Size Scaling of Tensile Strengths Using Weibull Statistics for Advanced Ceramics, ASTM C1683, Vol. 15.01, ASTM International, West Conshohocken, PA, 2008.
[10] Standard Practice for Reporting Uniaxial Strength Data and Estimating Weibull Distribution Parameters for Advanced Ceramics, ASTM C1239, Vol. 15.01, ASTM International, West Conshohocken, PA, 2008.
[11] A. A. Wereszczak, T. P. Kirkland, K. T. Strong, Jr., and T. J. Holmquist ORNL/TM-2009/234 Report: “ORNL Quasi-Static Mechanical Characterization and Analysis: FY09 Annual Report to TARDEC,” December, 2009.
[12] F. I. Baratta, “When is a Beam a Plate?” Journal of the American Ceramic Society, Vol. 65, No. 5, p. C86, 1981.
[13] S. Y. Zamrik, and M. Shabara, “The Effect of Stress Ratio on Fatigue Crack Growth in a Biaxial stress Field,” *ASME Transactions, Journal of Pressure Vessel Technology, Vol. 99*, Series J, No. 1, p. 137-143 (1977).
[14] S. Y. Zamrik, and D. C. Davis, “A Novel Test Method and Apparatus for Multiaxial Fatigue Studies,” *Advances in Multiaxial Fatigue*, ASTM STP 1191, D. L. McDowell and R. Ellis, Eds., American Society for Testing and Materials, pp. 204-219, 1993.

Agreement 19201: Non-Rare Earth Magnetic Materials

Michael A. McGuire and David J. Singh
Oak Ridge National Laboratory

Objective/Scope

We will examine rare-earth-free chemical systems which hold promise for the discovery of new high-temperature ferromagnets with the large magnetic moments and strong anisotropies required for technologically useful permanent magnet materials. This research will focus on the development of new rare-earth free permanent magnet materials. Understudied chemical systems which are likely to contain materials with properties required for useful ferromagnets (large moments, high Curie temperatures, strong magnetic anisotropy) will be synthesized and characterized. First principle calculations will be performed to aid in the identification of promising target materials and to guide chemical tuning of magnetic properties through element substitutions and alloying. The focus will be on materials based on elements, such as Mn, Fe and Co, suitable for application in vehicles.

The primary challenge in this work is to obtain high magnetic anisotropy without rare-earth elements, while maintaining high saturation magnetization. The two main sources of anisotropy are magneto-crystalline anisotropy and shape anisotropy. Magneto-crystalline anisotropy is an intrinsic property determined by energy required to rotate a magnetic moment relative to the crystal lattice. Shape anisotropy is an extrinsic property related to the domain structure of individual crystallites. We are targeting new materials with large magneto-crystalline anisotropy, which could then be further enhanced by materials processing to optimize magnetic domain configurations.

Technical Highlights

Work in this quarter involved the initial explorations of some of the materials and ideas put forth in last quarter's Report.

(1) *Zr_2Co_{11} and Hf_2Co_{11}*. The crystal structures of these materials are not well understood. Some studies of the 4*d* analogue Zr_2Co_{11} have been reported, and suggest a hexagonal structure with a large c/a ratio of ~5.1 [Ivanova 2007, Gabay 2001]. Our investigation of Hf_2Co_{11} has indicated a similar highly anisotropic crystal structure.

Zr_2Co_{11} and Hf_2Co_{11} were synthesized by arcmelting and annealing. Magnetization measurements showed that samples prepared in this way were ferromagnetic at room temperature, but with very little remnant magnetization (Figure 1). Lack of magnetic saturation up to H = 60 kOe suggests relatively strong magnetic anisotropy.

Since the crystal structure is suspected to be anisotropic, we investigated the effects of direction solidification using melt spinning. Although often the rapid cooling associated with this technique is used to make amorphous materials, in this case the products were better crystallized than the annealed materials. This is perhaps due to better mixing by the RF heating used in the melt-spinning process.

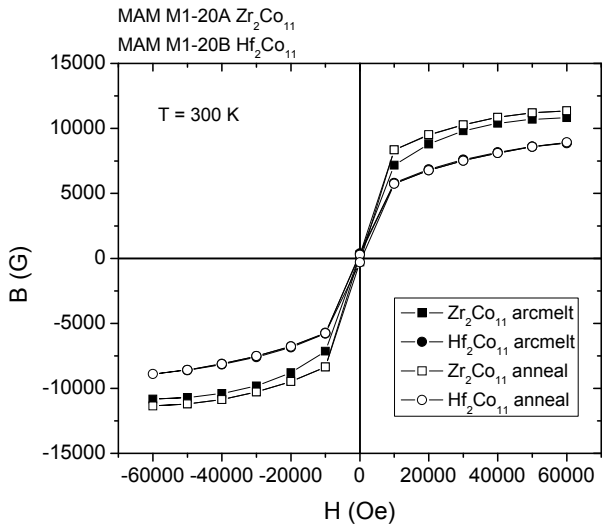

Figure 1. Magnetic induction B vs. applied field H for Zr_2Co_{11} and Hf_2Co_{11} prepared by arcmelting (solid symbols), and after annealing at 1100C for 3.5d (open symbols).

Melt-spinning resulted in a large increase in the remnant magnetization (Figure 2), indicating a significant increase in coercivity over the arcmelted and annealed samples (Figure 1). We note that demagnetization effects are not accounted for in the data shown in Figure 2. When H is perpendicular to the thin melt-spun ribbons, there may be a significant demagnetizing field. The observation of enhanced coercivity in the melt-spun samples led us to investigate more carefully the magnetic behavior of Hf_2Co_{11}.

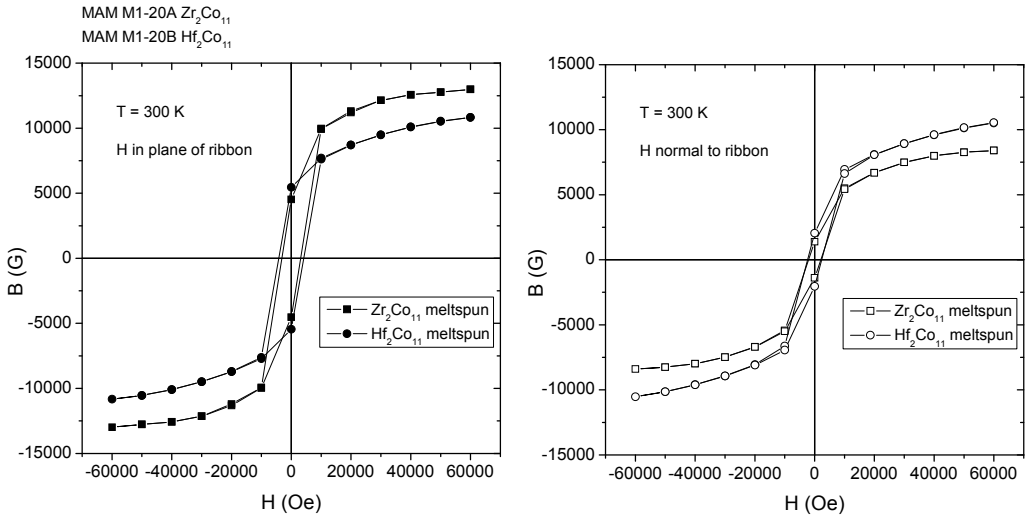

Figure 2. B vs. H for Zr_2Co_{11} and Hf_2Co_{11} melt-spun ribbons measured both in the plane of the ribbon and normal to the ribbons. Demagnetization effects, perhaps large for H normal to the ribbons, have not been accounted for.

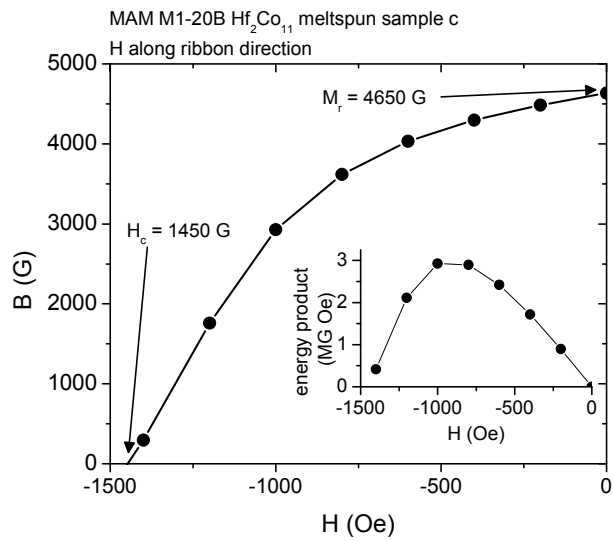

Figure 3. The second quadrant of the B/H diagram for melt-spun Hf_2Co_{11}. The remnant magnetization Br and the coercive field Hc are indicated in the main panel. The inset shows the energy product BH which reaches a maximum value of about 3 MGOe.

Magnetization data collected upon decreasing the magnetic field from $0 \geq H \geq H_c$ after applying a field of +60 kOe is shown in Figure 3. The energy product (the product of B and H) is shown in the inset, and reaches a value near 3 MGOe. This is comparable with ferrite magnets, but about an order of magnitude lower than rare-earth magnets. These results are very encouraging, and we believe this first sample is unlikely to be optimized, and improvements will come with more experimentation.

We are continuing our investigation of these materials, through modifying the melt-spin procedure and the incorporation of intercalants like B, C, and N. In addition, we are examining the effects of replacement of some of the Co with other 3*d* transition metals. We are also studying further the Zr material, which has shown a higher saturation magnetization than the Hf compound in our samples studied to date.

(2) *$TaCo_2$ and $TaFe_2$ Laves phases.* These hexagonal phases are composed of the 3*d* and 5*d* transition metals identified to be promising components of magnet materials. However, the magnetic properties of these phases are not well understood, likely due to relatively wide homogeneity ranges. $TaFe_2$ is reported to be paramagnetic to low temperatures, but is nearly ferromagnetic (FM) and FM can be induced by small changes in stoichiometry [Wada 1989]. "$TaCo_2$" has a wide composition range, and is hexagonal for compositions with 25.5 – 27% Ta. These Ta-poor compositions are FM at low temperature (below 20K) [Itoh 1974]. These nearly and barely FM compounds were chosen to investigate the possibility and effects of nitrogen intercalation.

$TaFe_2$ and $Ta_{27}Co_{73}$ were synthesized by arcmelting and annealing, resulting in well crystallized high-purity samples. Initial tests indicate some reactivity toward nitrogen gas at relatively low T (400 C); however, these results are still preliminary, and conclusions will be reported at a later date.

Status of FY 2010 Milestones

We are progressing toward our milestone of discovering new ferromagnetic materials that do not contain rare-earth elements.

Communications/Visits/Travel

None to report for this quarter.

Problems Encountered

No significant problems have been encountered.

Publications/Presentations/Awards

None to report for this quarter.

References

[Ivanova 2007] G.V. Ivanova *et al.*, J. Alloys. Compd. **432**, 135 (2007).
[Gabay 2001] A.M. Gabay *et al.*, J. Magnetism and Magnetic Materials **236**, 37 (2001).
[Wada 1989] H. Wada *et al.*, Physica B **161**, 197 (1989).
[Itoh 1974] H. Itoh *et al*., Z. Metallkunde **65**, 149 (1974).

Agreement 11752: Advanced Materials Development through Computational Design for HCCI Engine Applications

Govindarajan Muralidharan, Rick Battiste, and Bruce Bunting
Oak Ridge National Laboratory

Objectives/Scope

To identify and catalog the materials operating conditions in the HCCI engines and utilize computational design concepts to develop advanced materials for such applications.

Highlights

Technical Progress

Materials-by-Design of Advanced Materials:

In this quarter, work was continued on Ni-based alloys for valve applications. As reported earlier, using thermodynamic modeling, microstructure evaluation, and mechanical property evaluation, high temperature fatigue was identified as a property of critical interest in Ni-based alloy valve materials for the next generation automotive engines. In order to develop relationships between the microstructures of the alloys and their mechanical properties, high-temperature fatigue property data were obtained on all down-selected alloys as a part of the project. Using the approximate correlation between the fatigue lives obtained using the rotating beam and fully reversed fatigue testing techniques several alloys with required microstructures have been identified as candidates for high temperature valve applications.

Using the microstructures of these alloys as a guide, computational thermodynamics was used to identify additional alloys with microstructure similar to the commercial alloys with desirable properties. In contrast to the commercially available alloys with Ni-contents in the range of 50 wt. % to 60 wt. %, the Ni-content in these alloys ranges from about 30 wt. % to 45 wt. % with the potential to achieve comparable properties. This implies that the alloys will be of lower cost but comparable mechanical properties. This quarter, several additional alloys have been designed using computational thermodynamics approach and small batches of alloys have been cast and processed. Specimens for tensile tests have been prepared and high temperature mechanical tests have been completed. Microstructural characterization of the alloys have been initiated and microhardness tests have also been completed on the specimens in the aged condition. Figure 1 shows a comparison between the predicted microstructure of two commercial Ni-based alloys and a newly designed alloy with lower Ni-levels. Also shown are the microhardness values of the various alloys indicating that the new alloy has microhardness properties comparable with that of the desirable commercial alloy.

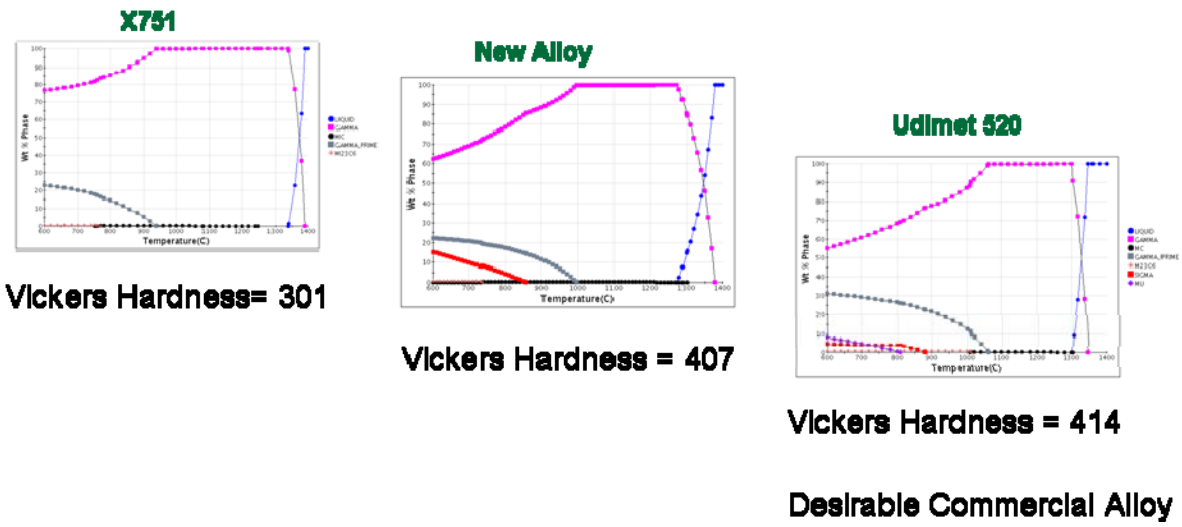

Figure 1. Thermodynamic calculations showing predicted microstructure of two commercial alloys and a newly designed alloy along with microhardness values in the aged condition.

Alloys designed and being tested have a wide range of tensile properties at 871°C and comparable to that of other commercial Ni-based superalloys as shown in Figure 2.

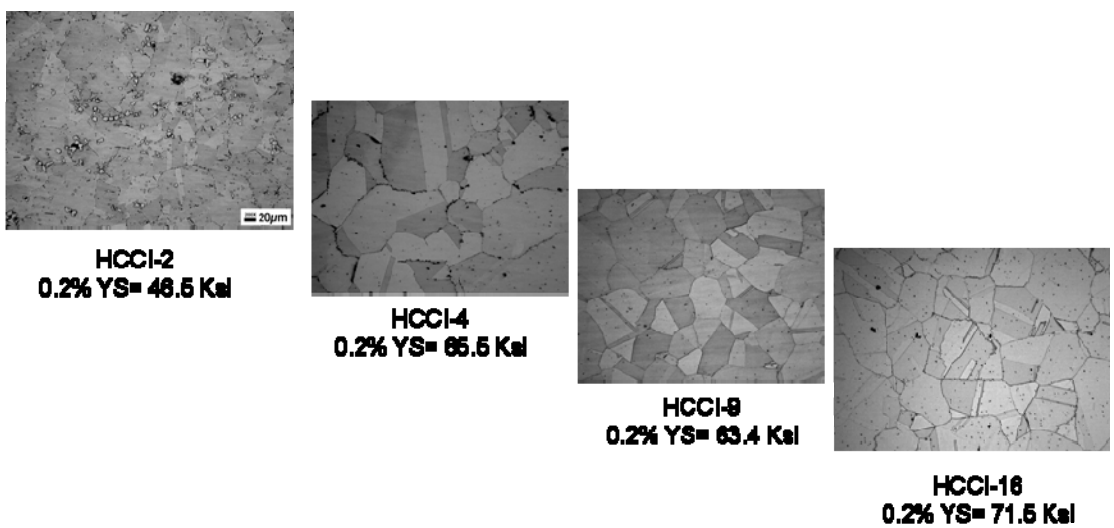

Figure 2. Microstructures and high temperature yield strength of various alloys designed using computational methodology

During this quarter, long-term aging tests will be performed to study the stability of strengthening phases at 871°C. Large scale heat will be cast and processed to enable fatigue testing of alloys at high temperatures**.**

Milestones

Work is on schedule to meet the following milestone:

Complete selection of one commercial alloy and one newly developed alloy for high temperature valve application. **(9/2010)**

Agreement 13329: Design Optimization of Piezoceramic Multilayer Actuators for Heavy Duty Diesel Engine Fuel Injectors

H.-T. Lin, H. Wang, T. Matsunaga, and A. A. Wereszczak
Oak Ridge National Laboratory

J. Carmona-Valdes, and R. Stafford
Cummins Inc.

Objective/Scope

Enable confident utilization of piezo stack actuator in fuel injectors for heavy vehicle diesel engines. The use of such actuators in diesel fuel injectors has the potential to reduce injector response time, provide greater precision and control of the fuel injection event, and lessen energy consumption. Though piezoelectric function is the obvious primary function of lead zirconate titanate (PZT) ceramic stacks for fuel injectors, their mechanical reliability can be a performance and life limiter because PZT is brittle, lacks high strength, and is susceptible to fatigue. However, that brittleness, relatively low strength, and fatigue susceptibility can be overcome with the use of appropriate probabilistic design methods.

Technical Highlights

1. Testing and Characterization on KCI Piezoceramics

Electric cyclic fatigue testing has been conducting on KCI single-layer PZT plate-typed specimens using the ORNL piezodilatometer during this reporting period. The cycling electric field is a unipolar 200 Hz sine wave. These tests were carried out to 10^8 cycles, followed by unipolar and bi-polar measurements using the same piezodilatometer setup. The electric loading was a 0.1 Hz triangle wave. For the unipolar measurement, it run between 0 and $2E_c$; for the bipolar measurement, it run between $-2E_c$ and $2E_c$, where E_c is the coercive electric field of the PZT ceramic evaluated. Variations of piezoelectric and dielectric quantities are given in Figs. 1-5 for four sets of tested specimens.

Following conclusions can be drawn based on the unipolar cycling fatigue testing and observations:

1. The electric contact provided by the original metallic coating is susceptible to the wear in a large number of cycles under high electric loading. An additional electrode is required to secure a proper contact during the cycling.
2. Cu disks seemingly do not have any appreciable effect on the measurement of reference specimen.

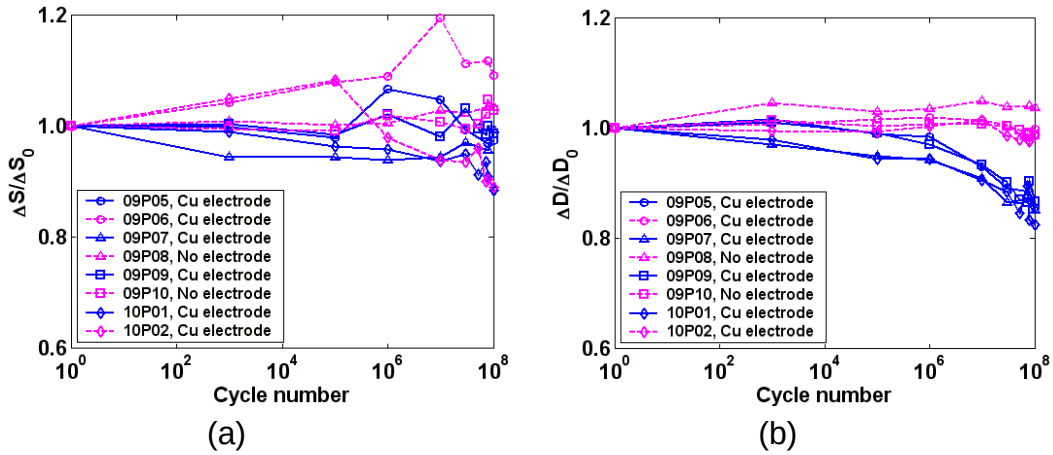

Fig. 1 Fatigue response of KCI single-layer-plate specimens as a function of cycle number for (a) amplitude ΔS of strain – electric field loop S(E), and (b) amplitude ΔD of charge density – electric field loop D(E). Results are based on unipolar measurement, and quantities are normalized to their prefatigue values.

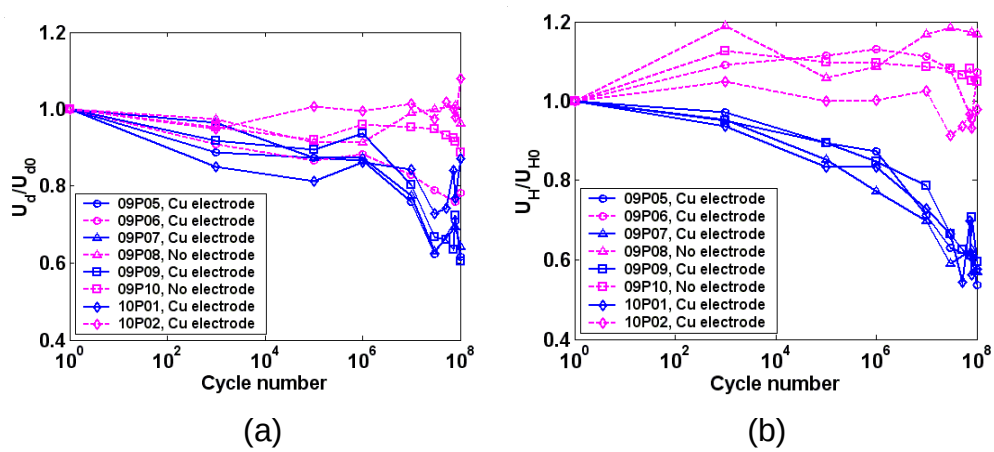

Fig. 2 Fatigue response of KCI single-layer-plate specimens as a function of cycle number for (a) hysteresis U_d of S(E), and (b) hysteresis U_H of D(E). Results are based on unipolar measurement, and quantities are normalized to their prefatigue values.

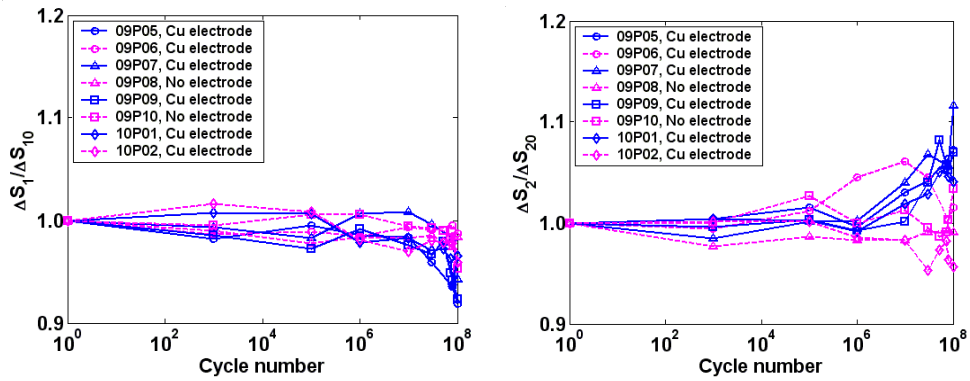

(a) (b)

Fig. 3 Fatigue response of KCI single-layer-plate specimens as a function of cycle number for (a) left wing size ΔS_1, and (b) right wing size ΔS_2 of S(E). Results are based on bipolar measurement, and quantities are normalized to their prefatigue values.

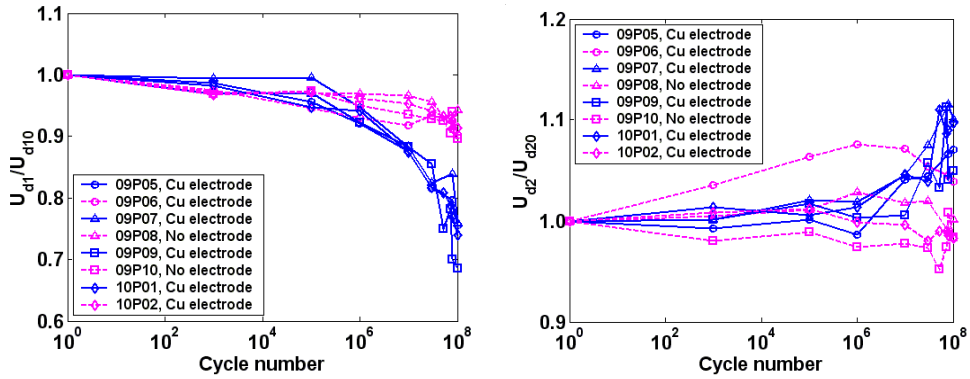

(a) (b)

Fig. 4 Fatigue response of KCI single-layer-plate specimens as a function of cycle number for hysteresis of S(E) corresponding to (a) left wing, U_{d1}, and (b) right wing, U_{d2}. Results are based on bipolar measurement, and quantities are normalized to their prefatigue values.

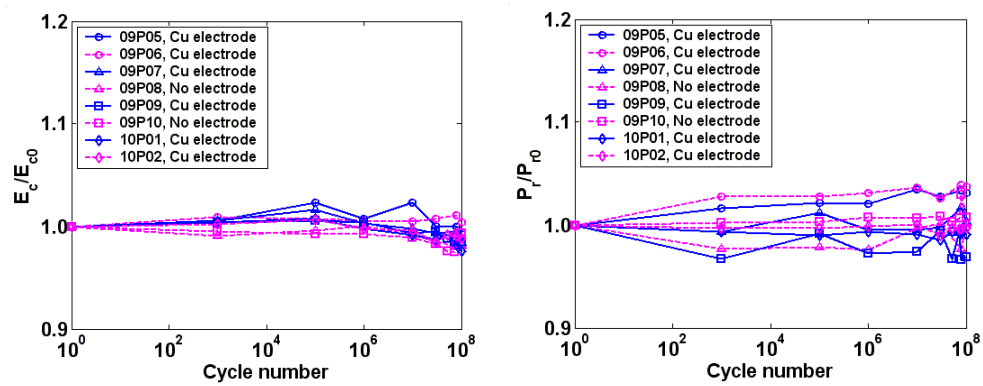

(a) (b)

Fig. 5 Fatigue response of KCI single-layer-plate specimens as a function of cycle number for (a) coercive field E_c, and remanant polarization P_r of D(E) loop. Results are based on bipolar measurement, and quantities are normalized to their prefatigue values.

1) Fatigue results are largely reproducible with regard to the four tested specimen sets so far.
2) The specimens used as a reference during the cycling seemingly capture the fluctuation, but the variation generally appears to be in a less extent.
3) Unipolar and bipolar measurements apparently have their unique features of revealing the characteristics of the unipolar cycling fatigue of PZT.
4) Tested PZT ceramic plates exhibited a significant reduction in the quantities measured by unipolar loading, especially in the charge density, piezoelectric, and dielectric hystereses. However, this observed trend does not hold quite true for the mechanical strain measured.
5) In the bipolar measurement, drastic changes occurred in two wings of S(E) butterfly curve. Particularly, the left wing decreased and the right wing increased. This can be seen from the variations in both the wing size and hysteresis. As for the D(E), the coercive field appeared to be decreased, but the remanant polarization did not.
6) Accordingly, both the asymmetry of S(E) and the bias field of D(E) exhibited a notable change during the cyclic process. [1]

The mobility of domains and domain walls may be affected due to a large number of high-field electric cycles. This shall be reflected in the microstructures of PZT material. The detailed SEM and EDS analyses are being conducted to provide insight into the degradation mechanisms. A user proposal to CNMS-ORNL is being prepared for Scanning Probe Microscopy to reveal the involved fatigue mechanisms in the domains. The results will be reported in future.

The design on including an oil (or, electronic liquid) bath into the current Ball-on-Ring (BoR) test setup has been finished and the fabrication of components is in progress. The availability of this system will enable the BoR test to be performed in as high as $2E_c$ field level without the occurrence of electric arcing due to surface discharge.

At the same time, the concept design for fabricating the discussed fatigue test rig on KCI stack has been finished. The finalization of associated drawings will be based on the inputs from Cummins, Inc.

2. Testing and Characterization on Stack Component Materials

Dielectric breakdown of polyester encapsulant might play key role in the failure of piezo stacks in field tests, and thus needs to be evaluated appropriately. Testing on this material was initiated in this quarter by using ORNL piezodilatometer. The polyester specimens for this purpose were prepared from four end sectors of a tube supplied by Cummins, Inc. These sectors were 12mm long, 3mm wide and 1mm thick. The thickness was reduced to 30 to 50μm by grinding and polishing. These films were then mounted onto a copper substrate by using a carbon conductive tape. The carbon served as a ground electrode. A 2.4mm diameter Cu-disk punched from a conductive copper tape was mounted on the top of film and served as a HV electrode in the testing. The use of film format specimens in the testing was proposed in order for the high-voltage amplifier (Trek 609E-6) to be able to trigger dielectric breakdown. This amplifier has voltage and current monitor channels, and voltage is cut off once the current exceeds a predetermined level. A 60 Hz ac voltage was applied with a ramping rate of 390 V/s. Electronic liquid FC-40 was used as a medium to control the possible surface discharge. The testing was carried out for four polyester film specimens and the results are summarized in Table 1.

Table 1 Dielectric breakdown on polyester film of stack encapsulant

No	Thickness (μm)	Breakdown V_{rms} (kV)	Apparent breakdown E_{rms} (kV/ mm)	Note
1	42	2.08	47.4	Current (rms) stayed at 40 μA and increased abruptly
2	50	2.68	53.6	Current (rms) increased gradually from 28 to 69 μA before breakdown
3	36	1.49	41.1	Current (rms) stayed at 26 μA and increased abruptly
4	32	1.20	37.6	Current (rms) increased gradually from 31 to 66 μA before breakdown

It can be seen that the breakdown field of tested polyester was relatively higher compared with those of regular PZT materials. SEM and EDS analyses were carried out for polished cross sections of these tested polyesters, as shown in Fig. 6. The polyester was observed to have a large volume fraction of reinforcing oxide particles containing elements of Si, Ca, Al and Mg, as shown in Fig. 6(b). There were also cases where the polyester film was not consistently flat as shown in Fig. 6(a). Moreover, a sizable gap can be seen between the polyester film and the

adhesive layer of Cu disk. It is not clear whether the gap came from the preexisting de-bonding by handling or the delamination induced by the dielectric breakdown. As this kind of gaps occurred quite often, it is suggested that a metallic electrode method (such as sputtering) other than a conductive tape should be used in the next step to ensure a more appropriate electric contact and interface condition.

A self-align fixture is being fabricated for the high temperature BoR setup on testing 10-layer plate specimens. These specimens are actually short multilayer actuators extracted from a supplied EPCOS stack (6.8mm x 6.8mm x 30mm). In parallel, four-point bending-bar specimens are also being prepared as well. These bending-bar specimens are based on the same stack geometry as that for preparing 10-layer plates. The planned tests will be then carried out at room temperature to quantify the interfacial mechanical strength of stacks.

Status of FY 2010 Milestones

Measure and compare reliability of competing commercially available piezoactuators under consideration for use in diesel fuel injectors, *on schedule*.

Communications/Visits/Travel

Conference call on CRADA update with Cummins, Inc. was held on March 23.

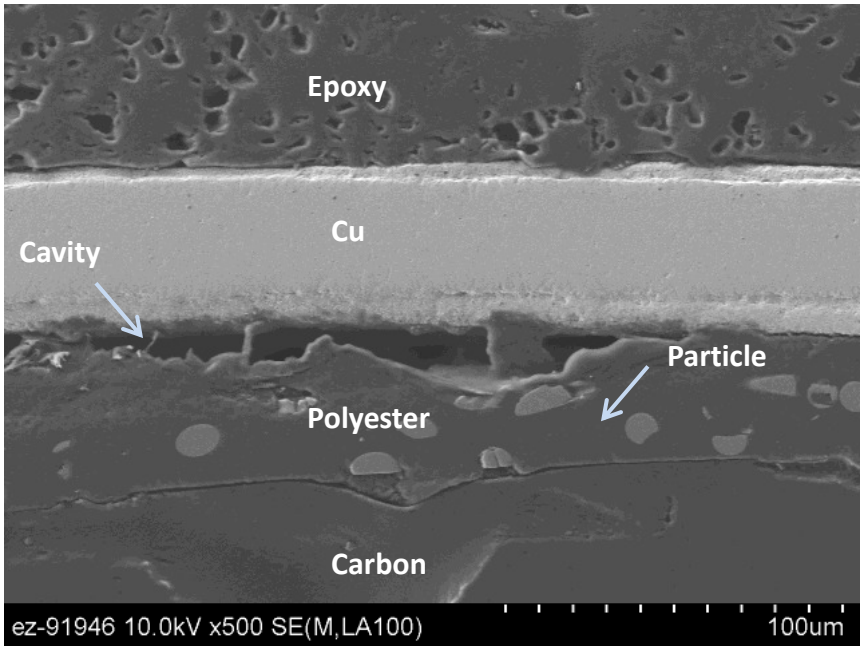

(a)

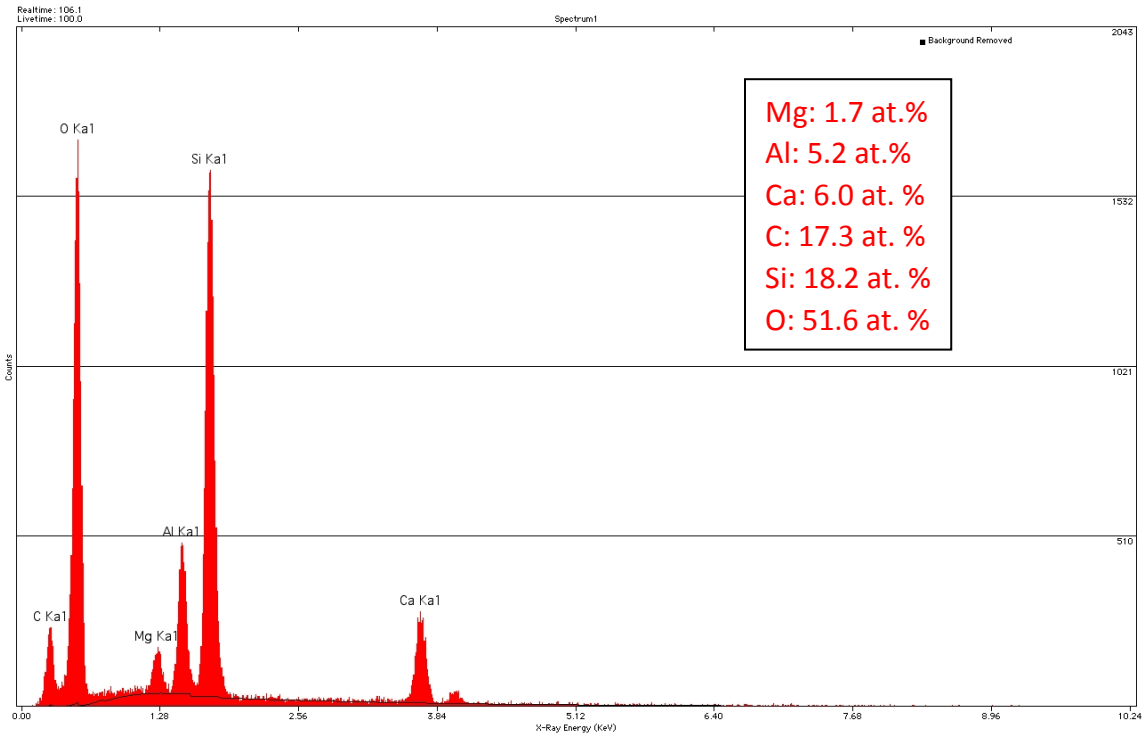

(b)

Fig. 6 (a) Cross section of an epoxy-potted polyester-film specimen (copper substrate is not shown), and (b) EDS spectrum on a reinforcement particle in Fig. 6 (a).

Publications/Presentations/Awards

1. Wang, H., Matsunaga, T. and Lin, H.-T., Characterization of poled single-layer PZT for piezo stack in fuel injection system, *34th Int. Conf. on Adv. Ceramics and Composites*, Jan. 24-29, 2010, Daytona Beach, FL, accepted
2. Wang, H., Cooper, T. A., Lin, H.-T., and Wereszczak, A. A., Fatigue responses of PZT stacks under semi-bipolar electric cycling with mechanical preload, *J. Appl. Phys.*, 2010, accepted.
3. Wang, H., Lin, H.-T., and Wereszczak, A. A., Strength properties of poled PZT subjected to biaxial flexural loading in high electric field, *J. Am. Ceram. Soc.*, 2010, in print.
4. Wang, H., Matsunaga, T., and Lin, H.-T., Effects of temperature and electric field on mechanical strength of single-layer PZT plate, in preparation.

References

1. Wang, H., Matsunaga, T., Lin, H.-T., and Wereszczak, A. A., Electric cyclic fatigue evaluation of PZT plate with an inactive reference included, 2010, unpublished.

Agreement 15050: Evaluation of Materials via ACERT Engine

Michael Kass, Norberto Domingo, Robert M. Wagner, K. Dean Edwards, H.-T. Lin and Brian C. Kaul
Oak Ridge National Laboratory

Objective/Scope

This project is focused on improving the performance, emissions and efficiency of heavy-duty diesel engines through the application of materials enabled technologies. The range of material systems is comprehensive and includes 1) improved structural materials to accommodate higher cylinder pressures and temperatures, 2) improved durability and corrosion resistance, 3) low inertial components to improve transient response, 4) improved emissions aftertreatment performance, and 5) waste heat recovery systems.

To date a dynamometer engine research cell was constructed for use with heavy-duty engines. A 2004 C15 ACERT Caterpillar engine was provided by the Caterpillar materials research staff for materials-based efficiency evaluations. The engine was instrumented for combustion and thermal assessment. During FY09, the Caterpillar combustion research staff signed a WFO agreement with ORNL to evaluate a thermodynamic model used to assess efficiency improvements on the ACERT engine.

Progress This Quarter (January – March 2010)

- Baseline testing of the engine was finished and the results were compared to data provided by Caterpillar. In addition the 973 simulation model results (sponsored by a WFO agreement with Caterpillar) were also determined for the operating points under consideration.

- A representative sample of the results (for the 1200 RPM operating condition) is shown in Figure 1 for engine airflow, air/fuel ratio, and manifold pressure as a function of brake mean effective pressure (BMEP).

  As illustrated here, there are some performance differences between this engine as configured at ORNL and Caterpillar's baseline, but in general the comparison between the ORNL and Caterpillar data is in fairly good agreement. In contrast the 973 simulation results for airflow and air/fuel ratio were noticeably much lower than the experimental results.

  Due to these differences in the engine controller calibration, a complete set of baseline data for the engine as-installed at ORNL, across the speed/load map, will be used in evaluating revised parts, rather than relying on Caterpillar-supplied data.

- ORNL and Caterpillar initiated another WFO to examine mixed-flow turbine performance. A photograph comparing the baseline and mixed-flow turbines is shown in Figure 2. The turbine performance will be evaluated during the next quarterly period and the results will be presented in the next quarterly report.

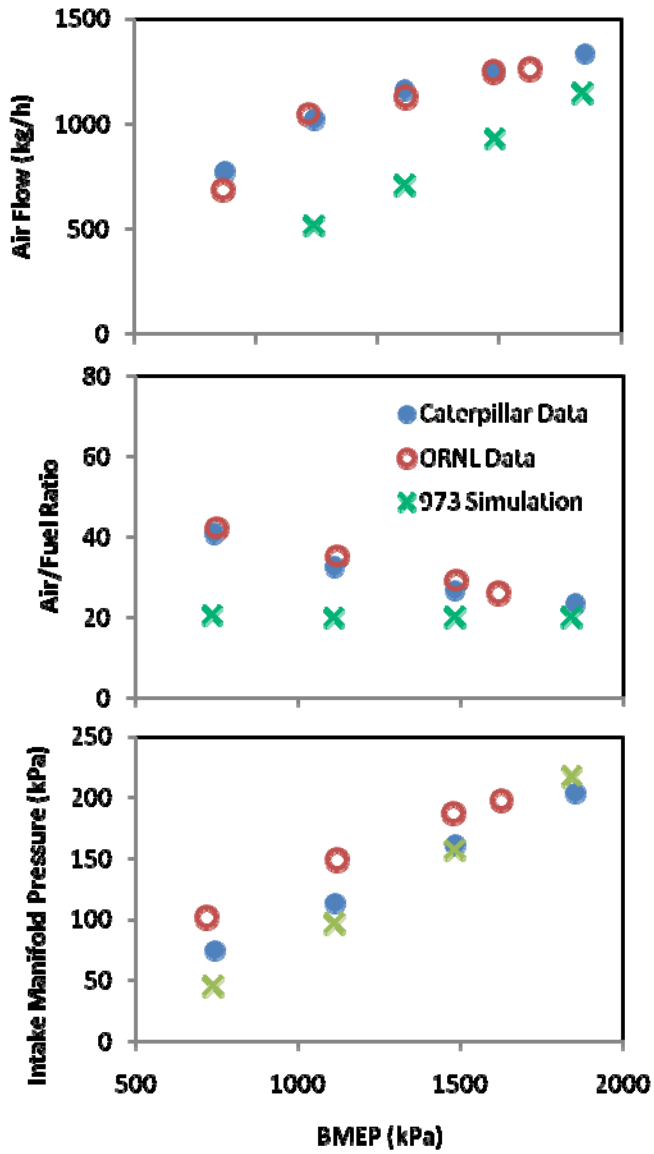

Figure 1 - Baseline BSFC Data at 1200 RPM

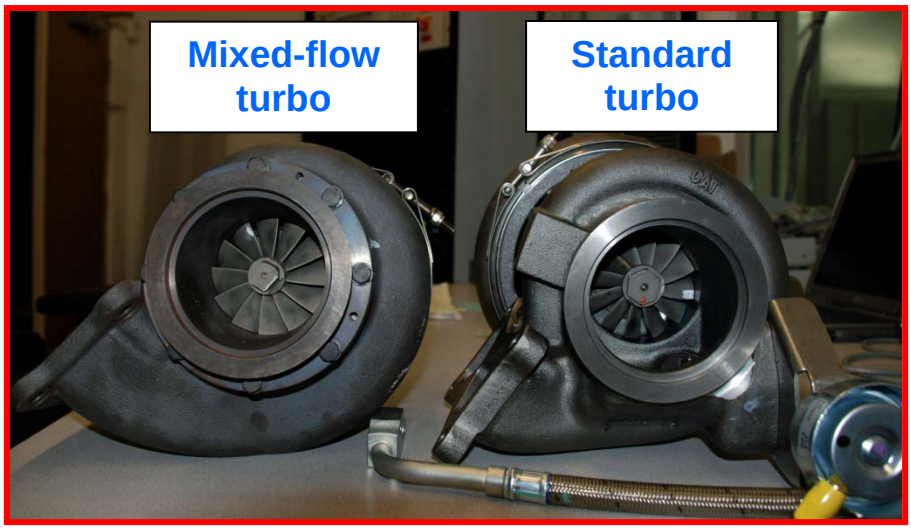

Figure 2 – Photograph showing mixed-flow and baseline turbines.

Publications/Presentations/Awards

No publications or presentations occurred during this quarterly period.

Plans for Next Reporting Period

- Complete the acquisition of baseline data in preparation to use for comparison when evaluating components.

Agreement 16303: Materials for High Pressure Fuel Injection Systems

Peter J. Blau, Jane Howe, Dorothy Coffey, and Amit Shyam
Oak Ridge National Laboratory
and
Michael J. Pollard
Caterpillar Corporation

Objective/Scope

The objective of this Cooperative Research and Development Agreement (CRADA) between UT-Battelle, LLC and Caterpillar Corporation is to advance the state of the art in the characterization, selection, and use of metallic alloys for high-pressure diesel engine fuel injector nozzles.

During recent decades, fuel efficient, low-emissions diesel engine designs for heavy trucks have relied upon increasing fuel injection pressures to optimize combustion characteristics. Precise fuel metering is required. This key functional requirement has raised concerns over the ability of spray holes to be machined to sufficiently close tolerances to provide desired spray patterns and for the materials of construction to withstand hundreds of millions of high-pressure pulses without succumbing to fatigue damage. The data and analyses obtained in the course of this three-year effort are expected to provide vital information for designers and material selectors for high-performance fuel systems for energy-efficient diesel engines.

A three-pronged approach has been developed. It involves: (1) characterization of current fuel injector hole geometry and alloy metallurgy, (2) measuring the residual stress in nozzle tips near spray holes, and (3) development and use of specialized fatigue test methods to address the special requirements of the next generation of high-pressure fuel injectors.

Technical Highlights

Axial fatigue tests continue to assess the effects of heat treatment and the presence of surface notches on the initiation mechanism for microcracks. In coming months, the newly-installed Questar™ tele-microscope system will be used to document crack behavior and provide new insights on flaw propagation mechanics. A publication on these results is anticipated, subject to approval by the CRADA partner. The major technical highlight for this quarter concerns the electron imaging of spray hole fine-structure.

Electron microscopy of hole walls. A major technical accomplishment was achieved during this quarter when the team at ORNL obtained the first ever images of the fine structure of fuel injector hole walls that were produced by electrical discharge machining (EDM). In order to do this, Randy Parten, a precision machinist, first had to section the fuel injector sack in such a way as to expose, lengthwise, the axis of a hole less than 200 µm in diameter. Then Dorothy Coffey used a focused ion beam system (FIB) to cut a minute sliver of material perpendicular to the hole wall, oriented along the axis. This sliver was then lifted out with micromanipulators and thinned to make it electron-transparent. Jane Howe, an experienced electron microscopist in ORNL's High

Temperature Materials Laboratory, then mounted the specimen in a high resolution, analytical scanning transmission electron microscope (ASTEM) to image the fine structure of the hole wall as well as chemically analyze certain detailed features like second-phases and inclusions.

Figure 1 shows a scanning electron micrograph image of the lumpy, recast layer of a spray hole wall, and Figure 2 is scanning transmission electron micrograph of the FIB'ed cross-section of one of those wavy features. Magnified 260,000 times, the nanostructure of the 'frozen waves' is different than that of the underlying alloy, and indicates that the surface material was rapidly solidified and recrystallized during the hole forming process. Sharp features, like the over-lapped wave in Figure 2, could serve at stress concentrators, thereby nucleating new fatigue cracks as high-pressure diesel fuel pulses through the injector nozzle. Having established the feasibility of this method, it will be possible to correlate failure origins in high pressure fuel injectors with the EDM process that produces the spray holes.

Plans for the coming quarter.
1) Continue to conduct axial fatigue tests and fractography of fuel injector alloy specimens that have been machined and heat treated at Caterpillar.
2) Using axial fatigue specimens of current alloys, supplied by Caterpillar in a heat-treated condition, prepare shallow notches in the surfaces of the gauge sections and begin fatigue tests.
3) Obtain new Carpenter Technology alloys as candidates for the fuel injector application and begin their characterization.

Status of FY 2010 Milestones
1) Complete baseline fatigue tests on smooth specimens without artificial flaws. **(3/31/2010) Status:** extended due to a delay in receiving heat-treated test specimens.

2) Complete fatigue tests on heat-treated steel specimens containing holes produced by the same process used on fuel injector nozzles. **(9/30/2010) Status**: on-going.

Communications/Visits/Travel
Monthly coordination calls have been made between ORNL and Caterpillar.

Problems Encountered
There was a delay in receiving specimens for fatigue studies from the partner. Since both FY 2010 milestones are dependent on specimen material availability of test specimens, so this is a critical situation. Efforts are being made to expedite the issue.

Publications/Presentations/Awards
None this period.

References
None

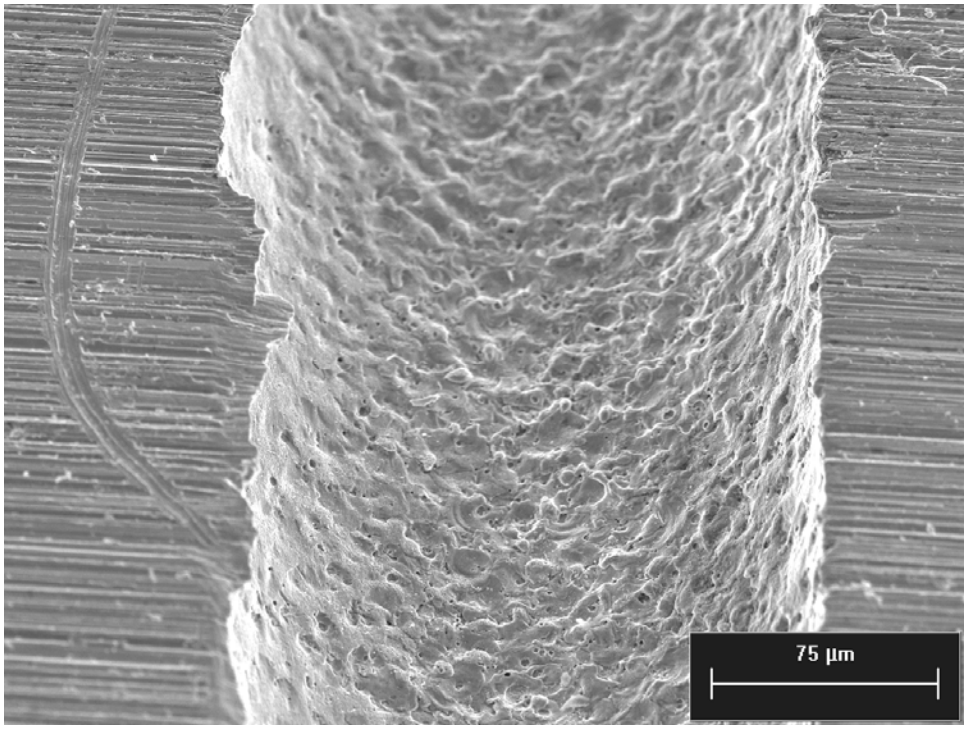

Figure 1. Scanning electron micrograph showing the re-cast layer on the wall of a 192 µm-diameter spray hole (axial section).

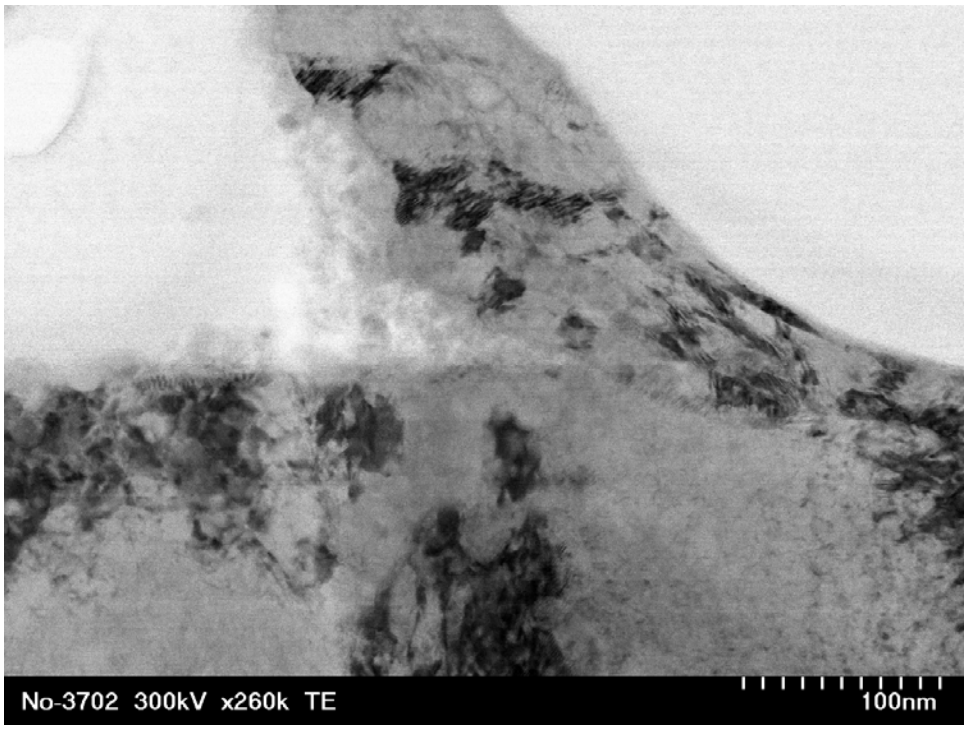

Figure 2. Nanostructural details of the recast and underlying materials on the wall of a spray hole. An overall view of the original ‘slice,’ prior to final thinning, was shown in the previous quarterly report.

Agreement 16304: Materials for Advanced Engine Valve Train

P.J. Maziasz and N.D. Evans
Oak Ridge National Laboratory

M.D. Veliz and N. Phillips
Caterpillar, Inc.

Objective/Scope

This is an ORNL CRADA project with Caterpillar, NFE-07-00995 and DOE OVT Agreement 16304, which lasts for about 3.5 years, and is scheduled to end in Dec., 2010. This CRADA project focused on addressing the wear and failure modes of current on-highway heavy-duty diesel exhaust valves and seats, and then evaluating changes in valve-seat design or selection of advanced alloys, which will then enable higher temperature capability, as well as better performance and durability. The CRADA was extended for 12 more months due to technical success during the 2nd year of the project. Another 24 month extension was requested this quarter, due to the need to generate new creep-data and wear-test new prototype valves made of new Ni-based superalloys with more temperature capability. Requests for more detailed information on this project should be directed to Caterpillar, Inc.

Highlights

Caterpillar, Inc.
Caterpillar began very high temperature wear-rig tests of new prototype exhaust valves made from upgrade Ni-based superalloys with higher temperature capability than standard 31V superalloy valves.

ORNL
ORNL received tensile/creep specimens for testing at ORNL, made from the same upgrade Ni-based superalloys used to make new prototype exhaust valves for testing at Caterpillar. Creep-rupture testing at 800°C and above began at ORNL this quarter, to demonstrate higher temperature capability and performance compared to the standard 31V superalloy.

Technical Progress, 2nd Quarter, FY2010

Background

This OVT Agreement 16304 is an ongoing ORNL CRADA project with Caterpillar, NFE-07-00995, which will last for about 5.5 years, after this year's new 24 month extension. This CRADA project has addressed the wear and failure modes found for current on-highway heavy-duty diesel exhaust valves and seats. It then identified changes in valve-seat advanced alloys that will enable higher temperature capability, as well as better performance and durability. The need for such upgraded valve-seat alloys is driven by the demands to meet new emissions and fuel economy goals, which continue to push diesel exhaust component temperature higher. The CRADA was originally scheduled to

be complete at the end of 2009, but was extended for 12 more months and is being extended for another 24 months, due to outstanding technical progress and success at mitigating wear between exhaust valves and seat-inserts at above 800°C. Requests for more detailed information on this project should be directed to Caterpillar, Inc.

Approach

Caterpillar provides the baseline wear and mechanical behavior characteristics of engine-exposed standard valves and seats, and provides exposure of similar components from simulation-rig testing at Caterpillar. ORNL provides more in-depth characterization and microcharacterization of those valves and seats, and provides knowledge and understanding of the full range of commercially available heat-resistant alloys, to select those most suitable for upgraded valve performance. ORNL and Caterpillar have developed an understanding of the underlying degradation mechanisms, which is the technical basis for selecting and testing alternate valve and seat alloys with upgraded performance and temperature capability. Caterpillar and ORNL are working with Caterpillar's various component and materials suppliers, to enable prototype production of upgraded exhaust valves and seats for evaluation in Caterpillar's wear-test rig, and parallel testing and characterization of the same advanced alloys at ORNL.

Technical Progress – Caterpillar, Inc.

Caterpillar previously initiated a project with a major valve supplier to obtain heats of two advanced, alternate Ni-based superalloys for forging into upgraded exhaust valves. These new upgrade Ni-based alloys should have improved performance and higher temperature capability than the standard 31V alloy. This quarter, Caterpillar received new prototype exhaust valves from its valve supplier, and began testing and evaluation in the wear-test rigs.

Technical Progress – ORNL

ORNL placed a sub-contract with Caterpillar's exhaust valve supplier to forge new valves and to make various mechanical properties test specimens last quarter, from two alternate Ni-based alloys with more temperature capability and performance than the standard 31V alloy. ORNL received all of the test specimens, and began elevated temperature creep-rupture testing this quarter.

Communications/Visits/Travel

Detailed team communications between ORNL and Caterpillar occur regularly in multi-party conference calls. Caterpillar has extended team discussions to include their commercial seat-insert supplier as well as one of their exhaust valve suppliers.

Status of Milestones (ORNL for DOE)

Milestone for Caterpillar rig-testing of prototype valves and seats of new advanced alloys is on schedule for FY 2010.

Publications/Presentations/Awards

None

Agreement 17257 – Materials for Advanced Turbocharger Designs

P.J. Maziasz and A. Shyam
Oak Ridge National Laboratory
and
K. Pattabiraman
Honeywell Turbo Technologies

Objective/Scope

This is a new ORNL CRADA project with Honeywell, NFE-08-01671 (DOE/EERE/OVT Agreement 17257), that began in August 2009, and is scheduled to last for about 3 years. This CRADA project addresses the limitations of lifetime or use-temperature for the various components (casing, wheel, shaft, bearings) of both the turbine and compressor parts of the turbocharger system. As exhaust temperatures increase, to provide higher engine efficiency and lower emissions, turbocharger component temperatures also increase, so the need for most heat-resistant materials must be addressed. Requests for more detailed information on this CRADA project should be directed to Honeywell, Inc.

Highlights

This is a new project that began last quarter.

Technical Progress, 2nd Quarter, FY 2010

Background

This new CRADA project, which began at the end of FY 2009, will extend for 3 years, and covers several different tasks. The first task was to assess and prioritize the various components that need or would most benefit from materials upgrades to increase temperature capability and performance, as well as durability and reliability. The next tasks examine current performance and degredation modes of wheel/shaft assemblies for turbines and compressors, housings for turbines and compressors, and bearings. These tasks may then obtain and test new materials with upgraded performance, and provide the results to Honeywell for designing advanced turbocharger systems, or manufacturing new prototype components for testing and evaluation.

Approach

This new CRADA project was executed late in FY 2009, and began last quarter. This project is comprised of six tasks, which will span the next 36-month period. Activity began with ORNL and Honeywell discussing the priority of the various turbocharger components for materials upgrades.

A turbocharger system includes the hot (turbine) end, driven by exhaust gas from the engine, a cold (compressor) end to increase air pressure into the combustion changer, and a transition region that connects these two ends. The turbine and compressor wheels are connected to a common shaft, supported by bearings. For the first task, the turbine wheel-shaft assembly was chosen as the first component for consideration, with

analysis focused on residual stresses near the weld-joint of the Ni-based superalloy wheel to the steel shaft, which can upset balance during service. Another task of this new CRADA project continues previous work between ORNL and Honeywell on testing of the new CF8C-Plus cast stainless steel as a significant performance upgrade for the turbine housings relative to standard SiMo cast iron. This CRADA project for turbine housings will cover a broad range of other high temperature properties, including creep and fatigue strength, and expand it to turbine housing applications for passenger vehicle gasoline engines.

Technical Progress

For Task 1, Honeywell identified neutron-scattering experiments to measure residual stresses in welded wheel/shaft assemblies as one of their highest priority items. For Task 2, efforts to define these experiments, including developing the proposal needed to obtain neutron scattering time at the HFIR Residual Stress User- Facility, began last quarter and continued this quarter.

For Task 3, ORNL continued several of the CF8C-Plus steel creep-rupture tests that were stopped during a previous ORNL/Honeywell CRADA project. ORNL also machined new tensile/creep specimens of CF8C-Plus steel to fill in the data gaps for selected high-temperature tensile and creep-rupture tests. Honeywell also identified the next steps necessary to commercially produce some prototype turbocharger housing using CF8C-Plus steel for certain turbocharger models, to that they could be evaluated and tested on engines. Figure 1 shows data from previous work by ORNL and Honeywell comparing the new CF8C-Plus steel to HK30-Nb at 600-800°C. HK30-Nb is a standard commercially available cast stainless alloy used for turbochargers for heavy-duty truck diesel engines when temperatures exceed the limitations of SiMo cast iron. Additional tensile testing of as-cast CF8C-Plus steel and HK-30-Nb at 900°C was completed this quarter, and is also included in Figure 1. While CF8C-Plus cast stainless steel and HK30-Nb stainless alloy have similar yield-strengths at 600- 700°C, CF8C-Plus stainless steel has higher strength at 800-900°C than HK30-Nb alloy.

Communications/Visits/Travel

Periodic conference calls are held between ORNL and Honeywell Turbo Technologies, and email communications help to coordinate the work

Status of Milestones (ORNL for DOE)

New project in FY 2010, and milestones for FY 2011 are on-track.

Publications/Presentations/Awards

None

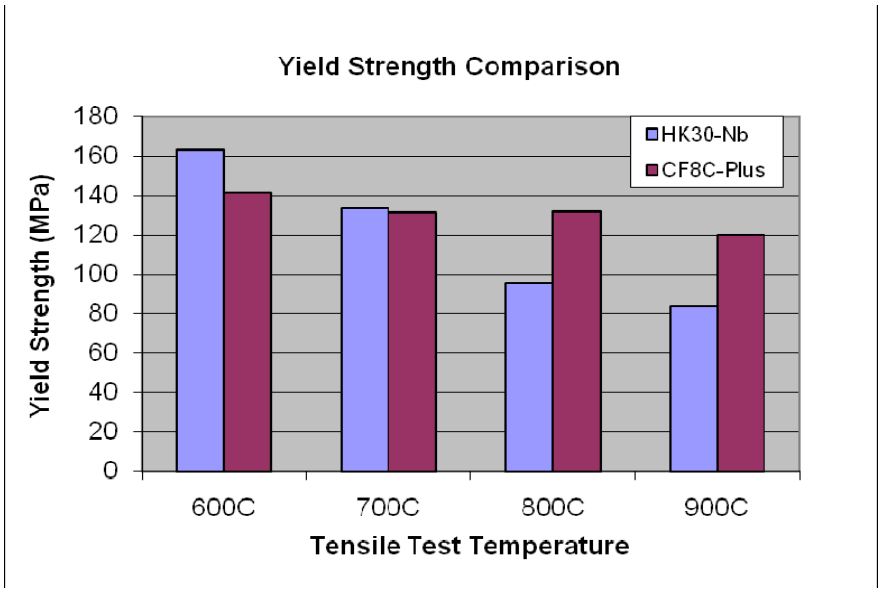

Figure 1 – Comparison of yield strength (YS) measured by elevated temperature tensile testing of both cast CF8C-Plus and cast HK30-Nb austenitic stainless steels. While both materials have similar strength at 600-700°C, the CF8C-Plus cast stainless steel is clearly stronger at 800-900°C.

Agreement 17894: NDE for ACERT Engine Components

J. G. Sun
Argonne National Laboratory

J. A. Jensen
Caterpillar, Inc.
Technical Center

Objective/Scope

Applications of advanced materials in diesel engines may enhance combustion and reduce parasitic and thermal losses, thereby improving engine efficiency. Engine components developed from advanced materials, however, require rigorous assessment to assure their reliability and durability in more stringent operating conditions. The objective of this work is to develop and assess various nondestructive evaluation (NDE) methods for characterization of advanced engine components in a Caterpillar heavy-duty ACERT experimental engine at ORNL. NDE technologies established at ANL, including optical scanning, infrared thermal imaging, ultrasonics, and X-ray CT, will be further developed for detection of volumetric, planar, and other types of flaws that may limit the performance of these components. NDE development will be focused on achieving higher spatial resolution and detection sensitivity. Current efforts are directed in applications of optical methods for valvetrain components, x-ray and ultrasonic for joinings, and thermal imaging for thermal barrier coatings (TBC).

Technical Highlights

Work during this period (January-March 2010) focused on optical imaging NDE analysis for TBC specimens received from Caterpillar and on development of a high depth-resolution algorithm for thermal tomography.

1. Optical Imaging NDE for Thermal Barrier Coatings

During this period we continued NDE imaging and analysis of as-processed and thermally-cycled TBC specimens from Caterpillar. Although thermal imaging provided NDE data for the entire TBC surface, its lateral resolution is limited by the pixel size which is ~0.2mm when testing 1”-squared specimens. To obtain higher resolution, optical scanning methods were investigated for imaging and analysis TBC quality and damage/delamination. Optical imaging can only be used for optically-translucent materials, which is the case for these ceramic TBCs. Two optical methods were used: the laser backscatter for surface area imaging and the optical coherence tomography (OCT) for cross-section imaging. The lateral resolution of these optical methods is typically in the order of ten microns, which is much better than thermal imaging.

Optical NDE of as-processed TBCs

Figure 1 is a photomicrograph of an as-processed TBC surface; it consists of raised circular features of various sizes. In high-magnification SEM images [Lin, et al., Quarterly Report for April-June 2009], many cracks and pores up to a few tens of microns in size are visible on TBC surface, located mostly around the boundaries of large circular features. Figure 2 shows an OCT cross-sectional scan image of as-processed TBC specimen #10. In this scan, the TBC surface was placed at an angle to

the scan beam in order to avoid surface reflection; the scanned image dimension is 1mm x 1mm with a pixel size of 4µm. It is seen that the TBC surface is generally dense, with minimal optical penetration. One penetrated defect, which is likely a crack, can be observed in this image. These cracks are also detected in the laser-backscatter surface-scan image as shown in Fig. 3 (scan area of 5mm x 2mm; pixel size of 5µm). The cracks display high scatter intensities and are mostly arranged in circular patterns, which is consistent with the observations from SEM images. The length of individual cracks varies, but typically within ~25µm long. Because of their small sizes, these cracks could not be detected by thermal imaging (unless a focus lens is used).

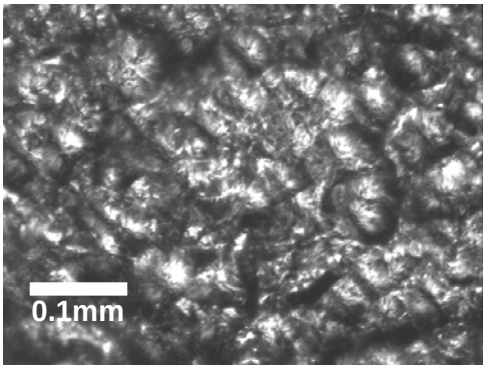

Fig. 1. Photomicrograph of as-processed TBC surface.

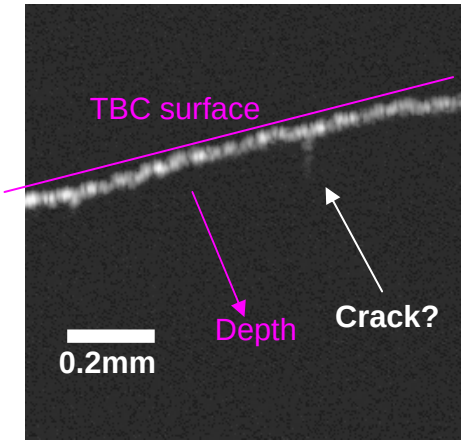

Fig. 2. Cross-sectional OCT scan image of as-processed TBC specimen #10.

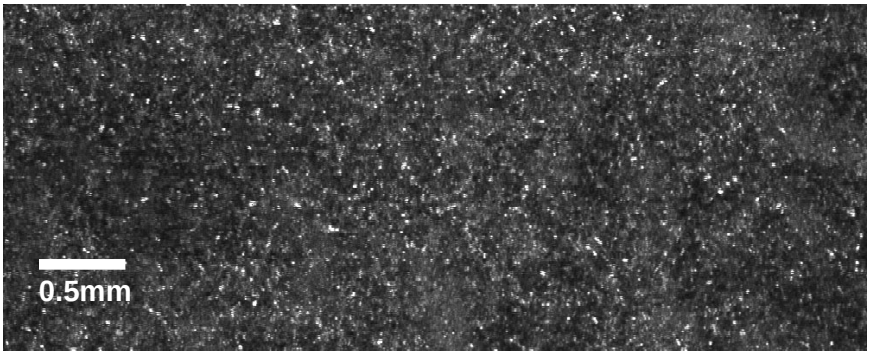

Fig. 3. Laser-backscatter scan image of as-processed TBC specimen #10.

Optical NDE of thermal-cycled TBCs

Preliminary optical imaging data [Sun, 2009 Annual Report] showed that OCT may image the surface elevation and laser backscatter may determine the lateral dimensions of TBC cracks and delaminations. These optical data were not correlated with the actual flaws because of their complex geometries and small sizes. This correlation however is important in validation and calibration of NDE technologies for accurate inspection and reliable prediction of material conditions. To facilitate this correlation, a detailed comparison of the images from NDE and optical microscopy on a large surface area was performed in this period. Figure 4 shows a photograph of the thermal-cycled TBC specimen #9, with an inserted laser-backscatter scan image and the corresponding scan area marked on the TBC surface. The scan image has a dimension of 10 mm x 5 mm, with a pixel size of 10 µm. In general, the TBC surface exhibits either high or low laser-scatter intensities. The intensity pattern in the scan image matches well with that observed in the optical image of the TBC surface. The regions with high-scattering intensities correspond to the gray surface where TBC is damaged or delaminated but still remains on surface, and the regions with low scattering intensities to the dark-brown surface where TBC has already been spalled off [Sun, 2009 Annual Report].

A detailed comparison of the laser-scatter NDE data with the photomicrograph of the TBC surface is shown in Fig. 5. There are at least three types of surface features as indicated in the figure: (1) TBC coatings that have cracked/delaminated and raised above surface as surface bumps; these coatings always display high scatter intensities. (2) Bright flat-surface regions with high scatter intensity; the materials in these surface areas are likely TBCs that are either damaged (with high porosity) or delaminated but are not in the process of spallation. (3) Dark flat-surface regions with low scatter intensity; as discussed above, the TBC in these surface areas was already spalled off from the surface. In addition to these major features, there are other secondary features that need to be further investigated.

The optical NDE data will also be correlated with thermal tomography results. Although it is relatively easy to correlate the larger cracked/delaminated TBCs, smaller TBC delaminations are difficult to be resolved in thermal tomography data because of the lower lateral resolution (~0.2 mm) in thermal imaging. The effort in next period will therefore be focused on acquiring thermal imaging data with high lateral resolutions,

which could be achieved by adjusting the system setup for imaging smaller areas. The NDE data and detailed correlation between thermal and optical methods will be obtained and presented in next report.

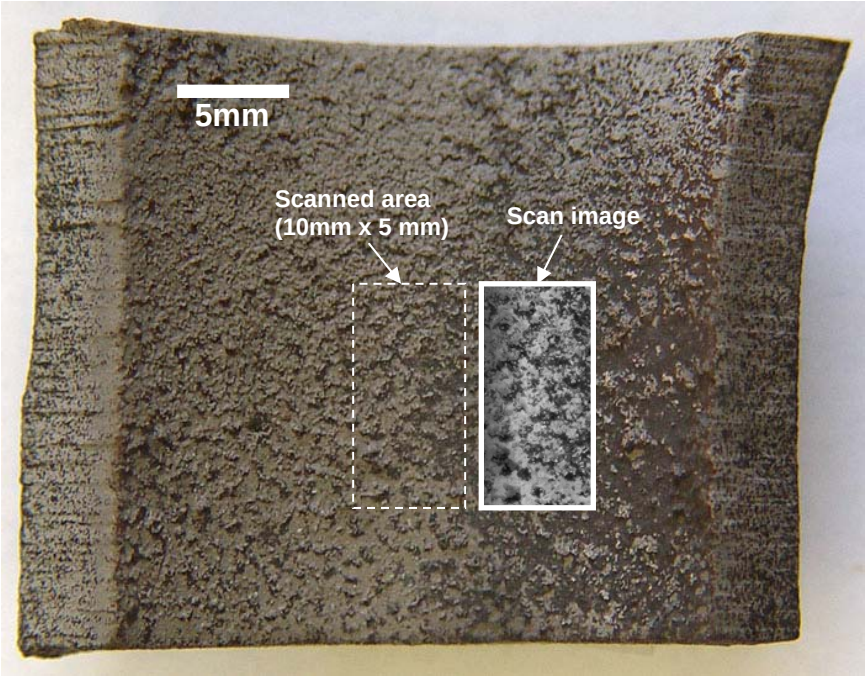

Fig. 4. Laser-backscatter scan image and corresponding TBC surface of thermal-cycled TBC specimen #9.

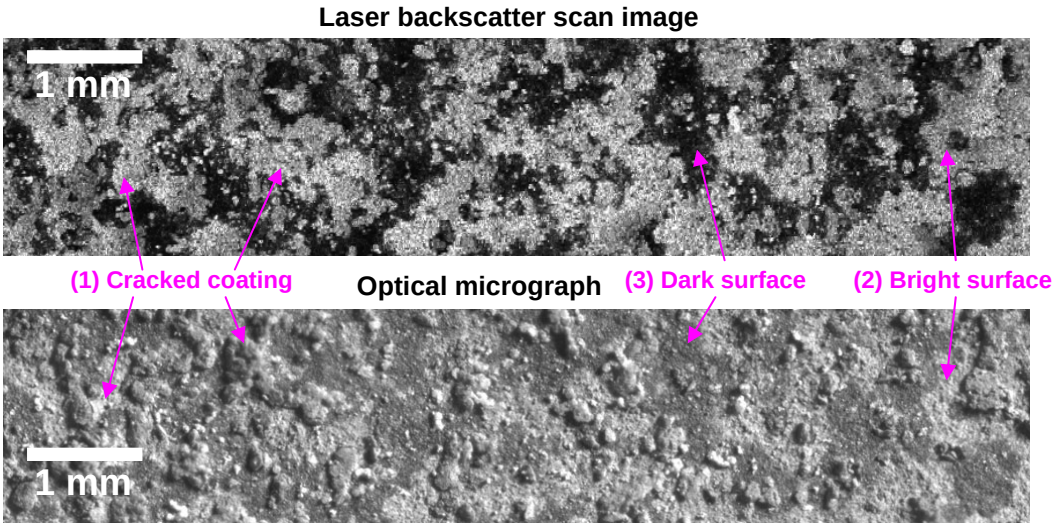

Fig. 5. Detailed comparison of laser-scatter scan image with surface micrograph for thermal-cycled TBC specimen #9.

2. Development of High Depth-Resolution Algorithm for Thermal Tomography

Thermal tomography is a new 3D imaging method that can construct 3D data for a test sample similar to those obtained by the 3D x-ray CT method. Thermal tomography has been used for TBC inspection under this project and has produced detailed data for characterization of TBC quality and detection of TBC flaws such as delamination. The current algorithm for depth data construction in thermal tomography is based on a simple formulation, which suffers from a linear degradation in depth (and lateral) resolution with depth. Therefore, the current algorithm is best suited for imaging relatively shallow layers like TBCs or detecting larger flaws in deeper depths. To improve the depth resolution, a new depth reconstruction algorithm was developed. This algorithm is based on a rigorous convolution formulation as shown below:

$$e_a(t) = e_a(z) = \int_0^{\infty} e(l)\, r(z/l)\, dl \,,$$

where $e_a(t)$ is measured apparent effusivity, $e(l)$ is the real material effusivity along depth l or z, and $r(z/l)$ is a response function. The deconvolution solution of $e(z)$ can completely eliminate the depth diffusion effect at the back surface of a test sample. This formulation will be further evaluated for application in TBC characterization.

Status of Milestones

Current ANL milestones are on schedule.

Communications/Visits/Travel

J.G. Sun presented two papers at the 34th International Conference and Exposition on Advanced Ceramics and Composites, Daytona Beach, FL, January 24-29, 2010.

J.G. Sun plans to attend the 2010 Vehicle Technologies Annual Merit Review and Peer Evaluation Meeting, June 7-11, 2010, in Washington, D.C.

Problems Encountered

None this period.

Publications

J.G. Sun, “Thermal Property Measurement for Thermal Barrier Coatings by Thermal Imaging Method,” paper presented at the American Ceramic Society’s 34th International Conference and Exposition on Advanced Ceramics and Composites, Daytona Beach, FL, January 24-29, 2010.

J.G. Sun, “Thermal Tomographic Imaging for Nondestructive Evaluation of Ceramic Composite Materials” paper presented at the American Ceramic Society’s 34th International Conference and Exposition on Advanced Ceramics and Composites, Daytona Beach, FL, January 24-29, 2010.

Agreement 18570: Engine Materials Compatibility with Alternate Fuels

S. J. Pawel
Oak Ridge National Laboratory

Objective/Scope

The purpose of this Cooperative Research and Development Agreement (CRADA) between Oak Ridge National Laboratory and USCAR is to systematically evaluate compatibility between engine materials and ethanol fuel blends over a range of temperatures consistent with engine operation. Four primary tasks are included in the overall program:

1) surface analysis of materials exposed in field and lab exposures
2) in-situ extraction of gas and/or fluid from the valve seat crevice
3) development of electrochemical testing protocols
4) laboratory corrosion exposures of coupon materials

Technical Highlights

The USCAR Partners identified three cylinder heads suitable for surface analysis (task 1) and these have been received at ORNL. Two of the cylinder heads were used in engine tests, and the third cylinder head represents an unexposed engine that will be used to establish the baseline surface condition (composition, film thickness, etc.) of the components. Surface analysis emphasis in this case will be on the Fe-based valve insert and the cast aluminum cylinder it contacts. Figure 1 is a representative image of the components shipped to ORNL for analysis. Methods to cut/section the engine for analysis without altering the surface chemistry/condition of interest must be established. An additional cylinder head has been received at ORNL for modification as part of task 2.

Autoclaves to be used for electrochemical testing of Fe-based and Al-based engine alloys in various fuel compositions and temperature/pressure conditions (task 3) have been procured. Figure 2 shows the major components of the equipment. Other components (reference electrodes, specimen holders, etc) are being fabricated, and the next challenge is to identify methods to render suitable test specimens from the engine materials.

Status of FY2010 Milestones

Work initiated.

Communications/Visits/Travel

Routine electronic mail and telephone contact is being maintained between the USCAR Technical Lead and the ORNL PI. No travel occurred this quarter.

Problems Encountered

None

Publications/Presentations/Awards
None

References
None

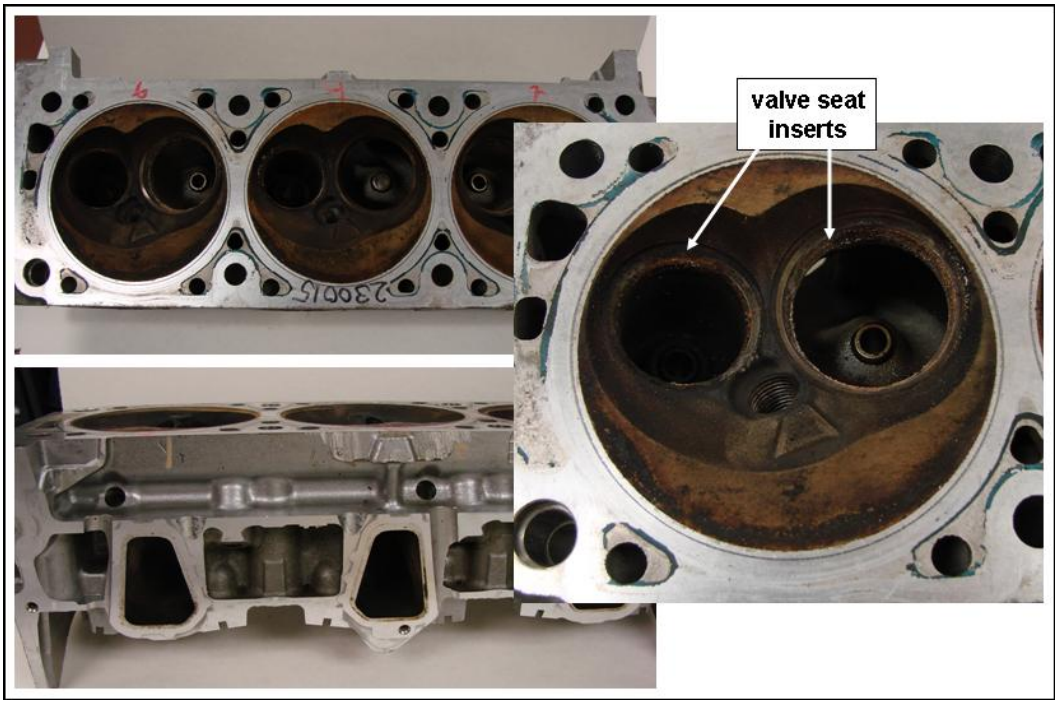

Figure 1. Views of a representative cylinder head sent to ORNL for surface analysis. The component shown here is one side of a V6 engine. Analysis of corrosion in/around the valve seat crevice (behind the inserts) is of primary interest.

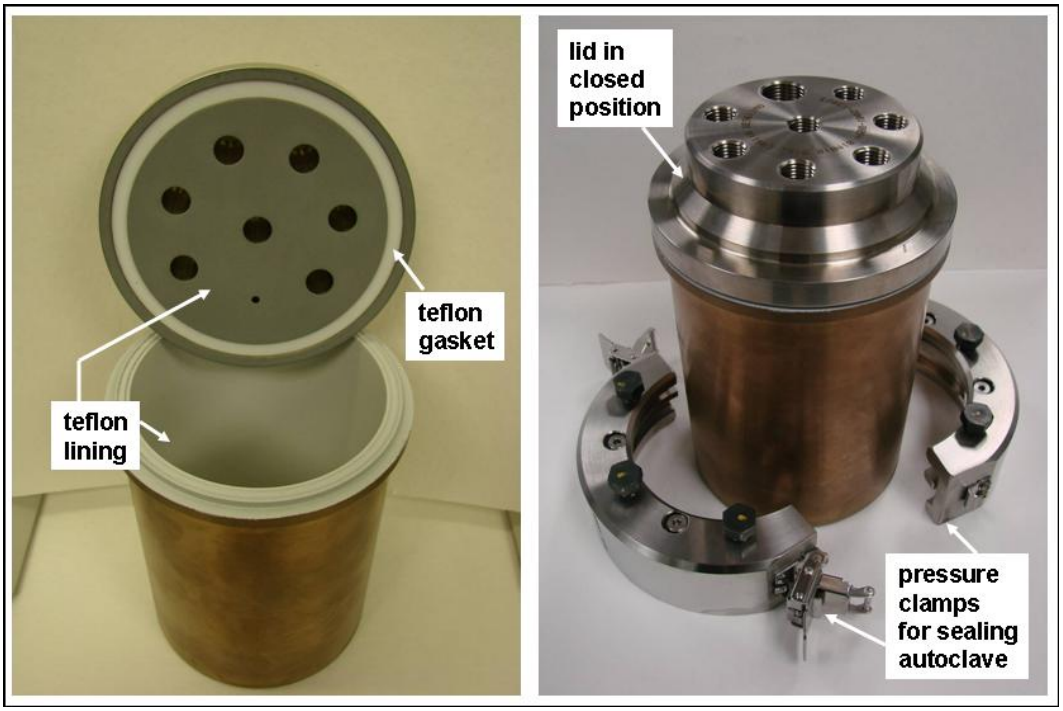

Figure 2. One of the autoclaves to be used for electrochemical testing. On the left, the internal surfaces (Teflon coated/lined) exposed to fuel mixtures at high temperatures are shown. On the right, the autoclave is pictured in the closed position along with the sealing clamp. The lid has a number of penetrations to allow for reference and auxiliary electrodes, specimens, temperature monitoring, and cover gas manipulation. The autoclave body and head are both 316 stainless steel, as are the pressure clamps and other metallic components.

Agreement 18571: Materials Issues Associated with Exhaust Gas Recirculation Systems

M. J. Lance, C. S. Sluder and J. M. E. Storey
Oak Ridge National Laboratory

Objective/Scope

Provide information to industry specialists about fouling deposit properties so as to enable improved models and potential design improvements to reduce fouling and its impact on the performance of EGR (exhaust gas recirculation) coolers.

Technical Highlights

In February of 2009, a consortium consisting of engineers responsible for EGR systems was assembled from nine diesel engine manufacturers and surveyed to identify the biggest problems facing EGR systems. EGR cooler fouling was identified as a very critical concern. Each member of the EGR consortium agreed to provide a cooler that had seen enough operation to categorize it as 'half-useful-life'. Of the nine members, the seven companies that currently use HP-EGR all sent at least one fouled cooler for analysis with the results to be shared with the entire consortium. Recent results of this survey will be discussed below.

X-ray Photoelectron Spectroscopy (XPS) was collected on all deposit samples and the carbon 1s spectra are presented in Figure 1. All samples exhibited the C-C bonding peak at 285 eV, and with the exception of cooler deposit #5, all showed the C-O bonding peak at 289 eV.

Hydrocarbon profiles were measured with gas chromatography-mass spectrometry (GC-MS). Four species that indicate different hydrocarbon origins (fuel, oil and oxidized fuel) are listed in Table 1. Most samples had concentrations of individual hydrocarbon species below 1 ng per µg of deposit. Cooler #3 had high amounts of fuel hydrocarbons and partially-oxidized fuel but no heavy hydrocarbons from oil. Cooler #5 had large amounts of both fuel and oil hydrocarbon but no oxidized fuel which compares well to the XPS results which also showed no C-O bonding in this deposit.

Status of FY2010 Milestones

Complete chemical and microstructural characterization of industry provided coolers. (09/10) *On Schedule.*

Communications/Visits/Travel

Engineers from John Deere visited at the end of March to discuss EGR fouling.

Problems Encountered

None

Publications/Presentations/Awards

None

References

None

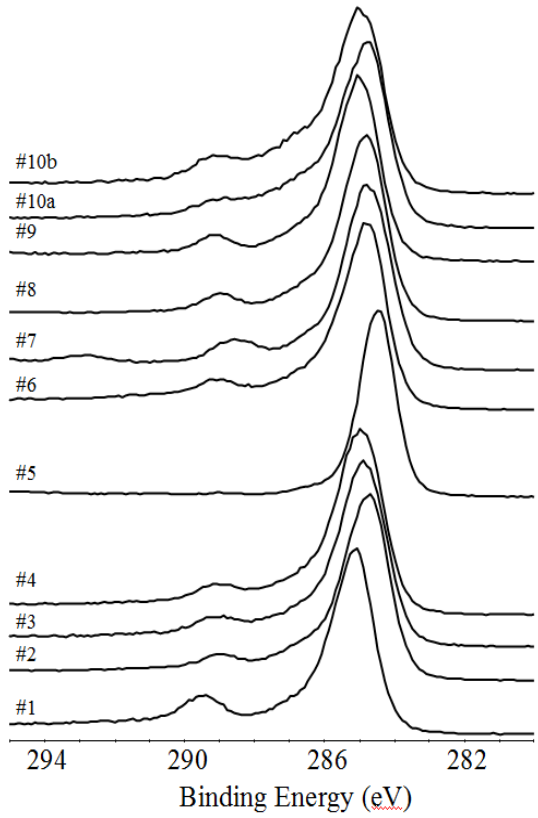

Figure 1. Carbon 1s spectra measured by X-ray Photoelectron Spectroscopy (XPS). The peak positions are uncorrected for sample charging. The large peak around 285 eV is from C-C bonding and the smaller peak around 289 eV is from C-O bonding.

Table 1. Estimated mass (in ng/µg) of four common hydrocarbon species in the cooler deposits measured by GC-MS. Naphthalene and nonadecane correspond to aromatic and alkane species in diesel fuel, respectively. Pentacosane is a heavier hydrocarbon species more common in oil. Naphthalenic anhydride indicates partially oxidized fuel.

Cooler #	*naphthalene*	*nonadecane*	*pentacosane*	*naphthalenic anhydride*
1	0.0	0.3	0.0	0.2
2	0.6	0.2	0.5	0.0
3	18.0	8.4	0.0	5.4
4	0.4	1.5	0.6	0.6
5	11.0	87.8	49.6	0.0
6	0.5	1.6	1.1	0.4
7	0.0	3.9	0.0	0.2
8	0.1	0.3	2.7	0.1
9	0.9	0.1	0.0	0.3
10a	0.0	1.7	0.0	1.0
10b	0.0	0.0	0.0	0.0

Agreement 19202: Titanium Friction and Wear
(Surface Engineering of Bearing Components)

Peter Blau and Dinesh Bansal
Oak Ridge National Laboratory

Objective/Scope

Energy efficiency and durability of internal combustion engines (ICEs), whether fueled by conventional or alternative fuels, benefits from the utilization of lightweight materials. Examples include fiber composites and alloys of aluminum, magnesium, and titanium. While such materials offer attractive efficiency gains, their use also presents technical and economic challenges. The nature of those challenges depends upon which materials and engine components are involved. One class of applications involves tribological applications: that is, those which concern friction, wear, and lubrication. Studies in the United States, Japan, and the United Kingdom have shown that mechanical losses comprise about fifteen percent of the energy dissipation from fuel in a typical ICE, and that of those, energy losses by friction comprise about eighty percent. The two major subsystems in terms of engine frictional losses are the piston ring/cylinder interface and the engine bearings. Past work at ORNL and other organizations has focused on the piston ring/cylinder interface. The current project, beginning in FY 2010, not only addresses the second contributor: connecting rod bearings, but it also demonstrates surface engineering technologies that could benefit other transportation applications as well.

The objective of this project is to enable the use of lightweight titanium (Ti) alloys in connecting rods (CRs) by applying integrated surface-engineering methods to effect significant improvements in the lubricity and durability. The goal is to employ surface engineering methods that allow the Ti surfaces to be used without the need for additional bearing inserts or heavier bearing materials. Surface engineering, in the present context, is defined as any process that aims to improve the functionality of a solid surface by altering its geometric form (shape, texture, or roughness), its chemical composition, or the microstructure of the materials of which it is composed. This work capitalizes both on recent developments in Ti processing technology to reduce raw material cost, and the capabilities of ORNL to effect changes in the surface-critical properties via a variety of potential treatment routes. Three phases of this effort are planned:

1. *Researching current and emerging surface treatment technologies*. Laboratory-scale testing of candidate materials using simple coupons, and the construction of a variable loading spectrum bearing wear and friction apparatus. (Year 1)
2. *Simulative, variable load testing*. Tests will be performed on selected surface engineered titanium samples using the bearing test apparatus to be designed and built during Phase 1. (Years 2 and 3)
3. *Scale-up testing*. Scale-up and dynamometer testing of a titanium connecting rod produced using the preferred surface engineering (Year 3)

Technical Highlights

Baseline testing of titanium alloy Ti-6Al-4V. A supply of rolled plate stock of Ti alloy Ti-6Al-4V was obtained for use in Phase 1 laboratory-scale baseline testing and screening of surface treatments. Its nominal composition (in wt%) is: 5-5 – 6.8 Al; 3.5 – 4.5 V; 0.3 Fe; 0.2 O; 0.1 C; 0.05 N; ~ 0.01 H wt%; balance Ti) This alloy is by far the most commonly used Ti aerospace alloy, and a great deal is known about its metallurgy, processing, heat treatment, and properties. Barring some unforeseen technical problem, this alloy will serve as the standard substrate on which to assess the effects of candidate surface engineering methods.

Oscillating motion is common in engine parts such as piston rings sliding on cylinder bores, fuel injector plungers in their bores, and piston wrist pins in the small end bearings of connecting rods. Therefore, the test method selected for pre-screening of candidate surface engineering methods in Year 1 is based on ASTM standard G 133 "Standard Test Method for Linearly Reciprocating Ball-on-Flat Sliding Wear." The development effort for that standard was led by ORNL under DOE sponsorship in the early 1990s. It involves a fixed sphere oscillating on a flat surface under a fixed normal force (load). ASTM G 133 has two procedures: "A" that was developed for non-lubricated metals and ceramics, and "B" that was designed for lubricated metals and ceramics. Procedure B uses more severe load and speed conditions because wear is generated more slowly during lubricated contact and accelerated testing is required. In these pre-screening experiments, we are using a modified procedure B that does not require elevated temperature. The operating conditions are summarized in Table 1 and a schematic of the set-up is shown in Figure 1. In the current pre-screening work, we selected AISI 52100 high Cr bearing steel as the standard counterface (ball) material. In later stages of this effort, a steel more similar to crankshaft steel will likely be used instead. Friction measurements were made using a data acquisition software package (LabView™) at 100 or 200 data per second, recorded and averaged for 5 seconds at 20 second intervals during the test. Therefore, there were 50 friction coefficient data points collected for each Procedure A test and 100 points for each Procedure B-mod. test. Both the ball and flat specimens were cleaned in acetone and 2-propanol prior to testing.

The first baseline tests, using Procedures A and Procedure B-mod, were performed using Ti-6Al-4V as the flat specimen material. Flat specimens, 25 x 25 mm square, were prepared to a final 600-grit SiC, wet hand-ground finish. The lubricant used was an analyzed sample of diesel engine test oil and was applied so as to produce a 1-2 mm-deep puddle surrounding the wear path. The lubricant was observed to remain on the wear path for the duration of the test. The engine-conditioned oil was obtained from Southwest Research Institute, San Antonio, TX. It consisted of a 15W40 commercial diesel engine oil (Valvoline) retrieved from a standard Mack T-11 test that ran for 252 hrs. [Note: This oil came from the same sample as was used for a recently-completed ASTM five-laboratory friction and wear testing program to validate standard ASTM G 181 on ring and liner friction.]

Table 1. ASTM G 133 Test Conditions.

Test Variable	Procedure A	Procedure B
Applied load (N)	25.	200.
Sliding stroke length (mm)	10.	10
Speed of oscillation (cycles/s)	5	10
Test length (s)	1000.	2000.
Sliding distance (m)	100.	400.
Surrounding atmosphere	ambient air	ambient air
Relative humidity (%)	40 - 60	not specified
Lubrication method	none	surface immersion
Lubricant temperature (C)	not applicable	150 (Note 1)
Air temperature (C)	22 +/- 3	not specified
Ball (slider) diameter (mm)	9.525	9.525

Note 1: For this work, the lubricant was used at room temperature. Therefore, Procedure B will be reported as being modified ('B-mod')

Typical friction coefficient versus time for the baseline tests on non-treated titanium are summarized in Figures 2(a) and (b). The oil-lubricated test had to be terminated after only 1.5 minutes of running due to excessive vibration and chatter. Ideally, the friction coefficients for engine bearing applications should be no higher than 0.08, so neither test result was satisfactory from that standpoint. Figures 3(a) and (b) show the wear tracks associated with the two baseline tests, respectively. Clearly, non-treated Ti-6Al-4V is unsuitable for lubricated sliding in engine oil.

A series of surface modified Ti test coupons to compare with the baseline results has either been obtained or are in the process of being obtained for further laboratory study. These include oxygen-diffused Ti surfaces, previously shown by ORNL researchers to perform well under oil lubricated conditions [1], titanium nitride coatings developed for use with cutting tool materials, and a novel infra-red processed Ti composite surface developed by ORNL researchers for high-temperature galling resistance [2].

Future Plans. In the upcoming quarter, plans include additional testing of surface modified and coated Ti alloys. In particular, oxygen diffused surfaces, in situ Ti composite surfaces, and titanium nitride coated surfaces will be tested. In addition, a workbench and drive system components for the spectrum load actuated tribotester will be obtained.

Status of FY 2010 Milestones

Design friction and wear testing apparatus to simulate connecting rod motions, loads, and speeds, and complete a series of baseline experiments on small test coupons of candidate titanium alloys, with and without surface treatments. **(09/10)** *Status: on schedule***.**

Communications/Visits/Travel
None

Problems Encountered
None

Publications/Presentations/Awards
None

References

[1] J. Qu, P. J. Blau, J. Y. Howe, H. M. Meyer III (2009) "Oxygen diffusion enables anti-wear boundary film formation on titanium surfaces in zinc-dialkyl-dithiophosphate (ZDDP)-containing lubricants," *Scripta Materialia*, Vol. 60 (10), pp. 886-889.

[2] P. J. Blau, D. L. Erdman III, E. Ohriner, and B. C. Jolly (2010) "High-Temperature Galling Characteristics of Ti-6Al-4V with and without Surface Treatments," accepted for presentation, Soc. of Tribologists and Lubrication Engineers Annual Meeting, Las Vegas, NV, May 16-20.

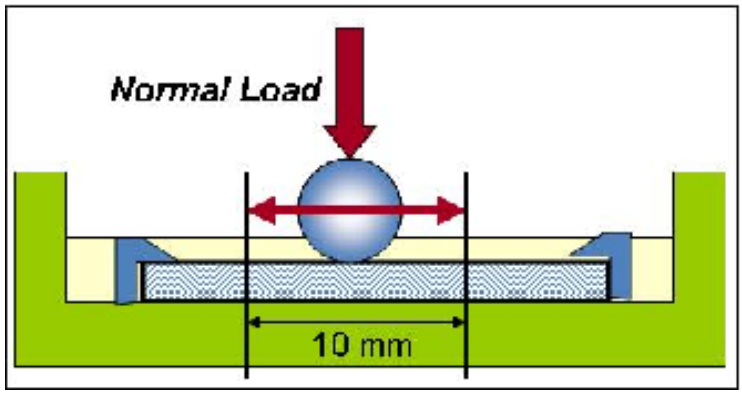

Figure 1. Reciprocating ball-on-flat test geometry

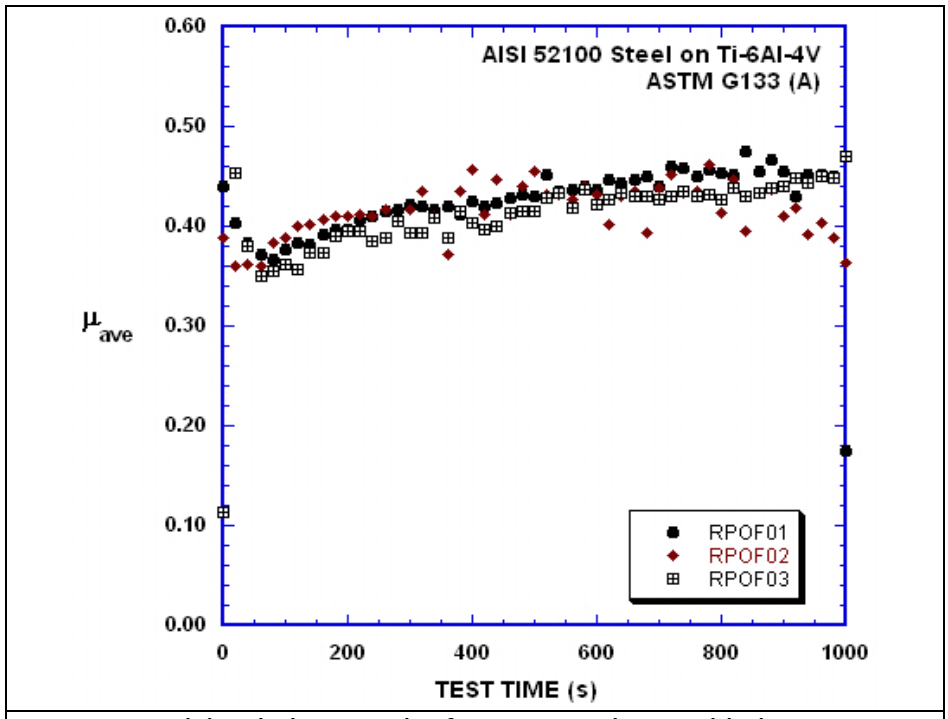

(a) Friction results from Procedure A (dry)

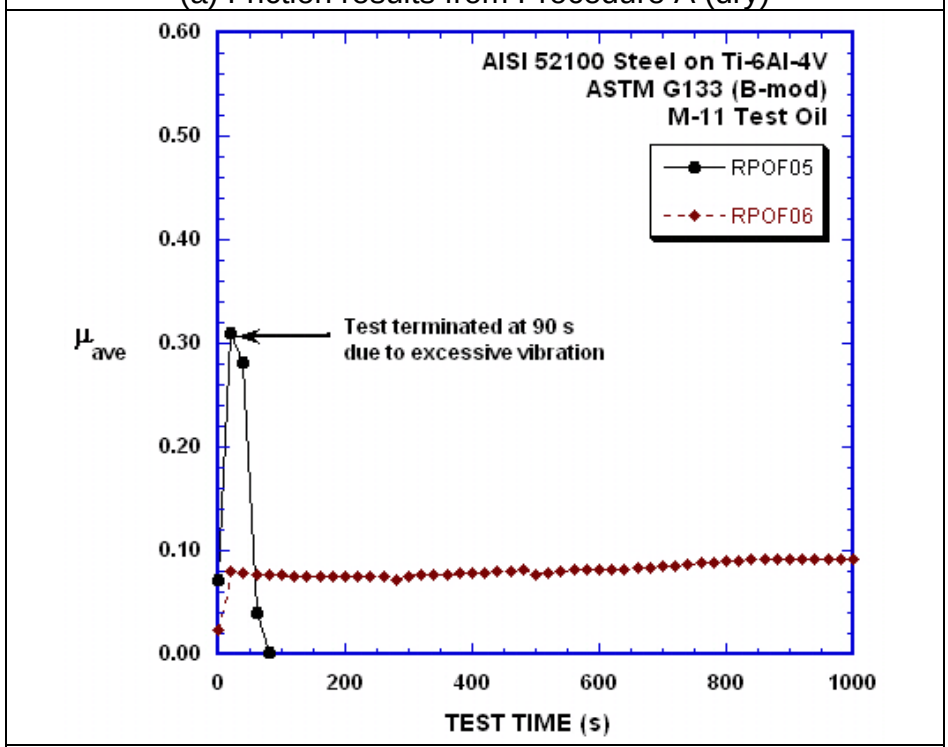

(b) Friction results from Procedure B-mod. (used oil)

Figure 2. Friction coefficient versus time for (a) three tests of AISI 52100 steel sliding on Ti-6Al-4V dry at 25 N load, and (b) two tests of the same material combination, but in used oil at 200 N load. The first test in oil was terminated 90 seconds after the start due to excessive vibration, but the second performed acceptably. Consistency of performance is a significant concern.

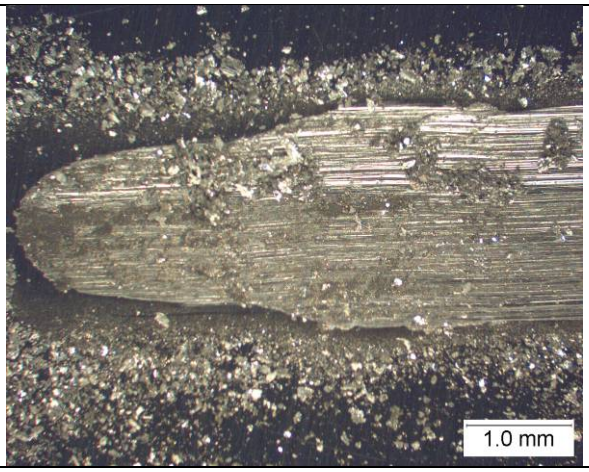

(a) Wear track on bare Ti tested dry

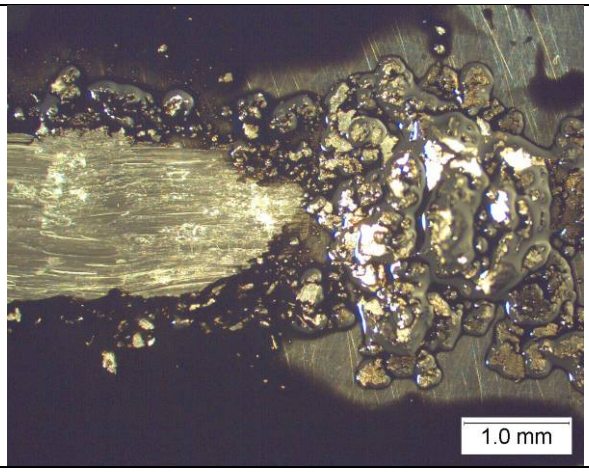

(b) Wear track on bare Ti, tested in used diesel engine oil

Figure 3. Initial reciprocating sliding wear tests of steel sliding on Ti-6Al-4V alloy dry (a) and in used oil (b) showed the production of myriad shiny metallic wear particles. This degree of wear is wholly unacceptable for a bearing surface.

Agreement 9130: Development of Materials Analysis Tools for Catalyst Characterization

Thomas Watkins, Larry Allard, Michael Lance, Harry Meyer
Oak Ridge National Laboratory

Krishna Kamasamudram, Alex Yezerets
Cummins Inc.

Objective

The objective of this effort is to produce a quantitative understanding of the process/product interdependence leading to catalyst systems with improved final product quality, resulting in diesel emission levels that meet the prevailing emission requirements.

Goals, Barriers, Relevance & Integration

In the study area of OVT's Advanced Combustion Engine research, the *goals* are to (1) improve commercial vehicle engine efficiency by at least 20% and (2) to achieve engine system cost, durability and emissions targets. This project addresses the three *barriers* related to the Emission Control System in this study area: Improving durability, numerous components and costly precious metal content. This project is *relevant* to these goals as the understanding of materials changes underlying the Ammonia Oxidation (AMOX) catalyst performance degradation with age increases, efficient and durable AMOX with higher NO_x conversion efficiencies can be attained. This minimizes constraints on engine-out NO_x emissions and allowing engines to be tuned for optimal fuel efficiency, cost and durability. This project supports clean diesel, which increases acceptance by the public. Larger acceptance, in turn, results in larger percentages of conversion to diesel, with the resulting reduction in petroleum usage/dependency upon foreign oil. This project is *integrated* within Vehicle Technologies program as it utilizes characterization tools acquired and maintained by the High Temperature Materials Laboratory (HTML) Program.

Technical Progress

The main focus in FY 2011 will be to continue the ammonia oxidation (AMOX) catalyst characterization of a practically-relevant zeolite catalyst subjected to hydrothermal aging for lifetime prediction model input. The technical approach will be as before: experimentally characterize materials, supplied by Cummins, from all stages of the catalyst's lifecycle: fresh, de-greened, aged, regenerated, on-engine and off-engine, etc. Determinations include: crystal structure, morphology, phase distribution, particle size and surface species of catalytically active materials; seek the atomic mechanisms and chemistry of adsorption and regeneration processes. Ultimately, an understanding of the thermal and hydrothermal aging processes and other degradation mechanisms is sought throughout the lifecycle of the catalytic material.

New samples were received in January 2010. Through 2009, progress had been slowed considerably due to sample unavailability because of Cummins' 2010 product

launch focus. The x-ray diffraction pattern of a zeolite-based AMOX catalyst on a cordierite honeycomb support is shown (see Figure 1). X-ray Photoelectron Spectroscopy was conducted in three location of a honeycomb core which was cut in half. Figure 2 shows the composition and valence at these three locations within the as-received AMOX sample. The Si 2P, Al 2p and O 1s core level spectra identical for all 3 sample regions which is consistent with literature for zeolites. Similarly, the Fe 2P core level spectra are identical for all three sample regions and indicate Fe3+. This AMOX zeolite shows significantly higher Fe concentrations than prior SCR samples, which should facilitate detection and characterization of the Fe species by TEM techniques.

Meetings

Thomas Watkins and Michael Lance travelled to Columbus, IN for technical discussions related to the CRADA on December 1, 2009.

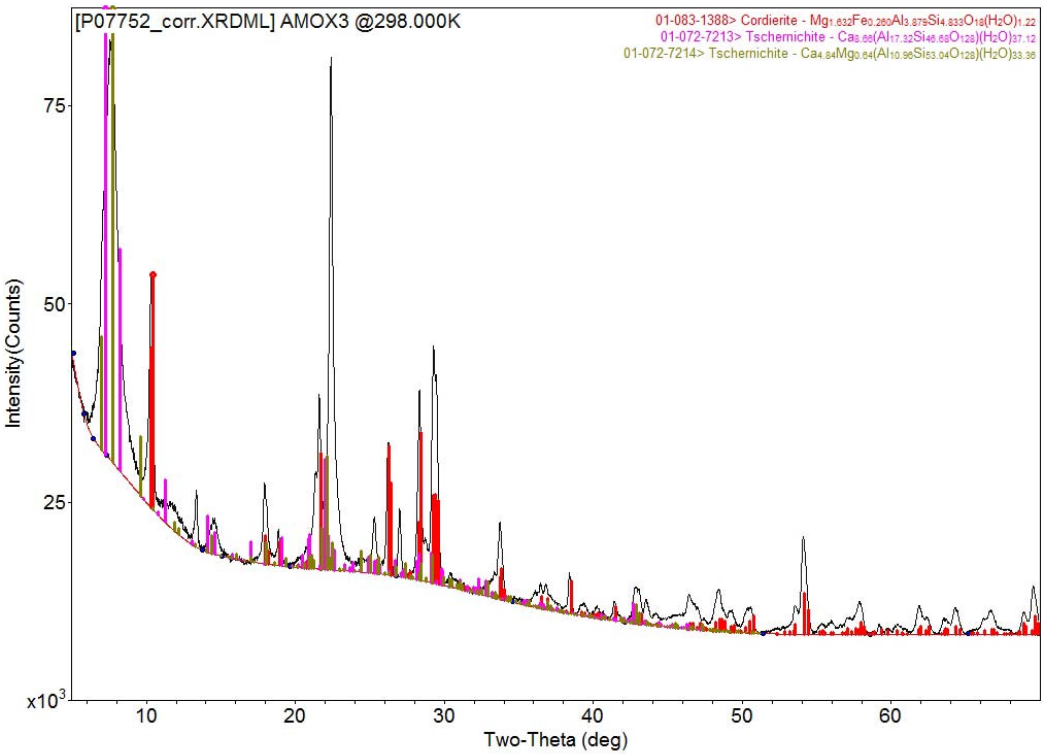

Figure 1 - The x-ray diffraction pattern of an AMOX catalyst.

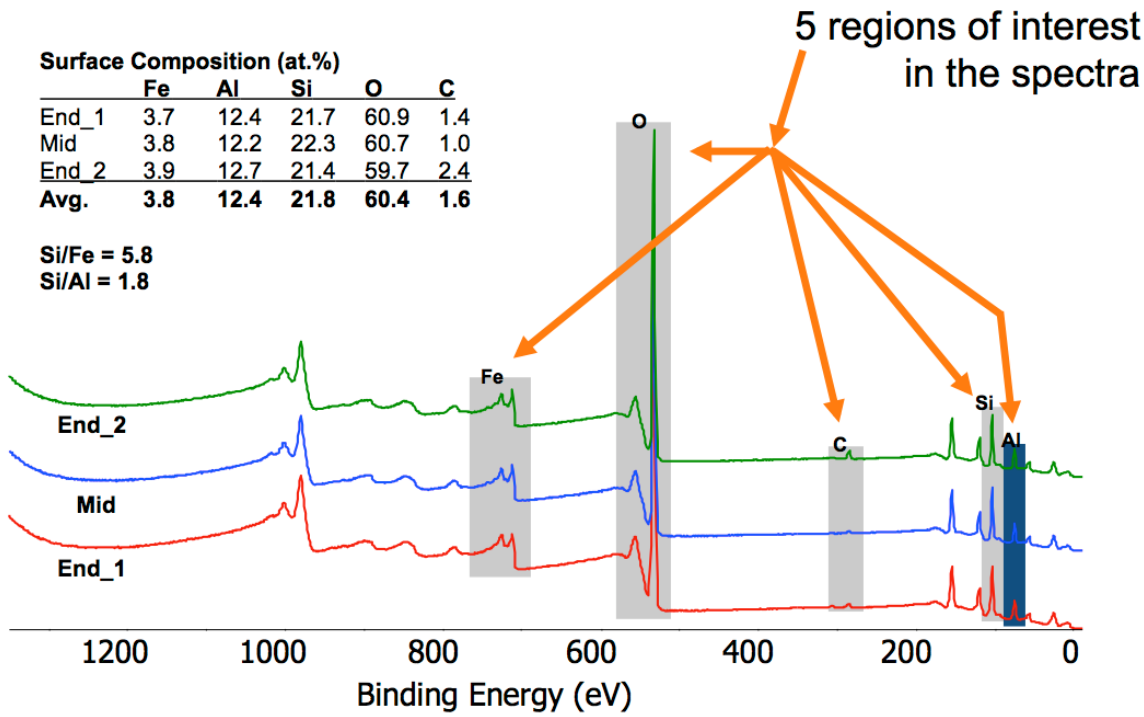

Figure 2 - The intensity (arb. units) as a function of binding energy for the as-received AMOX sample. The Al:Si:Fe assume Al_2O_3, SiO_2, and Fe_2O_3 are present. Further, the adsorbed water O 1s signal was ignored. The metal/oxygen ratio was found to be 0.68 and it is typically 0.59, indicating a slight oxygen deficiency in the near surface region

Agreement 10635: Catalysis by First Principles - Can Theoretical Modeling and Experiments Play a Complimentary Role in Catalysis?

C. Narula, M. Moses DeBusk, Xiaofan Yang
Oak Ridge National Laboratory

Objective/Scope

This research focuses on an integrated approach between computational modeling and experimental development, design and testing of new catalyst materials, that we believe will rapidly identify the key physiochemical parameters necessary for improving the catalytic efficiency of these materials. The results will have direct impact on the optimal design, performance, and durability of supported catalysts employed in emission treatment; e.g., lean NO_x catalyst, three-way catalysts, oxidation catalysts, and lean NO_x traps etc.

The typical solid catalyst consists of nano-particles on porous supports. The development of new catalytic materials is still dominated by trial and error methods, even though the experimental and theoretical bases for their characterization have improved dramatically in recent years. Although it has been successful, the empirical development of catalytic materials is time consuming and expensive and brings no guarantees of success. Part of the difficulty is that most catalytic materials are highly non-uniform and complex, and most characterization methods provide only average structural data. Now, with improved capabilities for synthesis of nearly uniform catalysts, which offer the prospects of high selectivity as well as susceptibility to incisive characterization combined with state-of-the science characterization methods, including those that allow imaging of individual catalytic sites, we have compelling opportunity to markedly accelerate the advancement of the science and technology of catalysis.

Computational approaches, on the other hand, have been limited to examining processes and phenomena using models that had been much simplified in comparison to real materials. This limitation was mainly a consequence of limitations in computer hardware and in the development of sophisticated algorithms that are computationally efficient. In particular, experimental catalysis has not benefited from the recent advances in high performance computing that enables more realistic simulations (empirical and first-principles) of large ensemble atoms including the local environment of a catalyst site in heterogeneous catalysis. These types of simulations, when combined with incisive microscopic and spectroscopic characterization of catalysts, can lead to a much deeper understanding of the reaction chemistry that is difficult to decipher from experimental work alone.

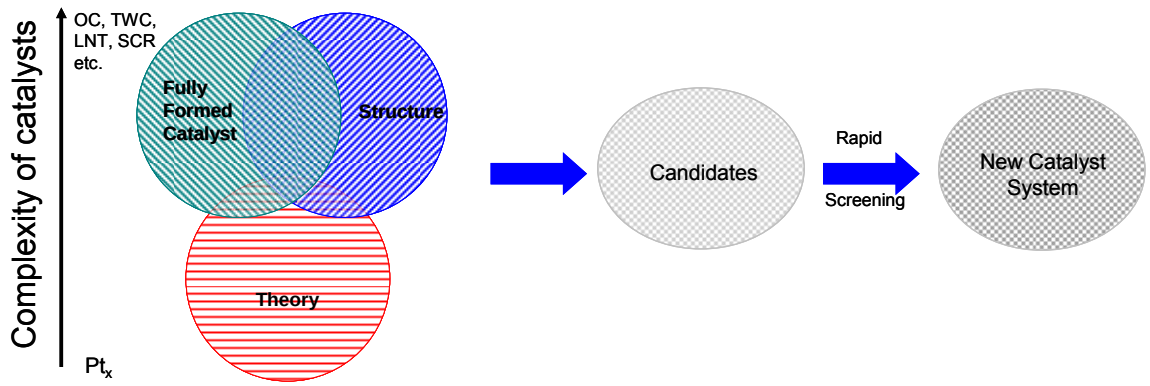

Thus, a protocol to systematically find the optimum catalyst can be developed that combines the power of theory and experiment for atomistic design of catalytically active sites and can translate the fundamental insights gained directly to a complete catalyst system that can be technically deployed.

Although it is beyond doubt computationally challenging, the study of surface, nanometer-sized, metal clusters may be accomplished by merging state-of-the-art, density-functional-based, electronic-structure techniques and molecular-dynamic techniques. These techniques provide accurate energetics, force, and electronic information. Theoretical work must be based on electronic-structure methods, as opposed to more empirical-based techniques, so as to provide realistic energetics and direct electronic information.

A computationally complex system, in principle, will be a model of a simple catalyst that can be synthesized and evaluated in the laboratory. It is important to point out that such a system for experimentalist will be an idealized simple model catalyst system that will probably model a “real-world” catalyst. Thus it is conceivable that “computationally complex but experimentally simple” systems can be examined by both theoretical models and experimental work to forecast improvements in catalyst systems.

We have focused on the oxidation catalyst to develop and demonstrate catalyst by design protocol as a prelude to developing catalyst by design protocols for complex emission treatment catalysts; e.g., TWCs, NO_x traps, and HC-SCR catalysts. Our goals are as follows:

- Our theoretical goal is to carry out the calculation and simulation of realistic supported Pt nanoparticle systems (i.e., those equivalent to experiment), in particular by addressing the issues of complex cluster geometries on local bonding effects that determine reactivity. As such, we expect in combination with experiment to identify relevant clusters, and to determine the electronic properties of these clusters.
- Our experimental goal is to synthesize metal carbonyl clusters, decarbonylated metal clusters, sub-nanometer metal particles, and metallic particles (~5 nm) on alumina (commercial high surface area, sol-gel processed, and mesoporous molecular sieve), characterize them employing modern techniques including

Aberration Corrected Electron Microscope (ACEM), and evaluate their CO, NO_x, and HC oxidation activity.

- This approach will allow us to identify the catalyst sites that are responsible for CO, NO_x, and HC oxidation. We will then address support-cluster interaction and design of new durable catalysts systems that can withstand the prolonged operations.

Technical Highlights

Our theoretical studies on single platinum atoms supported on θ-alumina slab shows that the platinum atom is in zero oxidation state. This result is very different from that reported in literature on single platinum atoms supported on α-alumina or simplified models of γ-alumina where a platinum atom generally has an unpaired electron. This also means that mechanism of CO, NO_x, or HC oxidation on Pt(0) will be different from that on Pt(I) or Pt(II). We plan to carry out first principle studies of CO oxidation on Pt atoms supported on θ-alumina slab.

Since our experimental work has already shown that the distribution of platinum on γ-alumina and θ-alumina is almost identical, and the surface properties and CO oxidation of both catalysts are identical, we propose that Pt supported on θ-alumina is a better model for Pt supported on γ-alumina than Pt supported on α-alumina or simplified models of γ-alumina.

Our next step involves substitution of platinum atoms from agglomerates with palladium to understand the energetics of the system that will enable us to synthesize more durable catalysts than the current generation of catalysts.

Theoretical Studies

We have previously summarized the results on DFT calculation of bulk θ-alumina, θ-alumina slab, and a single platinum atom on a θ-alumina slab. We also reported preliminary results on a charge neutral supercell of 420 atoms combining 2 x 3 x 3 cells and found the location of platinum to optimize in an environment identical to the one in 180-atom supercell [Figure 1]. We also optimized the single Pd, Ag, or Au atom adsorbed on the [010] surface of θ-alumina and found the adsorption energies for Pt, Pd, Au, and Ag are in the order of Pt>Pd>Au>Ag and are -62.29, -44.84, -20.21, and -13.23 Kcal/mole, respectively suggesting that the absorption of these atoms is exothermic.

The analysis of projected local density of state [LDOS] leads to a different bonding picture than that reported in literature for α-alumina or γ-alumina where platinum has unpaired electrons. The platinum d orbitals and s orbitals are occupied resulting in no unpaired electrons. The interaction of platinum orbitals with Op states results in O p_y orbitals shifting to lower energy. Bonding with two neighboring oxygen atoms and charge transfer to oxygen py orbitals result in no upaired electron on platinum atom. Formally, platinum is in zero oxidation state with d^{10} structure and is bonded to two oxygen atoms. The implication of this important result is that the mechanism of CO, NO,

or HC oxidation on sub-nanometer particles such as single atoms should be different from the large particles normally examined by DFT.

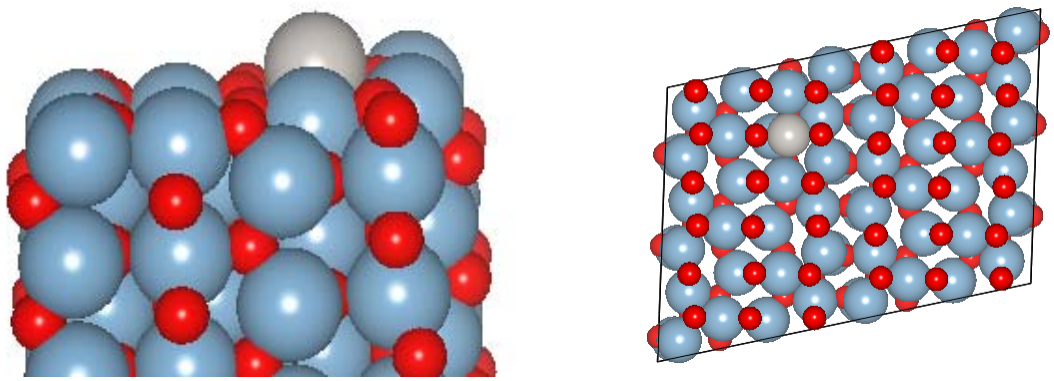

Figure 1: Pt location on a 2x4x2 (left) and 2x3x3 (right) supercells of 010 surface

The configuration of a palladium atom is $d^{10}s^{0}$, and it has higher energy valence d and s states than those for platinum. For Pd atoms, the Pd-O bond distances are 2.227 Å and 2.201 Å with an O-M-O angle of 134.54º. The distance from sub-surface Al is 2.49 Å and the Pd atom sits 0.86 Å above the cell surface. As expected, these distances are slightly larger that those for platinum atom but the bonding are identical to Pt atoms. For Au atoms, the Au-O bond distances are 2.45 Å and 2.69 Å with an O-M-O angle of 107.34º. The distance from sub-surface Al is 2.976 Å and nearest surface Al is 2.706 Å. The Au atom sits 1.519 Å above the cell surface. The Ag-O bond distances for Ag/θ-alumina are 2.483 and 2.549 Å with an O-Ag-O angle of 108.5º. The distance from sub-surface Al is 3.08 Å and from closest surface Al is 3.09 Å. Both Ag and Au are $d^{10}s^{1}$ atoms and the energy of their valence d and s orbitals are lower that that of valence orbitals of Pt. Since there is a magnetic moment of 1.0 associated with both atoms, they must be formally in oxidation state 2 (d^{9} species). This is supported by the fact that the s orbital is empty and d orbitals exhibit polarization and partial occupancy. This bonding picture is also different from Au or Ag on α-alumina where Au is bonded to an oxygen atom and Ag occupies a three-fold hollow site. The bonding picture Au/α-alumina suggest that Au orbitals are split by interaction with oxygen but remain filled. The s orbital also remains filled. Thus Au-O interaction is proposed to be a weak filled-filled one. The interaction of silver, on the other hand, is proposed to be an ionic one where Ag s states are vacated and do not participate in bonding.

Considering the facts (reported previously) that the Pt supported on γ-alumina and θ-alumina exhibit identical bimodal distribution of platinum (single atoms and 10-20 atom clusters) when examined by ACEM and have identical CO oxidation activity, we suggest that platinum on θ-alumina is a better representative of platinum on γ-alumina than the models reported in literature (platinum on α-alumina or platinum on simplified models of γ-alumina). As described previously, the structure of platinum on γ-alumina is uncertain due to uncertainty of the structure of γ-alumina.

We also summarized preliminary results on DFT structural studies of 2-atom and larger clusters of Platinum on a charge neutral supercell of 420 atoms combining 2 x 3 x 3 cells. Since 2x3x3 cell has four identical sites, we initiated our study of 2- and 4- Pt atoms on the surface with not bonding interaction with Pt atoms {Figure 2]. The impetus for this comes from our interest in comparing theoretical model with experimentally observed Pt agglomerates on alumina [Figure 3].

.

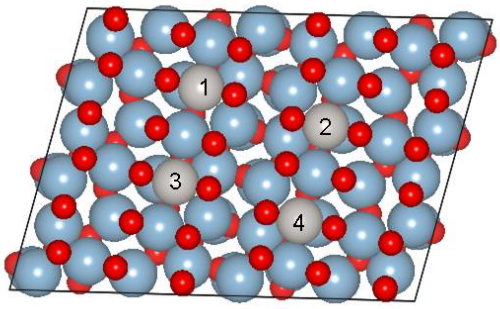

	OXYGEN	OXYGEN
Pt 1	2.192	2.132
Pt 2	2.202	2.129
Pt 3	2.135	2.214
Pt 4	2.138	2.214

Figure 2: Platinum atoms on 2x3x3 supercell

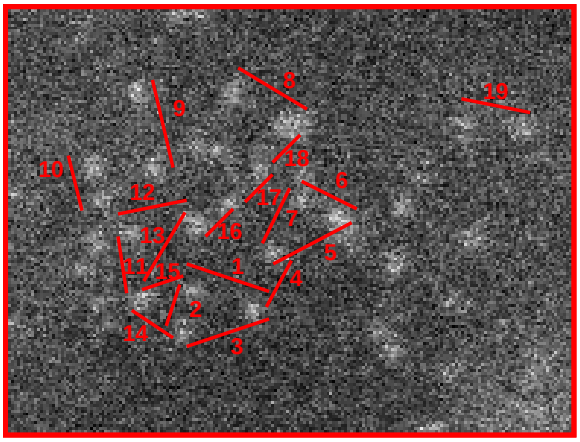

1	3.82	6	2.6	11	4.0	16	2.27
2	2.61	7	3.64	12	3.8	17	2.79
3	4.53	8	3.97	13	5.53	18	3.14
4	3.45	9	4.87	14	3.28	19	3.65
5	3.45	10	2.09	15	3.3		

Figure 3: Platinum agglomerates on θ-alumina

The measurement of Pt-Pt distances in a Pt agglomerate shows that most of the platinum atoms are not bonded to each other since Pt-Pt bonding distance is generally 2.5Å. Several of Pt atoms are even outside Pt-O-Pt bond distance which is ~3.2 Å (e.g. Pt-O and Pt-Pt distance in a complex 2.1 and 3.227 Å respectively and Pt-O-Pt angle is 100.6; Inorg. Chem. 27 (1988) 956). While some of the atoms are within Pt-O-Pt distance, most of them are too far from each other to have even Pt-O-Pt interaction. Interestingly, the calculated bond distance between Pt1-Pt3 is 5.7Å showing that the shortest non-bonded Pt-Pt bond distance is 5.7Å for two platinum atoms on 010 θ-alumina surfaces.

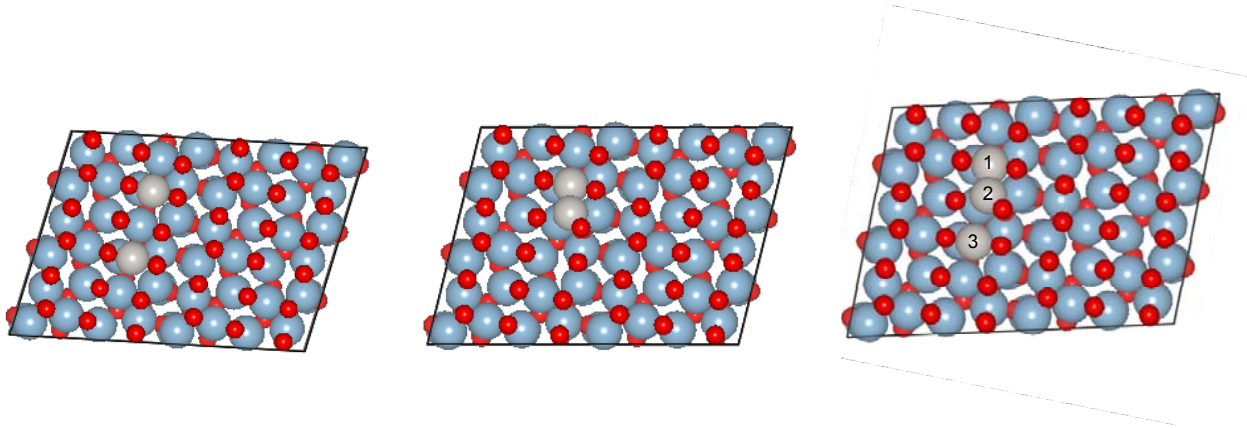

Figure 4: The models for 2 and 3-Pt atoms on 010 θ-alumina surfaces

We also calculated the energy barrier between two independent platinum atoms and two-bonded platinum atoms on 010 θ-alumina surfaces and found the two independent configuration favored by 1.27 Kcal/mole. Thus, the energetics does no seem to favor Pt clustering. Interestingly, a platinum atom bonded to platinum 1 and platinum 3 is not energetically favorable over a platinum atom bonded to platinum 1 and an independent platinum 3 configuration shown in Figure 4 right). While platinum 1 and 3 are bonded to two neighboring oxygen atoms, the platinum 2 atom is only bonded to platinum 1. The bonding analysis for this configuration is in progress and will be presented in the next quarterly report.

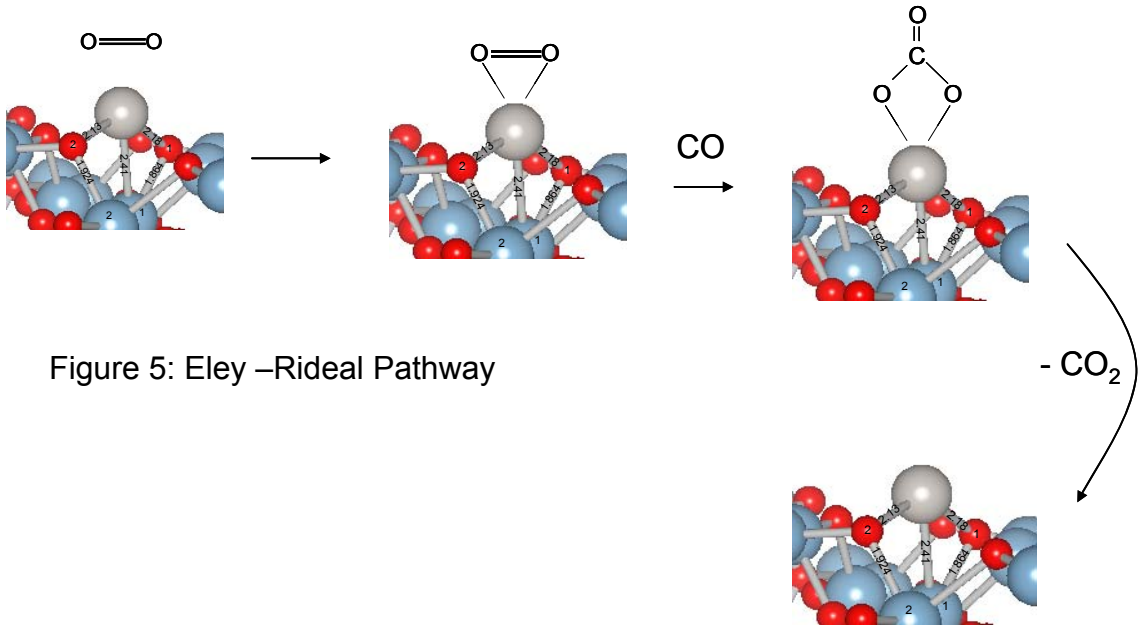

Figure 5: Eley –Rideal Pathway

Thus, the preliminary studies summarized here suggest that the platinum atoms prefer independent locations where they are in zero oxidation state and are bonded to two neighboring oxygen atoms. The agglomerates of platinum also do not exhibit Pt-Pt interaction. An important implication of this study is on the mechanism of CO or NOx

oxidation. The predominance of platinum atoms or agglomerates prevents adequate number of adjacent platinum atoms for Langmuir-Hinshelwood pathway for CO or NOx oxidation. This implies that Eley-Rideal pathways [Figure 5] can dominate for CO oxidation in sub-nanometer platinum. We have initiated studies of intermediates to determine the energetics of this pathway.

We have also carried out preliminary study of Pt-Pd clusters supported on 010 θ-alumina surfaces. Replacement of one platinum atom with one palladium atom in each of the three models shown in Figure 3 did not lead to any difference in the optimized structure except the Pd-O bond distances are larger than Pt-O bond distances.

Our next step will be to study palladium substituted platinum agglomerates.

Experimental Studies

As described in theoretical studies, Eley-Rideal mechanism appears to dominate for subnanometer Pt particles while Langmuir-Hinshelwood mechanism is established mechanism for large particles. We carried out experimental studies of CO-oxidation on sub nanometer Pt particles for extended period of time to observe transition from Eley-Rideal to Langmuir Hinshelwood and co-relate it with the nature of Pt particles. A sample was taken to 170ºC under CO oxidation conditions three times and held for total of 9h. The samples showed no change in initiation values at 160ºC and no drop in quantitative conversion observed during the extended monitoring at 170 ºC.

In order to be able to compare the results of theoretical models on palladium substituted platinum agglomerates, we have initiated studies to synthesize and characterize platinum-palladium agglomerates supported on alumina substrates.

We followed the procedure described by Toshima *et al.* (J. Chem. Soc. Faraday Trans., 1993, 89, 2537-2543) for the synthesis of bimetallic Pd-Pt clusters with different ratios in homogeneous size, around 1.5 nm, employing poly(N-vinyl-2-pyrrolidone) (PVP, average MW 40,000) to stabilize nanoparticles. This approach leads to nanometer clusters.

We are synthesizing trans-[(NH3)2Pt(C5H6N3O)2PdCl](NO3).H2O (Lippert et al., J. Am. Chem Soc., 113 (1991) 5129) which contains Pt-Pd bond to prepare subnanometer Pt-Pd agglomerates on alumina.

Next Steps: We plan to carry out the following tasks:

- We will carefully characterize palladium substituted platinum agglomerates and study their durability under CO, HC, and NO_x oxidation conditions and diesel emissions treatment conditions.
- Complete theoretical calculations on 10-20 atom platinum clusters supported on θ-alumina surface.
- Initiate CO oxidation theoretical studies on platinum single atoms supported on θ-alumina surface.

Other Activities

A joint project on lean NO_x treatment is on going with John Deere Co under work for others arrangement.

Communication/Visitors/Travel

C.K. Narula travelled to San Francisco to present a paper on March 25th at 229th American Chemical Society meeting.

Publications

1. C.K. Narula, X. Chen, M.G. Stocks, Unraveling the structure of metal atoms supported on alumina, Nature, (manuscript in preparation)
2. C.K. Narula, "Catalyst by Design – Bridging the Gap between Theory and Experiments at Nanoscale Level" Encyclopedia of Nanoscience and Nanotechnology, Vol. II, Taylor & Francis, New York, 2008, pp 771-782 (invited).
3. C.K. Narula, L.F. Allard, D.A. Blom, M. Moses-DeBusk, "Bridging the Gap between Theory and Experiments – Nano-structural Changes in Supported Catalysts under Operating Conditions" SAE-2008-01-0416, SAE Int. J. Mater. Manu., 1(2008) 182-188.
4. C.K. Narula, L.F. Allard, D.A. Blom, M.J. Moses, W. Shelton, W. Schneider, Y. Xu, "Catalysis by Design - Theoretical and Experimental Studies of Model Catalysts", SAE-2007-01-1018 (invited).
5. C.K. Narula, M.J. Moses, L.F. Allard, "Analysis of Microstructural Changes in Lean NO_x Trap Material Isolates Parameters Responsible for Activity Deterioration" SAE 2006-01-3420.
6. Y. Xu, W.A. Shelton, and W.F. Schneider, "The thermodynamic equilibrium compositions, structures, and reaction energies of Pt*x*O*y* (*x* = 1-3) clusters predicted from first principles," *Journal of Physical Chemistry B,* 110 (2006) 16591.
7. Y. Xu, W. A. Shelton, and W. F. Schneider, "Effect of particle size on the oxidizability of platinum clusters," *Journal of Physical Chemistry A*, 110 (2006) 5839.
8. C.K. Narula, S. Daw, J. Hoard, T. Hammer, "Materials Issues Related to Catalysts for Treatment of Diesel Exhaust," *Int. J. Amer. Ceram. Tech*., 2 (2005) 452 (invited).

Presentations (last 12 months)

1. Narula, C.K.; Chen. X.; Stocks, M.G.; "First-Principles Studies of the Structure and Bonding of Metal Atoms Supported on θ-Alumina," 229th American Chemical Society Meeting, San Francisco, CA, March 21-25, 2009.
2. Moses-DeBusk, M.; Narula, C.K. "Catalyst by design: Combining the power of theory, experiments, and nanostructural characterization for catalyst development," 227th National American Chemical Society Meeting, March 2009 (invited).
3. Narula, C.K.; DeBusk, M.M.; Allard, L.F.; "Catalyst by Design – Theoretical, Nanostructural, and Experimental Studies of Oxidation Catalyst for Diesel Engine Emission Treatment, DEER 2009, Detroit, MI.

Agreement 19214: Effects of Biodiesel Fuel on Diesel Particulate Filter Materials

M. J. Lance and T. J. Toops
Oak Ridge National Laboratory

Objective/Scope

To characterize changes in the microstructure and material properties of diesel particulate filters (DPFs) in exhaust gas produced by biodiesel blends.

Technical Highlights

A series of engine experiments were implemented to collect solid and semi-volatile particle emissions as a function of fuel type, ULSD or B20, and exhaust temperature, 300°C and 500°C. The exhaust was sampled using three techniques that will allow analysis of the following parameters:

- Acidic nature of the condensable species in the exhaust (condensate collection).
- Ratio of organic fraction versus elemental carbon fraction (quartz filters).
- Identification of the species in the organic fraction (Teflon filters).

Additionally, soot was collected using DPF cores to give a representation of the organic and elemental carbon fraction that would be expected in a typical DPF device. Several of the above analysis techniques will be employed on these samples, with a focus on the total acid content of the organic fraction and the specific acidic species that exist.

Results to date show a higher acid content in the B20 based exhaust. A more detailed report will follow in the next quarterly report.

Status of FY2010 Milestones

Measure the chemical composition and pH of condensate and PM generated by a diesel engine running with ULSD and biofuel blends. **(09/10)** *On Schedule.*

Communications/Visits/Travel

None

Problems Encountered

None

Publications/Presentations/Awards

None

References

None

Agreement 20091: Electrically-Heated Diesel Particulate Filter Regeneration

M. J. Lance, J. E. Parks II, A. A. Wereszczak and W. P. Partridge Jr.
Oak Ridge National Laboratory

Objective/Scope

Study efficiency benefits and materials issues associated with the electrically-heated diesel particulate filter (EHDPF) device developed by General Motors (GM). Specific objectives are:

Task 1: FEERC-NTRC

- Characterize potential fuel savings of the approach and related benefits to other emission control devices.
- Measure gas and substrate temperatures to obtain accurate picture of conditions experienced during regeneration.

Task 2: CerSaT-HTML-MST

- Resolve current disconnect between cordierite substrate model predictions and
- actual substrate durability.
- Use data and results to develop general design rules on heater geometries to
- optimize substrate durability.

Task 3: CS-MST

- Conduct a high-level discussion on the durability of the heater alloy.

Technical Highlights

This CRADA was signed on March 22nd, so no work was conducted by the end of the 2nd quarter. A face-to-face kick-off meeting was scheduled for May 18th at ORNL.

Status of FY2010 Milestones

Communications/Visits/Travel

Problems Encountered

Publications/Presentations/Awards

None

References

None

Agreement 9105: Ultra-High Resolution Electron Microscopy for Characterization of Catalyst Microstructures and Reaction Behavior

L. F. Allard, C. K. Narula, S. A. Bradley
Oak Ridge National Laboratory

Objective/Scope

The objective of the research is to understand fundamental processes in catalytic systems with applications to transportation technologies, such as those used for the treatment of NO_X emissions, and for the production of biomass-derived liquid fuels. The research heavily utilizes new capabilities and techniques for ultra-high resolution transmission electron microscopy with the HTML's aberration-corrected electron microscope (ACEM). The research is ultimately focused on understanding the effects of reaction conditions on the changes in morphology of heavy metal species on "real" catalyst support materials (e.g. oxides and carbon materials), and the understanding of the structures of model mono-, bi- and multi-metallic catalyst systems of known particle composition. A major thrust of these studies has been to develop methods of in-situ microscopy at elevated temperatures and under controlled gas compositions. This work has expanded with the collaboration with Protochips Inc. (Raleigh, NC), who provide a novel heating technology utilizing MEMS-based heating devices that we have shown to be stable enough to provide sub-Ångström imaging capabilities at high temperature in the ACEM. Model samples of nanoparticulates of controlled composition on carbon or oxide supports are also being studied in collaboration with the catalysis group at the University of Texas-Austin (Prof. P. Ferreira), the University of Texas-San Antonio (Prof. M. Jose-Yacaman), the University of Missouri-St. Louis (Prof. J. Liu), and University of New Mexico (Prof. A. Datye). Studies of the behavior of Pt species on oxide substrates are also being conducted with Drs. S. A. Bradley of UOP Co., and C. H. F. Peden of PNNL. NOx trap catalyst materials BaO/Al_2O_3 are being studied with Dr. Peden and Dr. Ja Hun Kwak at PNNL and Pt-Re/C catalysts on model carbon nanotube materials are being studies with Drs. Y. Wang and L. Zhang, also of PNNL. We have also initiated a new study of "intelligent catalysts" for automotive emission control applications, based on the self-regenerative phenomenon of heavy metal species such as Pd and Rh in Ca- and La-based perovskite crystal structures.

Technical Progress

This report highlights work this quarter on (1) tests of the Gen 2 environmental cell (E-cell) at both elevated temperatures and pressures; (2) the development of a new heating holder for the ACEM that also allows for double-tilting operation; (3) initial work on correlating the effects on the microstructure of atomically dispersed oxidized Pt on alumina that was subsequently reduced in the electron microscope, with temperature programmed reduction (TPR) behavior of the same material. Also, an initial report of our collaboration on a study of "single-Pt atom catalysis is given.

Gen 2 E-cell Tests at Increased Pressures

The Gen-2 environmental cell has been further tested to determine the efficacy of operation both at elevated temperatures and at pressures above the previously reported

(Q1, FY2010) 2Torr; in particular, to see if we could image crystal lattices at higher pressures. In the tests shown here, we deposited a sample of Au/Fe2O3 catalyst powder onto the E-cell heater membrane; surface Au nanoparticles had been removed from the support material by leaching in an aqueous solution of 2% NaCN [1]. The resulting catalyst showed residual Au species that were conclusively determined to be retained internal to the Fe_2O_3 support material. Figure 1 shows a typical high-angle annular dark-field (HA-ADF) image of the catalyst before and after leaching, recorded in the usual fashion with the sample mounted on a thin carbon support film. Figure 2 reviews schematically the geometry of the E-cell, and illustrates how the catalyst powder is supported on the heater. The imaging of the Au crystal lattice, therefore, involves the beam passing first through a nominal 20nm carbon film that acts as the upper window to isolate the cell gas from the microscope vacuum, then through the Fe_2O_3 support particle until reaching the Au nanoparticle in the interior, then through the remainder of the Fe_2O_3 support, and finally through the gas in the cell and the lower window, an amorphous 25nm silicon nitride material. The gas path in the cell is nominally a 50 -micron distance, controlled in the present incarnation of the holder by the diameter of the heater leads that make contact to the Protochips Aduro™ heater chip. For comparison, in an "environmental TEM" that is dedicated to in-situ studies, differential pumping apertures are used above and below the sample to retain gas around the sample. The apertures define a gas path on the order of a centimeter, or 20 times the length of the path in our prototype E-cell.

Figure 3 shows a sequence of images of the same sample area, recorded at 5mX direct magnification, with the cell first at vacuum (3a), and then at 5 Torr and 10 Torr (3b and 3c, respectively). The Au lattice with 2.04Å {200} planes is seen at 10 Torr in both the high-angle annular dark-field (HA-ADF) images (left side), and bright-field images (right side). We ran the cell at 20 Torr also, but the sample area shown in Fig. 3, which had been imaged for a long time, became contaminated, so we imaged an adjacent are to show that even at 20 Torr we retained the ability to image crystal lattices (Fig. 4). We cannot compare these results directly with those which have been obtained to date by laboratories that utilize environmental TEM instruments, as those instruments can operate only up to about 8 Torr maximum pressure, and require 300 kV (vs the 200 kV of the ACEM) operating voltage to penetrate the long gas path required by their objective lens pole piece geometry. So we believe the early results achieved by the new E-cell technology we are developing with Protochips Co. represent an advanced capability for imaging catalyst reaction events at high resolution.

New Double-Tilt Heater Holder Has Been Developed

In collaboration with Protochips Co., and Prof. Emeritus W.C. Bigelow of the University of Michigan, we have designed and fabricated a heating specimen holder that permits a second axis of tilt so that specimen areas can be precisely oriented with the electron beam parallel to know crystallographic directions, thereby allowing better high-resolution imaging, more accurate results and more reliable data interpretations. Figure 5a shows the full specimen rod, which incorporates a motor drive into the handle to run the second tilt axis, and the control box with a double-throw momentary contact switch that allows the ± directions of the second axis. A cable connection between the control box

and the specimen rod allows the box to be placed next to the operator, in the ACEM control room. Fig. 5b is a close-up showing the tilt table of the new rod, with a Protochips Aduro heater chip installed. The second tilt has a limit of ±6°, which is adequate to achieve precision orientations for many of the catalysts and other materials of interest. Examples of the utilization of the new specimen rod will be presented in the next quarterly.

New study of Pt/alumina reduction mechanisms begun with UOP Co.

We have been working with Dr. Stephen Bradley of UOP Co. on a fundamental study of the effects of oxidation and reduction cycles on experimental Pt/alumina catalysts doped at low levels such that the Pt species are dispersed at the mononuclear, dimer, trimer and ultra-fine cluster level. UOP has studied the effects of reduction treatments on prior oxidized Pt/alumina samples, using the technique of temperature-programmed reduction (TPR). We are interested in correlating the TPR behavior with the behavior of Pt species on the support, to obtain first-order information that will lead to better understanding of the reduction reaction. In the TPR technique, the number of reducible species present on the catalyst surface and the temperature at which the reduction of each species occurs is determined. An important aspect of TPR analyses is that the sample need not have any special characteristics other than containing reducible metals (oxidized platinum in our experiment). The TPR analysis begins by flowing an analysis gas (typically hydrogen in an inert carrier gas) through the sample, at ambient temperature. While the gas is flowing, the temperature of the sample is increased linearly with time and the consumption of hydrogen by adsorption/reaction is monitored. Changes in the concentration of the gas mixture downstream from the reaction cell are determined. This information yields the volume of hydrogen uptake. Figure 6 shows the TPR curve for our Pt/alumina as-prepared oxidized catalyst. The hydrogen consumption rate is given in mmol H_2 per gram of catalyst per second, and peaks at 300°C for our material.

We imaged the original oxidized catalyst at room temperature, and then the same or nearby adjacent areas at the different temperatures after ramping at a constant rate of 10°C, with the sample holder retracted into the specimen airlock, under 4%H_2/Ar at atmospheric pressure. The instant heating and cooling behavior of the Protochips heating devices allows us to do the ramp-up to a given temperature, then cool to RT for imaging (after re-inserting the specimen holder into the microscope), and afterward to continue the ramp heating from the previous level up to the next selected imaging temperature. Thus we have images at RT, 250°C, and subsequently every 50°C up to 500°C. Selected images from the sets recorded at the various temperatures are shown also on Fig. 6. These images are processed in order to highlight the atomic species in bright contrast in these HA-ADF images. We note that the Pt distribution as-oxidized consists primarily of mononuclear species, with some dimers and trimers present, and that there is little tendency for clustering of Pt with ramping to 300°C, even though the Pt atoms are very mobile on the surface of the support. No significant clustering is seen even up to 500°C, but inspection of several image areas show a tendency for development of more trimers and higher at both 400° and 500°C (clusters being defined as groups of 10 or more atoms). In future experiments, we will duplicate these tests for

confirmation of the results, and also conduct similar ramping experiments by heating in the vacuum of the electron microscope (a reducing environment), to compare to the atmospheric pressure results.

Other work:

Single-Pt-Atom Catalysis: We have been collaborating on another study of catalysis by Pt species in which initial results have shown that the primary catalysis phenomenon (for CO oxidation, as an example) occurs at single Pt atom sites, and that the reaction is enhanced two- to three-fold with the Pt species dispersed at the single atom level, and finally that the catalyst (Pt/Fe_2O_3) is stable long term with Pt so dispersed. The results of this study, in collaboration with Prof. Jimmy Liu of the University of St. Louis-Missouri, and colleagues at the Chinese Academy of Science, Dailin, China, is being prepared for submission to the journal Nature Chemistry. This work will be highlighted as part of the next quarterly.

"Intelligent Catalyst" Study with UMich/Ford: In collaboration with Prof. Xiaoqing Pan and his graduate student Michael Katz at the University of Michigan, along with colleagues George Graham and Andrew Drewes of Ford Research Laboratory, we have initiated a study of the self-regeneration phenomenon recently reported to occur during oxidation-reduction cycles in certain perovskite structures doped with heavy metal species such as Pt, Pd and Rh. We have obtained images of undoped calcium titanate and Rh-doped calcium titanate, the latter after an oxidation treatment. In the intelligent catalyst systems, oxidation drives the doping species into the crystal lattice, and subsequent reduction allows diffusion of the doping species to the surface, to form stable catalytic particles. Further oxidation causes diffusion back into the lattice. This phenomenon will be studied ultimately using our E-cell technology, in order to elucidate the mechanism of this process. This work will also be highlighted in upcoming quarterlies.

References:

1. **L.F. Allard**, A. Borisevich, W. Deng, R. Si, M. Flytzani-Stephanopoulos and S.H. Overbury, "Evolution of gold structure during thermal treatment of Au/FeOx catalysts revealed by aberration-corrected electron microscopy," *Journal of Electron Microscopy* **58(3)**: 199–212 (2009).

Status of Milestones

On schedule

Communications/Visits/Travel

Publications

1. "New Insights into the Growth Mechanism and Surface Structure of Palladium Nanocrystals;" B. Lim, H. Kobayashi, P.H.C. Camargo, **L.F. Allard** and J. Liu, *Nano Research* **3**(3), March 2010, 180-188.

Several extended abstracts are accepted for publication and presentation at the annual Microscopy Society of America meeting in August 2010, Cambridge University Press:

1. "Ultrahigh Resolution STEM and NMR Studies of Poorly Crystalline γ–Al_2O_3 Surfaces: New Insights From Imaging and Spectroscopy," J.H. Kwak, J.Z. Hu, D. Mei, D.H. Kim, J. Szanyi, **L.F. Allard**, and C.H.F. Peden

2. "Surface Channeling in Aberration-corrected STEM of Nanostructures," Jingyue (Jimmy) Liu and Lawrence F. Allard**

3. "Morphological and Electronic Structure of Pt-Re Nanoparticles Supported on Carbon under Activation and Reaction Conditions for Aqueous-Phase Reforming of Bioliquid," Liang Zhang, David King, Yong Wang and **Lawrence F. Allard**

4. "Aberration-Corrected STEM Image Simulation of Segregation in Pt_3Co Nanoparticles for PEM Fuel Cells, " Brian N. Patrick, **Lawrence F. Allard**, Yang Shao-Horn and Paulo J. Ferreira

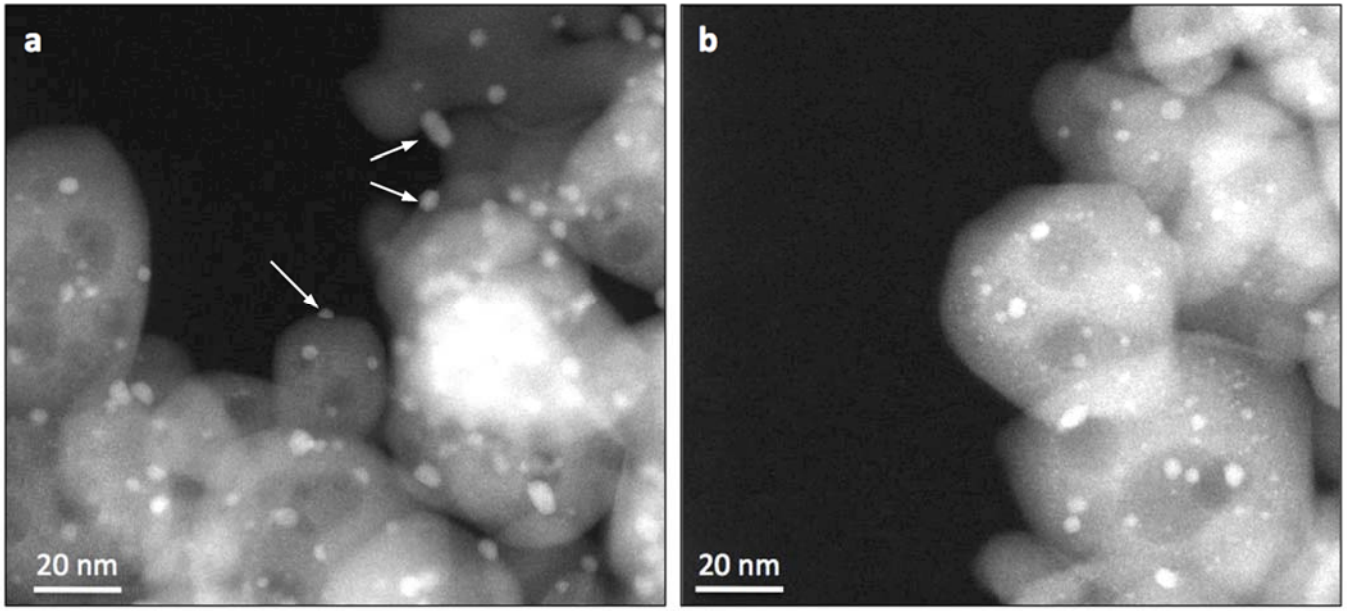

Fig. 1. a) HA-ADF image of Au/Fe2O3 catalyst prior to leaching. External Au nanoparticles seen e.g. arrows; b) Catalyst after leaching in aqueous NaCN solution; no external Au nanoparticles present.

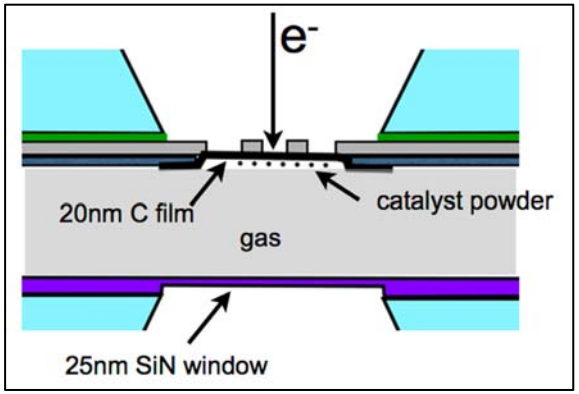

Fig. 2. Schematic of E-cell showing the regions through which the beam passes during a reaction experiment.

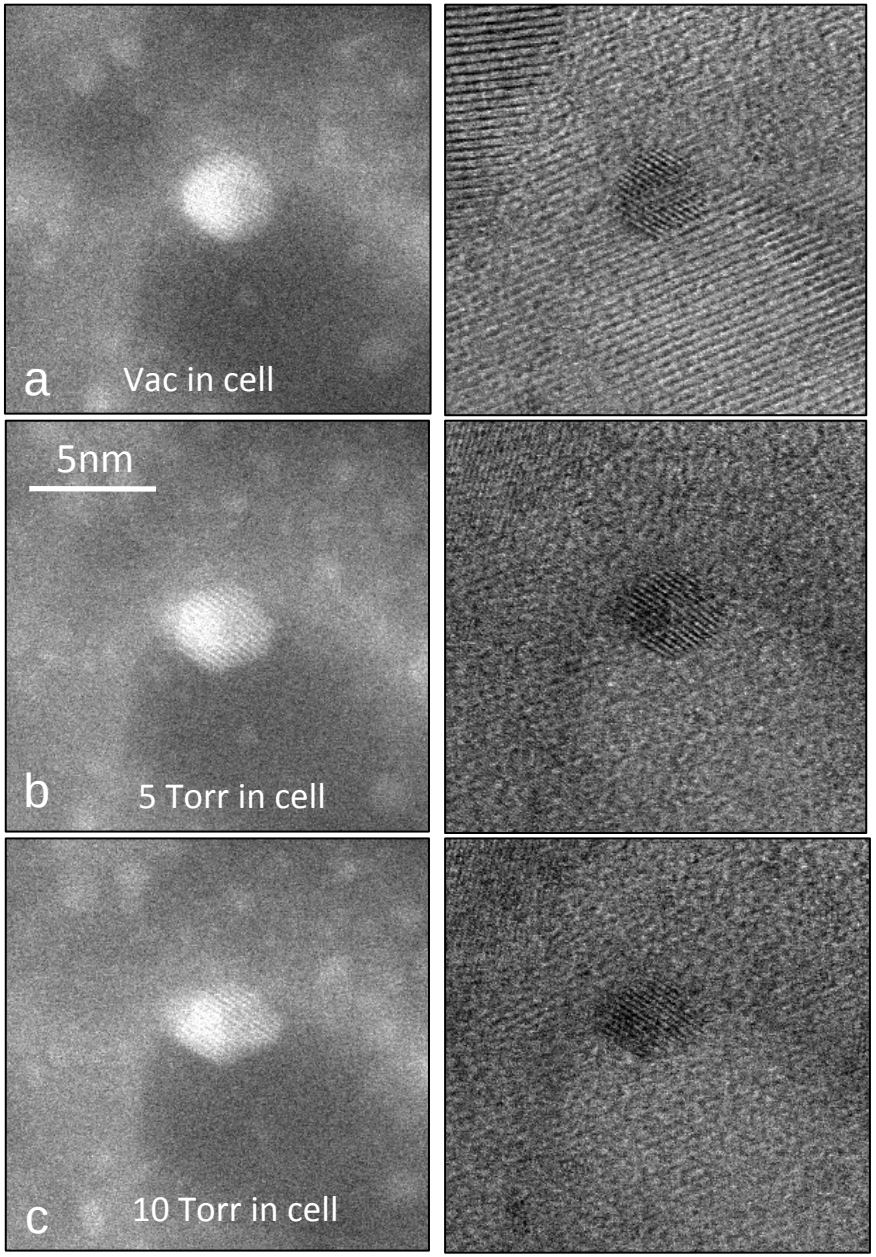

Fig. 3 HA-ADF (left) and BF (right) images taken with a) vacuum in the cell, b) 5 Torr in the cell and c) 10 Torr in the cell. Note that crystal lattice fringes in the Au nanoparticle and the Fe_2O_3 support are still resolved at 10 Torr.

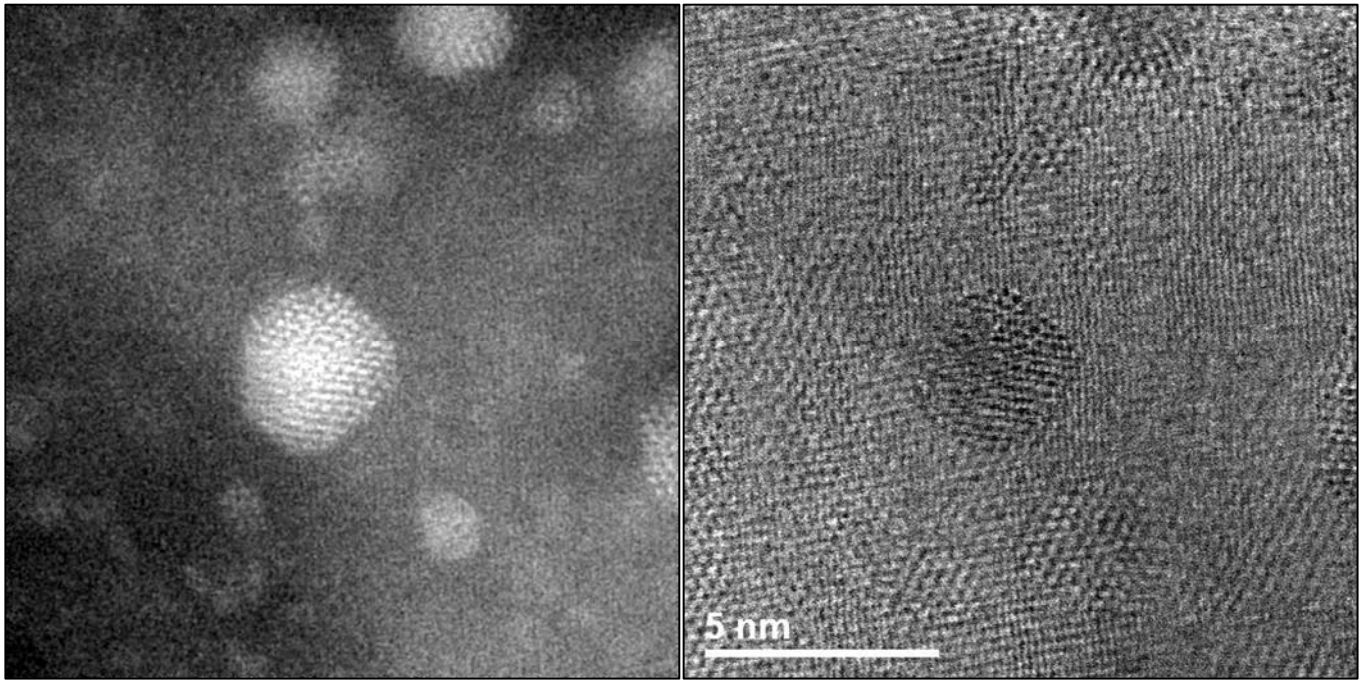

Fig. 4. Example of HA-ADF and BF images of a nearby area of the Au/Fe_2O_3 catalysts, recorded at 10Mx direct magnification with the E-cell at 20 Torr and 500°C, showing clear atomic columns in the Au particles visible inside the Fe_2O_3 support.

Fig. 5. a) overall view of the new double-tilt heating holder, with tilt controller that allows tilt operations to be run from ACEM control room; b) close-up view ot the rod tip, showing a heater chip installed on the tilt table. Total range of tilt permitted is ±6°.

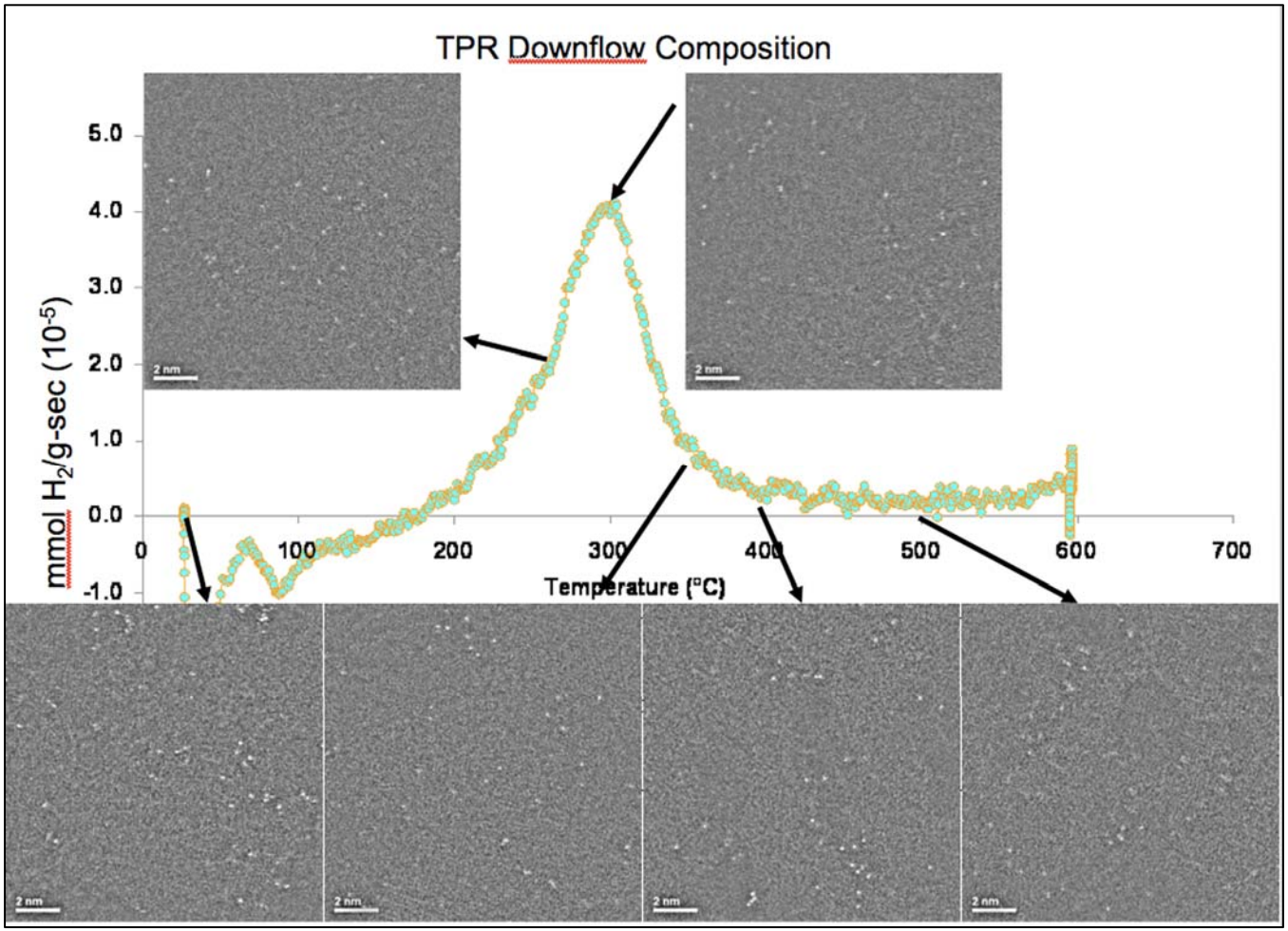

Fig. 6. TPR curve for experimental Pt/alumina catalyst with 0.5 wt% loading, and processed HA-ADF images recorded after ramping to the indicated temperatures, showing behavior of atomically dispersed Pt species. See text for details.

Agreement 14957: High Temperature Thermoelectrics

A. A. Wereszczak, H. Wang, R. McCarty, J. Sharp,****
Oak Ridge National Laboratory
****Marlow Industries, Inc.**
*****General Motors R&D Center**

Objective/Scope

Measures needed thermomechanical and thermophysical properties of candidate thermoelectric (TE) materials and then use their data with established probabilistic reliability and design models to optimally design automotive and heavy vehicle TE modules. Thermoelectric materials under candidacy for use in TE modules tend to be brittle, weak, and have a high coefficient of thermal expansion (CTE); therefore, they can be quite susceptible to mechanical failure when subjected to operational thermal gradients. A successfully designed TE module will be the result of the combination of temperature-dependent thermoelastic property and strength distribution data and the use of the method of probabilistic design developed for structural ceramics.

Technical Highlights

Three efforts continued during the present reporting period. One involved the ongoing CRADA with Marlow Industries. A second involved the ongoing effort to develop a test method that will allow flexure strength measurement of thermoelectric materials while a thermal gradient is superimposed. And the third involve neutron analysis of TE materials.

I. Thermoelastic and Mechanical Properties (CRADA)

Thermomechanical and thermophysical testing of Marlow-supplied materials continued throughout the FY10Q2.

I.a. Skutterudites

Uniaxial bend strength testing of n- and p-type skutterudites was performed as a function of temperature. Several temperatures were tested at and at least 15 bend bars were tested at each to promote statistical significance. Dilatometry on both skutterudite compositions was performed to determine their coefficient of thermal expansion. Seebeck coefficient and electrical conductivity of both compositions was also quantified. Microstructural imaging of polished and fracture surfaces of both compositions were completed using scanning electron microscopy (SEM).

I.b. PbTe

Uniaxial bend strength testing of n-type lead telluride (PbTe) was performed as a function of temperature. Several temperatures were tested at and at least 9 were tested at each to promote statistical significance. Dilatometry was performed to determine their coefficient of thermal expansion. Seebeck coefficient and electrical conductivity was also quantified. Microstructural imaging of polished and fracture surfaces were completed using SEM.

II. Mechanical-Temperature-Gradiented Testing
Design of bend fixturing occurred and its fabrication is underway.

III. Initial Assessment of Stress Measurements Using Neutron Scattering
PbTe and bismuth telluride (Bi_2Te_3) elements were tested at the residual stress mapping facility at ORNL's High Flux Isotope Reactor (HFIR). Scans were performed to assess available diffraction peaks and intensity in both materials. Strong diffraction peaks were observed in PbTe elements indicating the possibility to perform neutron stress mapping of thermoelectric modules. Bi_2Te_3 elements also showed expected diffraction peaks. Due the layered structure, stress measurements in modules could be more challenging, especially for Bridgeman materials.

Status of FY 2010 Milestones

1. Generate thermoelastic and mechanical property database as a function of temperature on candidate p- and n-type TEMats fabricated by Marlow Industries as part of CRADA. (09/10) *On schedule*.
2. Develop in-situ thermal-gradient-strength test method for TEMats. (09/10) *On schedule.*

Communications/Visits/Travel

Two conference calls were held between Marlow and ORNL (Wereszczak and Wang) on 15 January 2010 and 05 March 2010 to discuss progress of the CRADA.

Problems Encountered

None.

Publications/Presentations/Awards

A. A. Wereszczak, M. E. Ragan, K. T. Strong, Jr., P. J. Ritt, H. Wang, J. R. Salvador, and J. Yang, Strength of N- and P-Type Skutterudites," to appear in Vol. 31, *Ceramic Engineering and Science Proceedings*, 2010.

References

None.

Agreement 16308: MBD Thermoelectrics Theory and Structure

David J. Singh
Oak Ridge National Laboratory

Objective/Scope

We will use modern science based materials design strategies to find ways to optimize existing thermoelectric materials and to discover new families of high performance thermoelectrics for waste heat recovery applications. The emphasis will be on the thermoelectric figure of merit at temperatures relevant to waste heat recovery and on other properties important for applications, especially anisotropy, cost, and mechanical properties.

Technical Highlights

Vehicular applications of thermoelectric materials for waste heat recovery will be greatly facilitated by the identification of high performance materials that have low cost and are available in large quantities. One class of materials that shows great promise are filled skutterudites. The first such material was $La(Fe,Co)_4Sb_{12}$. This is a Zintl-type compound. More recently higher performance has been found by replacing La by mixtures of rare earth elements, or rare earth elements plus Ba, particularly in n-type material. These materials derive their performance from the combination of low lattice thermal conductivity due to the rare earth filler and a favorable electronic structure that has multiple heavy conduction bands. [1] We constructed a classical potential model for $LaFe_4Sb_{12}$ based on a fit to first principles calculations. Green-Kubo calculations of the thermal conductivity were performed for this model based on molecular dynamics simulations (Fig. 1). This was done in collaboration with the Naval Research Laboratory.

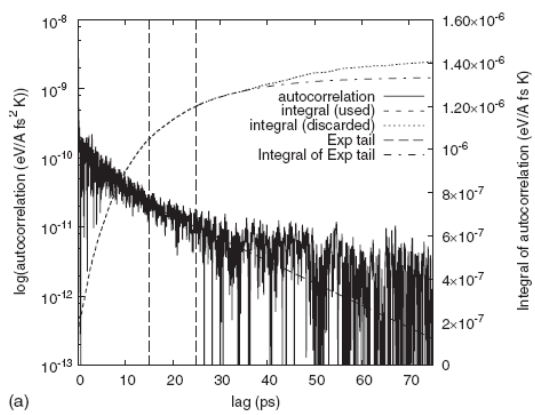

Fig. 1: Calculated autocorrelation for $LaFe_4Sb_{12}$ from molecular dynamics simulations using a first principles based classical model. This yields a thermal conductivity very close to the experimental value and elucidated the origin of the reduction relative to the unfilled compound.

Our calculations showed that the thermal conductivity reduction due to filling comes from an anharmonic mixing of modes associated with the rare-earth and the Sb modes of the host lattice. Importantly, we did not find specific chemical interactions involving

the rare earth f-electrons to be important. This means that simple, non-rare earth ions could also be used. This suggested examining mixed fillers based on alkaline earths instead of rare earths. These would be mixtures of Ca, Sr and Ba. This is of importance for vehicular applications because alkaline earths are cheap and available, while rare earths are more expensive and there are supply questions. Motivated by this, we did calculations of the Einstein mode frequencies for Ca, Sr and Ba filled skutterudite. We find that the frequencies are higher than in skutterudites filled with heavy rare earth ions, and that very similar frequencies of ~90 cm^{-1} occur for the three elements. However, the force constants for different alkaline earths are very different as are the expected mean square displacements. Considering what we found for the mechanism of the thermal conductivity reduction in $LaFe_4Sb_{12}$, this implies that mixed alkaline earth elements are a good opportunity for realizing lower cost but still high performance skutterudite thermoelectrics.

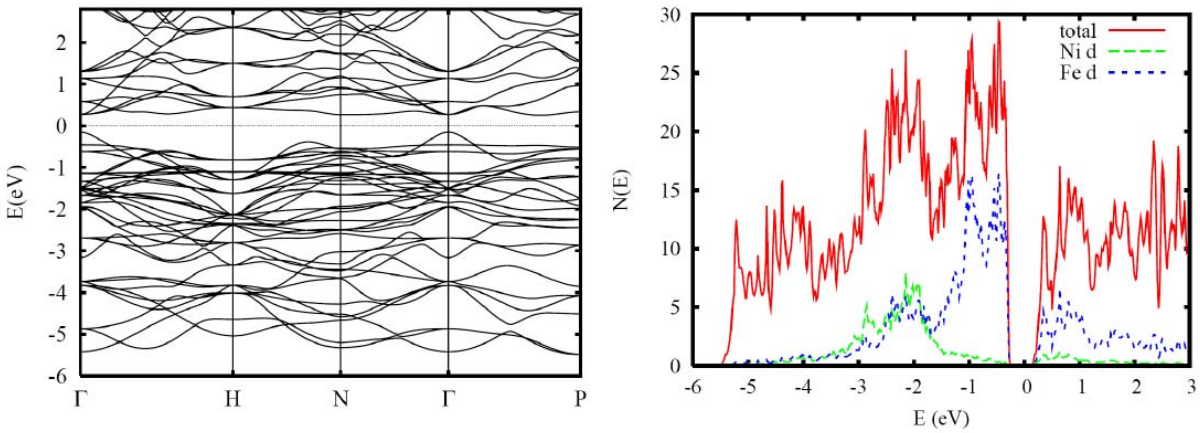

Fig. 2: Calculated band structure (left) and density of states (right) for a supercell of $SrFe_3CoSb_{12}$.

We also did calculations for alkaline earth filled skutterudite using Ni as a source of electrons to control the doping, instead of Co. The band structure and density of states for a supercell are shown in Fig. 2. We find that the filling opens a band gap in this material, similar to the Co based compound, although the details differ. The key points are (1) in the valence bands we find a combination of heavy and light bands at the band edge and (2) that there are multiple very heavy bands at the conduction band edge. This is similar to $LaFe_4Sb_{12}$ and leads to the expectation of good thermoelectric performance, similar to that material. The calculations also suggest that the mobility may be higher in this material than in La filled material, which would suggest that the performance of the p-type compound could be better than p-type $LaFe_4Sb_{12}$ if the doping level of the alkaline earth filled Ni compound is optimized. For n-type doping, we find very heavy bands comparable to the state-of-the-art multiply filled skutterudites based on $CoSb_3$. The results indicate that compounds $A(Fe,Ni)_4Sb_{12}$, where A is a mixture of Ca, Sr and Ba may have performance comparable to the best skutterudites if the doping level is optimized. We are currently performing transport calculations along with detailed phonon modeling to further quantify these results and to determine the doping level dependence of the properties. This will be needed for optimization of the

compounds. These are based on first principles calculations done with the LAPW method [2] and Boltzmann transport. [3]

The importance of this is (1) alkaline earths are cheap and available as compared to rare earths and (2) Ni is substantially cheaper than Co, and furthermore only half as much of this element is needed to achieve the correct electron count as compared to Co (Co has one less valence electron than Ni). This allows the use of material with more Fe, which is a very inexpensive material.

Status of FY 2010 Milestones

We are progressing towards our milestone of predicting new thermoelectric compositions. Strategies that will be used are to continue investigation of Cu containing delafossites, other narrow band oxide materials, skutterudites and chalcogenides. We also plan to continue investigation of nano-structured PbSe and related materials. Depending on the results we will continue with those materials and/or investigate alternate narrow band oxides containing mixed-valent transition element ions and Zintl-phase materials.

Communications/Visits/Travel

D.J. Singh hosted a visit by three scientists from Corning, Inc. They gave a presentation on “Multi-valence state oxide thermoelectrics” and had discussions about possible interactions with ORNL on oxide thermoelectrics.

Problems Encountered

No significant problems encountered this quarter.

Publications/Presentations/Awards

D.J. Singh was elected to the Executive Committee of the American Physical Society, Division of Computational Physics.

D.J. Singh give an invited talk, “New directions in thermoelectric materials” at the International Conference on Advanced Ceramics and Composites”, Daytona Beach, Florida.

D.J. Singh gave an invited talk, “Thermoelectric Materials” at the Institute for High Performance Computing, Singapore.

Refereed Paper: L. Zhang, M.H. Du and D.J. Singh, “Zintl-phase compounds with $SnSb_4$ tetrahedral anions: electronic structure and thermoelectric properties”, Physical Review B **81**, 075117 (2010).

References

1. D.J. Singh, “Theoretical and Computational Approaches for Identifying and Optimizing Novel Thermoelectric Materials”, in “Semiconductors and Semimetals, Vol. 70: Thermoelectric Materials Research”, p. 125 (Academic Press, New York, 2000).
2. D.J. Singh and L. Nordstrom, Planewaves, “Pseudopotentials and the LAPW Method, 2nd Edition”, Spinger, Berlin, 2006.

Agreement 17895: Durability of ACERT Engine Components

Hua-Tay Lin, T. Kirkland, and B. Armstrong
Oak Ridge National Laboratory

N. Philips and J. Jenson
Caterpillar, Inc.

Objective/Scope

There are four primary goals of this research agreement, which contribute toward successful design and implementation of advanced lightweight material components to achieve high-efficiency engine of 55% of heavy-duty diesel engines by 2018 as set under the 21st CT program: 1) the generation of a mechanical engineering database of candidate advanced lightweight materials before and after exposure to simulated engine environments; 2) the microstructural evolution and accompanied chemical changes during service in these advanced materials; 3) material selection, development, and design of complex-shaped components, and 4) application and verification of probabilistic life prediction methodology for advanced high-efficiency diesel engine components. The methodology implemented would also help to manufacture consistent mechanical reliability and performance of complex shaped components.

Technical Highlights

Study of Al-oxide based environmental barrier coating (EBC) developed for the ductile ferritic Fe-steel substrate was continued in this quarterly reporting period. The goal of this EBC developmental study is to provide an alternative approach for an effective protection for the current production ferritic Fe-steel used for exhaust components in heavy-duty diesel (HDD) engine. The application of EBC would allow HDD OEMs to significantly reduce the heat rejection (and thus thermal stress generated) and also prevent the oxidation/corrosion-induced degradation process encountered in the current production materials. Consequently, it would allow the OEMs to avoid the use of the very high-cost stainless steel materials for the exhaust port and manifold components that could potentially lead up to USD $5M cost saving per year. More importantly this is one of the key enabling materials technologies that would allow end users to achieve 55% HDD engine efficiency and life greater than 1 million miles by 2018 as set under the 21st Century Truck Program.

Colloidal processing offers a low cost alternative processing technology for producing uniform coatings on complex-shaped components via a simple dip coating process (i.e., the ORNL slurry coating process) (1-2). Also, the oxide-based coating could be processed at lower temperature with much shorter times, thus preventing the interaction (chemical reaction) between the coating and Fe-based substrate. Control of the rheological behavior of the suspension by tailoring interparticle (or surface) forces is paramount to achieve a high quality and defect free coating. In aqueous-based suspensions long-range attractive van der Waals forces must be balanced by repulsive forces to tailor the desired degree of suspension stability. Typically, ionizable polymeric dispersants, or polyelectrolytes, are used to modify the surface of particles to impart repulsive electrosteric forces (3-4). Aluminum, (H10, Valimet Inc., Stockton, CA) was used as the metal powder in this study. The aluminum powder had an average particle

size of ~ 13.19 μm and surface area of 0.4475 m2/g, determined using dynamic light scattering (Horiba, Inc., Kyoto, Japan) and B.E.T. (Autosorb-1, Quantachrome Instruments, Boynton Beach, FL), respectively. Polyacrylic acid (PAA, 450kg/mol, Aldrich Chemicals, Milwaukee, WI), an anionic polyelectrolyte, was used as the dispersant and PL001 (Polymer Innovations, Inc., Vista, CA) as the rheological modifier for the Al system. Water purity was measured using inductively coupled plasma mass spectroscopy (ICPMS, X Series 2, Thermo Fisher Scientific, Inc., Waltham, MA). The standards (QCS26, High Purity Standards, Charleston, SC) and the nitric acid matrix (Ultrex Pure, J.T. Baker, Phillipsburg, NJ) were used to calibrate the ICPMS. The Al-oxide based coating was employed via a dip or slurry based process. A post heat treatment at 750°C for 2 hrs in argon was carried out to covert the slurry coating into the oxide based coating.

Figure 1 shows the polished cross section of as-coated Al-oxide based layer on the ferritic Fe steel alloy substrate. The detailed SEM observations show that a dense and coherent Al-oxide layer (~ 20 μm thick) containing also Fe and Si elements, which are presumably from the steel substrate enriched with Si, formed after the heat treatment conversion process (Fig. 1). This Al-Fe-O layer could be $FeO\text{-}Al_2O_3$ (or the soli solution of other complex phases) that would need to be verified by further X-ray analysis. A dense oxidation reaction layer ~ 10 μm underneath the Al-oxide layer was also observed. A detailed EDAX mapping for element of Al, Fe, Si, and O was provided in Fig. 2. The element mapping results provide a guideline of the diffusion (and reaction) rate of Al and Fe under the heat-treating condition employed. Consequently, studies of the heat treatment conditions (i.e., temperature and time) will be planed to determine an optimized window for an effective and durable protective coating layer. In addition, study of thermal cycle under a simulated engine condition is in progress in order to determine the long-term stability of the Al-oxide based coating via the low-cost aqueous processing method. The results and details of analysis will be reported in the next quarterly report.

An advanced Tier 4 version of the C15 engine will be delivered to NTRC, ORNL this summer by Caterpillar Inc. This Tier 4 C15 engine will be equipped with EGR and emission control system that would enable effective improvements in engine thermal efficiency via implementations of various advanced material technologies and components. Research and mechanical testing plans on the potential candidate materials and components will be discussed in details. On the other hand, a mixed flow turbine will be installed in the current version of C15 ACERT engine to study its effectiveness on the fuel efficiency improvement.

Status of FY 2010 Milestones

Complete testing and analysis of a prototype ACERT exhaust component with advanced thermal barrier coating. **(09/10**) – On schedule.

Communications/Visits/Travel.

Communications and conference calls with Dr. Nate Philip of Caterpillar and Dr. JG Sun of ANL regarding the up-to-date progress on development of alternative EBC systems for ACERS engine and components.

Communications with Dr. Mike Kass at ORNL NTRC regarding the up-to-date status on verification test run of C15 ACERT engine.

Communications with Dr. Nate Philip of Caterpillar and Mike Kass of ORNL NTRC on the study and installation plan for the mixed flow turbo component.

Problems Encountered

None.

Publications/Presentations/Awards

1. H. T. Lin, "Implementation Methodology of Silicon Nitride Ceramics for heavy-Duty Diesel Engine Application," Invited department seminar, presented at Mechanical and Materials Engineering Department, Florida International University, Miami, FL, March 26, 2010.

2. P. F. Becher, N. Shibata, G. S. Painter, F. Averill, K. Van Benthem, H. T. Lin, and S. B. Waters, "Observations on the Influence of Secondary Me Oxide Additives (Me = Si, Al, Mg) on the Microstructural Evolution and Mechanical Behavior of Silicon Nitride Ceramics Containing RE_2O_3 (RE = La, Gd, Lu)," *J. Am. Cera. Soc*., 93[2] 570-580 (2010).

References

1. Armstrong, B., Kirby, G., Cooley, K., *Proceedings of The 29th International Technical Conference on Coal Utilization & Fuel Systems*, Clearwater, FL (2004).
2. Kirby, G., Cooley, K., and Armstrong, B., *Proceedings of GT2005 ASME Turbo Expo 2005: Power for Land, Sea, and Air*, Reno-Tahoe, NV (2005).
3. Cesarano, J. and Aksay, I., *J. Am. Ceram. Soc.*, 71 (4) 250-55 (1988).
4. Cesarano, J. and Aksay, I., *J. Am. Ceram. Soc.*, 71 (12) 1062-67 (1988).

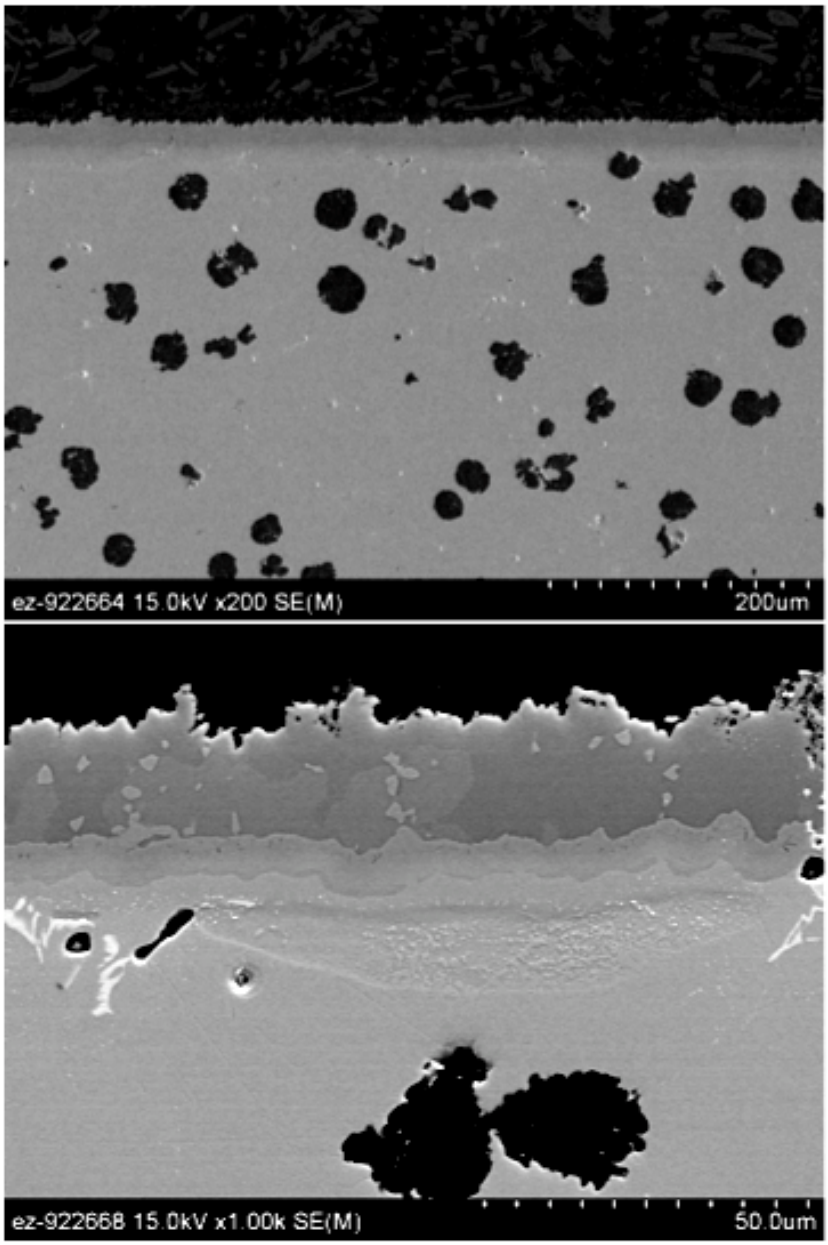

Figure 1. SEM micrographs showed the as-deposited Al-oxide based coating via the low-cost aqueous processing method.

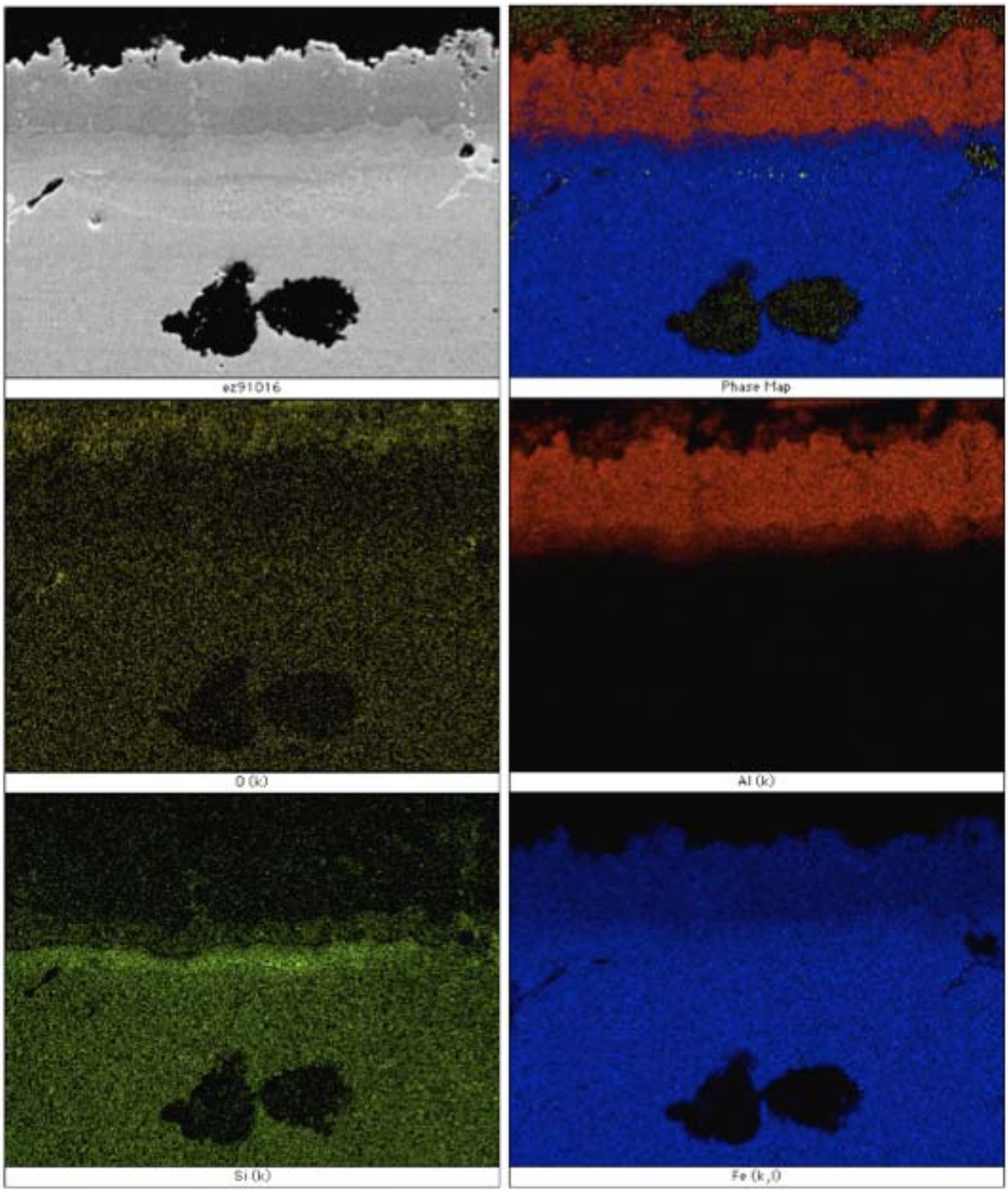

Figure 2. EDAX maps show the details of elements and distribution in the reaction and reaction surface layer on the ferritic Fe-steel substrate.

Agreement 20370: Life Cycle Modeling of Propulsion Materials

Sujit Das
Oak Ridge National Laboratory

Objective/Scope

Perform a life cycle assessment of alternative lightweight light-duty engine designs for vehicle weight reduction and improved fuel economy. In addition, a life cycle energy analysis of CF8C+ cast austenitic stainless steel will be undertaken.

Technical Highlights

A literature search was completed to determine the most representative alternative lightweight engine designs to be considered for the life cycle analysis. Two alternative lightweight designs will be considered and they are to be compared with the baseline Ford Duratec 3.0L, V6, 4-V, DOHC, d-VVY, NA, PFI engine with a power rating of 225 hp used in the recent light-duty technology cost analysis EPA study by FEV, Inc. A downsized 2.0L, I4, 4-V, DOHC, d-VVT, Turbo, GDI having the same power will be considered as one of the lightweight engine design options, whereas the other option includes the use of lightweight engine material. Magnesium will be considered as the lightweight engine replacement material for major engine components such as cylinder block, cylinder head, cylinder liner, structural oil pan, and front engine cover etc. compared to aluminum used for those parts in the baseline engine. The lightweight engine material data is based on the USAMP Magnesium Powertrain Cast Components project and the use of magnesium alloy based engine in some current BMW vehicle models. Life cycle engine data collection has been initiated and fuel economy estimates for various lightweight engine options will be based on a combination of previously published research, available data suitability of various engine types to appropriate vehicle classes, and expert opinions. The commercial LCA software SimaPro will be used for the life cycle analysis.

Future Plans

Complete the life cycle assessment of alternative lightweight light-duty engine designs. A draft report will be prepared summarizing the results of the life cycle analysis. The other task on the life cycle energy analysis of CF8C+ cast austenitic stainless steel in automotive applications will be initiated.

Status of FY 2010 Milestones

On schedule.

Communications/Visits/Travel

Several communication exchanges were made with Greg Kolwich of FEV, Inc. and Alan McEwan of Mahle Powertrain, LLC currently involved in light-duty engine downsizing.

Problems Encountered

None

Publications/Presentations
None

References
None